Development of a Quartz Crystal Microbalance sensor for the detection of Technetium in groundwater

by

Athanasios Papageorgiou, B.Sc., M.Sc.

Being a thesis submitted to Lancaster University in partial fulfilment for the requirements for the degree of

DOCTOR OF PHILOSOPHY

March 2022

DECLARATION

I, Athanasios Papageorgiou, hereby certify that this thesis, unless stated otherwise, is the work of the author, it has been written by me and has not been submitted in support of any previous application for a higher degree. The work presented in this thesis was conducted at the Departments of Engineering and Chemistry at Lancaster University between October 2017 March 2022.

Date: 28 March 2022 Signature of candidate: Athanasios Papageorgiou

Athanasios Papageorgiou

ABSTRACT

Technetium-99, a pure β-emitter with E_{max} =294 keV, is relatively long-lived radio isotope ($t_{1/2}$ =2.1×10^5 y) found in nuclear waste, produced by the fission of U with a yield of 6%. Under normal environmental conditions, it is mostly encountered as the pertechnetate ion, TcO_4^-, which is highly soluble in water and consequently mobile in natural environment. For this reason, and because it often is the first radioisotope that can be detected in contamination scenarios, its monitoring into groundwater is a statutory requirement for every nuclear license site. Current determination methods of ^{99}Tc involve several steps, such as chemical separation from the matrix, purification and source preparation, prior to radiometric (e.g. liquid scintillation counting) or mass spectroscopic (e.g. inductively coupled plasma mass spectroscopy) determination, due to its relatively low concentration in environmental samples, even in contamination scenarios. The detection of ^{99}Tc may take up to several days, thus making these techniques inappropriate for an emergency situation, where real-time monitoring is ideally required. Hence, in this work the development of a sensor for the real time monitoring of ^{99}Tc in groundwater based on the Quartz Crystal Microbalance (QCM) is presented. The QCM is a piezoelectric resonator, which oscillates in a resonant frequency f_s when an electric potential is applied across its body. It is capable of measuring very small changes in mass at its surface, through the change of the resonant frequency. The QCM is modified to respond exclusively to the presence of TcO_4^-, by application of materials reported in the literature for the effective take-up of Tc, such as TREN ligand, TEVA resin and a Ag-4,4bipyridine metal-organic framework. These materials are chemically modified in order to create effective coatings on the surface of the QCM, thus developing novel ligands and films. The structures of these novel materials are characterised by several techniques such as and NMR, IR, MS, XRD and SEM and their response and selectivity is evaluated by monitoring the changes in the resonant frequency of the QCM as a function of the concentration of ReO_4^-, which is a non-radioactive chemical surrogate for TcO_4^-. Finally, the adsorption of ReO_4^- and other interferences is modelled with adsorption isotherms such as Langmuir, Freundlich and Sips. Adsorption

experiments were conducted with $NaReO_4$, NaCl, Na_2SO_4 and Na_2CO_3 and it was found that self-assembled monolayers of the TREN ligand and the active component of TEVA resin, Aliquat-336, did not yield any adsorption results, possibly because ReO_4^- is too light to be detected by a single monolayer. On the other hand, a multi-layered thin film of the Ag-4,4bipyridine metal-organic framework yielded adequate adsorption results; however, through the analysis with adsorption isotherms, it was found that Na^+ cations where adsorbed in the thin film, rather than ReO_4^- anions, possibly through cation-π interactions.

ACKNOWLEDGMENTS

I would like to thank my Director of Studies Dr Fabrice Andrieux for his help, support and enthusiasm as well as his concern for my well-being during my PhD tenure. Special thanks must also go to my co-supervisor Dr Nicholas Evans for his help, support and interest in the work.

I wish to thank the Engineering and Physical Sciences Research Council, the Next Generation Nuclear (GREEN) – Centre for Doctoral Training and Sellafield Ltd for funding this project.

Thanks must go to staff of Lancaster University, Dr Richard Wilbraham, Dr Dominic Laventine, Dr Nathan Halcovitch and to the technicians within the Engineering department for their support.

I am very grateful to my amazing partner, Penny, for her unconditional love and support though all the ups and downs over the course of this PhD, as well as to my family and friends.

Publications resulting from this work include a Journal Article:
"Adsorptive behaviour of a novel Ag-4,4-bipyridine metal organic framework thin film tethered to a quartz crystal microbalance" Papageorgiou, A., Andrieux, F. 2/11/2021 Journal of The Electrochemical Society.

Table of Contents

CHAPTER 1

1 Introduction

Radioactive contamination of the environment is of critical concern to civil nuclear sites around the world. Monitoring programs are implemented in order to characterize and understand the contamination, especially that of groundwater, which is a major pathway to the spread of contamination. Existing monitoring programs involve time consuming methods which are disadvantageous in a field that requires fast responses. There is therefore a need for simple and low-cost detection methods that can be deployed in situ and aid rapid response in the event of contamination being found.

This work focuses on the detection of the radionuclide ^{99}Tc, which forms extremely water mobile pertechnetate (TcO_4^-) anion. The occurrence, physicochemical properties and mobility of ^{99}Tc, as well as the current methods for its separation and measurement are reviewed. Novel ligands and materials, based on existing literature, will be assessed as a new means for the immobilization of ^{99}Tc by a Quartz Crystal Microbalance, which can lead to the development of a real time detector.

1.1 Contamination in civil nuclear sites

In recent years, it has become widely known that there is a large number of sites around the world which have become radioactively contaminated as a result accidents, leaks, spills, deliberate disposals and weapons testing. In this section, the Thermal Oxide Reprocessing Plant (THORP) at Sellafield Ltd (Cumbria), which is one of the biggest nuclear reprocessing plants in the UK, will be used as a real-life example to highlight the significance of the contamination in such sites and the importance of monitoring the levels of several different radionuclides.

Until it was shut down in 2018, the THORP at Sellafield Ltd operated a slightly modified Plutonium Uranium Redox Extraction (PUREX) process for the treatment of spent nuclear fuel. For decades, the resultant radionuclides was being discharged into the Irish Sea, leading to total annual releases of up to 190 TBq by 1997 (see *Figure 1-1*) [1],

[2]. The discharges stopped in 2004 and since then there are serious efforts to remediate ^{99}Tc from any liquid waste and store it in a safe solid state. Also, monitoring of the groundwater of the site has become a mandatory requirement, in order to prevent any accidental releases [3].

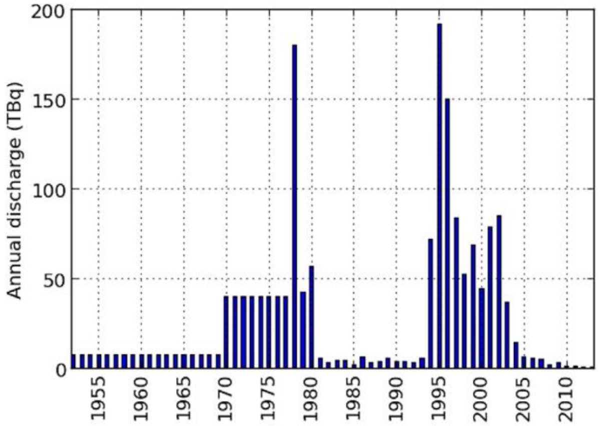

Figure 1-1. Annual discharges of ^{99}Tc from Sellafield in the Irish sea [2]. *In 1980 the site seized its operations, as the construction of the THORP started, which was finished set to operate in 1997, when the discharge started again.*

Contamination of the groundwater due to leaks consists a major issue and for this reason an annual monitoring of groundwater takes place. Table 1.1 shows the maximum measured activities of the main radioisotopes detected in the groundwater of the Sellafield site between 2012 and 2016 [4], as part of the routine monitoring programme, together with the drinking water guidelines recommended by the World Health Organisation's, to provide context.

From the data of Table 1.1, the isotopes of major concern are mainly tritium and ^{90}Sr as they exceed by far the drinking water guidelines set by the World Health Organization (WHO) [5]. Technetium monitoring is a statutory requirement on nuclear license sites but also offers additional advantages as an analyte of interest. The high environmental mobility and very long half-life of technetium coupled with the fact that it does not occur in nature, mean that an effective technetium sensor could lead to an early leak detection system and enable rapid decision making.

Analytical determination of ^{99}Tc is more complex than that of tritium, for example, and routine monitoring for this isotope did not begin until 2000 [6]. Figure 1-2 shows a map of the Sellafield sites and highlights the direction of travel for technetium-99 and other isotopes from their source. Monitoring of the groundwater requires sampling boreholes and monitoring wells located across the site. These samples are then transferred to laboratories for analysis. Most commonly, samples at Sellafield are collected by low flow sampling, which requires flushing large amounts of stagnant water out of the borehole for the sample to be assumed representative, as described in Sellafield's official manual [7]. Then the samples are transferred in the lab for analysis and are assayed by several methods, e.g. direct evaporation for alpha activity, Cerenkov counting [8] for beta activity and gamma spectroscopy for gamma activity, as detailed in Cavendish Nuclear's official manual [9].

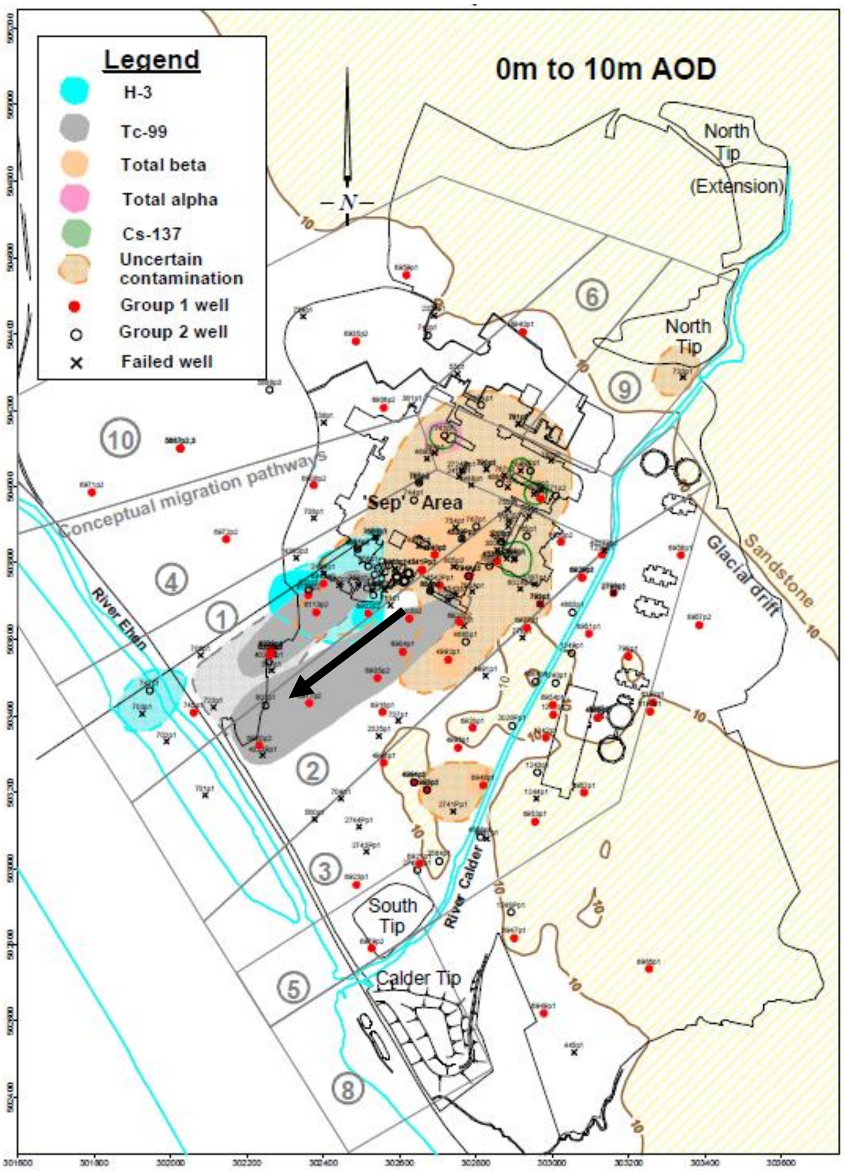

Figure 1-2. Radioactive Contamination and Monitor Wells Screened in the 0m to 10m AOD groundwater layer in Sellafield [6] *The red points correspond to boreholes, through which sampling is conducted. The thick black arrow and the grey areas represent the flow of* ^{99}*Tc in the groundwater.*

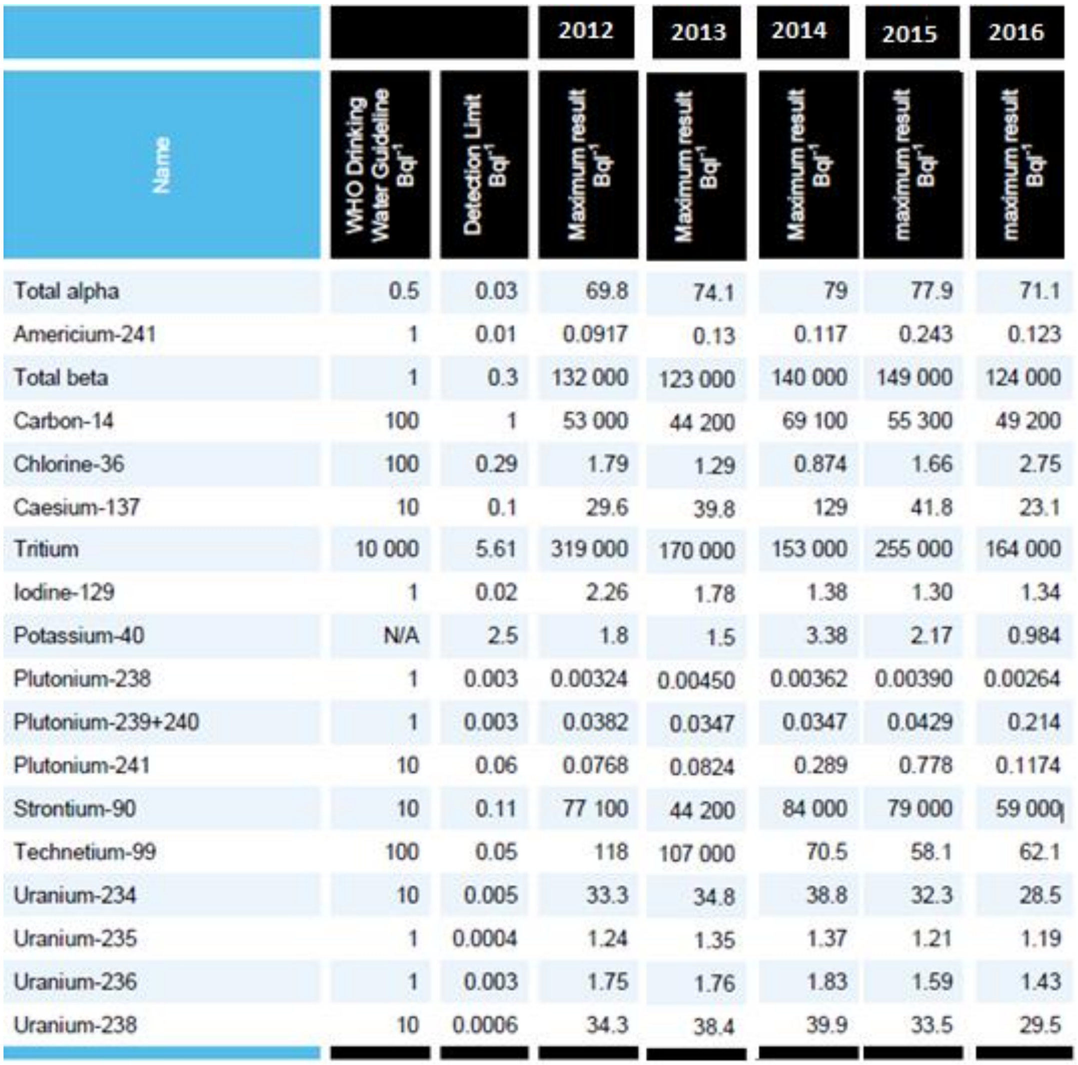

			2012	2013	2014	2015	2016
Name	WHO Drinking Water Guideline Bql^{-1}	Detection Limit Bql^{-1}	Maximum result Bql^{-1}	Maximum result Bql^{-1}	Maximum result Bql^{-1}	maximum result Bql^{-1}	maximum result Bql^{-1}
Total alpha	0.5	0.03	69.8	74.1	79	77.9	71.1
Americium-241	1	0.01	0.0917	0.13	0.117	0.243	0.123
Total beta	1	0.3	132 000	123 000	140 000	149 000	124 000
Carbon-14	100	1	53 000	44 200	69 100	55 300	49 200
Chlorine-36	100	0.29	1.79	1.29	0.874	1.66	2.75
Caesium-137	10	0.1	29.6	39.8	129	41.8	23.1
Tritium	10 000	5.61	319 000	170 000	153 000	255 000	164 000
Iodine-129	1	0.02	2.26	1.78	1.38	1.30	1.34
Potassium-40	N/A	2.5	1.8	1.5	3.38	2.17	0.984
Plutonium-238	1	0.003	0.00324	0.00450	0.00362	0.00390	0.00264
Plutonium-239+240	1	0.003	0.0382	0.0347	0.0347	0.0429	0.214
Plutonium-241	10	0.06	0.0768	0.0824	0.289	0.778	0.1174
Strontium-90	10	0.11	77 100	44 200	84 000	79 000	59 000
Technetium-99	100	0.05	118	107 000	70.5	58.1	62.1
Uranium-234	10	0.005	33.3	34.8	38.8	32.3	28.5
Uranium-235	1	0.0004	1.24	1.35	1.37	1.21	1.19
Uranium-236	1	0.003	1.75	1.76	1.83	1.59	1.43
Uranium-238	10	0.0006	34.3	38.4	39.9	33.5	29.5

Table 1.1. Maximum measured activities in Sellafield for the years 2021-2016. Adapted from [4].

Thus, being able to detect Tc in real time in the groundwater would offer Sellafield Ltd and other similar nuclear sites the opportunity to reduce contamination in early stages. The following section discusses the nature and properties of Technetium and highlights some of the techniques used to detect it in ground water, which are time consuming and costly.

1.2 Physicochemical properties of Technetium-99

Technetium (Z=43) is the lightest element with no stable isotopes. This was predicted by the German physicist Mattauch who formulated the “prohibition rule” stating that the isobars of two adjacent elements in the Periodic Table cannot be stable [10]. It was synthesised a few years later by Perrier and Segre by irradiating a molybdenum target with deuterons[11].

Technetium may occur naturally from the spontaneous fission of ^{238}U, neutron-induced fission of ^{235}U or cosmic ray reactions with Mo, Ru and Nb within the earth’s crust [12], and several millenia ago, the Oklo natural nuclear reactors in Gabon were a natural source of Tc [13]. However, the natural production of Tc is insignificant compared to its anthropogenic sources which include nuclear power plants, nuclear weapons and medical applications [12].

Fourty-five isotopes of Tc have been synthesised, ranging from ^{85}Tc to ^{117}Tc, the most long lived of which are ^{97}Tc ($t_{1/2} = 2.6 \times 10^6$ y), ^{98}Tc ($t_{1/2} = 4.2 \times 10^6$ y) and ^{99}Tc ($t_{1/2} = 2.1 \times 10^5$ y). Technetium-99, which is a weak β-emitter (E_{max} = 294 keV), can be produced by thermal neutron induced fission of ^{235}U with a relatively high yield of 6%, leading to the production of about 1 kg of ^{99}Tc from 1 ton of uranium (with uranium enriched at 3%) and thus making it quite abundant among fission products [14]. Meanwhile, ^{99}Tc can also be produced by the β-decay of ^{99}Mo, as shown in Figure 1-3.

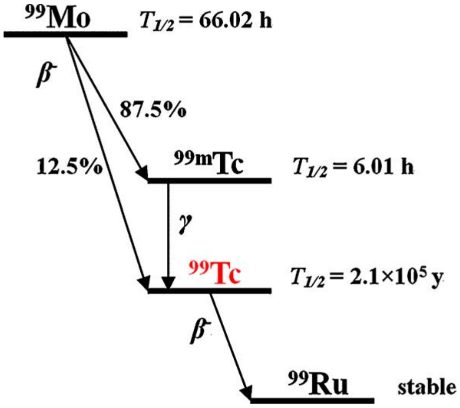

Figure 1-3. Decay scheme of ^{99}Mo [13].

^{99m}Tc, produced from ^{99}Mo, as shown in Figure 1-3, is the metastable isotope of ^{99}Tc and is widely used in nuclear medicine because of its short half-life and low radiation dose (E_γ = 142 keV) [14].

1.2.1 Redox chemistry

Tc is a redox-sensitive element and its solubility and mobility in water depends strongly on its oxidation state. Its electronic structure ([Kr]$3d^5 4s^2$) gives rise to a wide range of oxidation states from -1 to +7, with the lower oxidation states being rarer than the higher states [12]. In the environment, Tc is mostly found as Tc(VII) and Tc(IV), because these oxidation states are thermodynamically stable and can exist in aqueous solution [15]. Tc(VII) acts as a hard acid and, in aerobic environments, forms the pertechnetate ion TcO_4^-, which has a water solubility of approximately 11 mol/L, and remains stable in typical oxidizing conditions under a wide pH range [16], as shown in the Pourbaix diagram depicted in Figure 1-4. As a result, the pertechnetate ion is very mobile in groundwater.

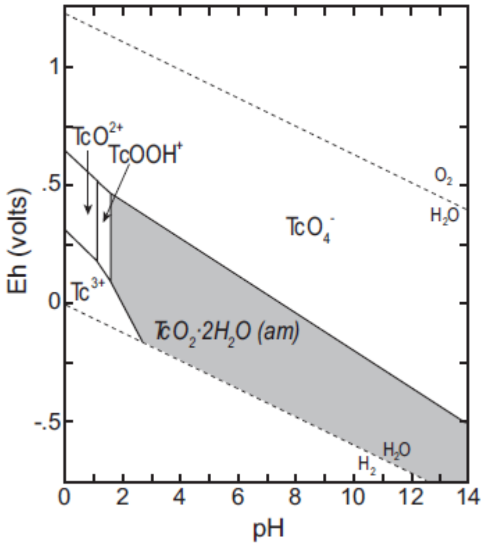

Figure 1-4. E_h-pH diagram for technetium [16].

Nevertheless, under strongly reducing conditions Tc(VII) can be reduced to Tc(IV) according to the reaction below [17] :

$$TcO_4^- + 4H^+ + 3e^- \rightarrow TcO_2 + 2H_2 \qquad 1$$

The presence of reductants, such as Fe(II), can also contribute to the reduction of Tc(VII) to Tc (IV) [12]. However, since TcO_2 is only sparingly soluble in water, the mobility and redox chemistry of TcO_4^- is very important, because it determines the environmental mobility of Tc.

1.2.2 Occurrence in the nuclear fuel cycle

Spent nuclear fuel is nuclear fuel that has been irradiated in a nuclear reactor but cannot sustain a nuclear reaction anymore. It mostly consists of uranium, the original ^{238}U and a little unreacted ^{235}U, as well as fission products. Spent nuclear fuel is reprocessed using the PUREX process (**P**lutonium **U**ranium **R**edox **Ex**traction) [18]. During this process, irradiated fuel (which contains technetium as a by-product of ^{235}U fission) is dissolved in concentrated nitric acid (HNO_3) and a 30% solution of tributylphosphate (TBP) in n-dodecane is used to extract U and Pu, as uranyl nitrate $UO_2(NO_3)$ and plutonium dioxide PuO_2, respectively.

Upon dissolution of the fuel, technetium solubilizes as TcO_4^- into the aqueous phase and is subsequently extracted into the organic phase in the first step of U and Pu extraction, as a result of the equilibrium below [14]:

$$UO_2(NO_3)_2(TBP)_2 + TcO_4^- \rightleftharpoons UO_2(NO_3)(TcO_4)(TBP)_2 + NO_3^- \qquad 2$$

In the second step of the extraction process, Pu and U are separated from each other by reductive re-extraction of Pu, generally, with U(IV) or Fe(II) in the presence of hydrazine. This process affords Pu(III), which is extracted into the aqueous phase, while U(VI) remains in the organic phase. The conditions used for this process may have a substantial impact on the fate of Tc. If an aqueous solution of U(IV) is used as the reducing agent, then Tc is partially re-extracted into the aqueous phase along with Pu while the complement remains in the organic phase. This is problematic as the TcO_4^- anions are capable of oxidizing both U(IV) and Pu(III). If Fe(II) is used as the reducing agent, then Tc is virtually completely extracted into the aqueous phase together with Pu and is not retained in the uranium-containing organic phase. Then, in the following step of Pu purification, Tc passes into aqueous intermediate level radioactive waste, from which it can be quantitatively extracted [19]. Although U and Pu are the main components in PUREX, it should be noted that the extraction of technetium can be significantly enhanced in the presence of zirconium [20].

The presence of measurable amounts of Tc in recycled Uranium is problematic because the production of UF_6 (for isotope separation during the process of enrichment with ^{235}U) may lead to the formation of TcF_6 which is highly volatile and is therefore easily discharged into the air. For this reason, quantitative transfer of Tc into only one waste stream is of great importance [14].

1.3 ^{99}Tc measurement methods

There are two broad groups of measurement methods for β-emitters such as ^{99}Tc. The first is the radiometric methods, which quantify the radionuclides in terms of their β-decay, and the second is the mass spectroscopic (MS) methods, which quantify the nuclides in terms of their mass/charge ratio. Usually, radiometric methods have lower cost and are easier to operate than the MS techniques. However, MS methods normally have lower detection limits and shorter counting time.

1.3.1 Radiometric methods

The radiometric methods that are normally used for the measurement of ^{99}Tc are liquid scintillation counting (LSC), gas ionization detectors and neutron activation analysis (NAA).

LSC is one of the most common radiometric methods used for the detection of ^{99}Tc [21]–[23]. In LSC, a purified sample is mixed with a liquid scintillation cocktail (LS cocktail), which consists of an aromatic solvent, a scintillator and a surfactant. The delocalized π-electrons of the aromatic rings are capable of absorbing the energy of the β-particle, which is then transferred to the scintillator and is re-emitted as a photon of a specific wavelength. The photon is then detected by a photomultiplier tube, which converts it into an electric current to quantify the β-emission. The role of surfactant is to keep the sample, which is usually dissolved in aqueous solution, in contact with the organic phase of the LS cocktail [23]. The main characteristics of LSC are that it has negligible self-absorption, no air absorption and no radiation scattering prior to incidence upon the detector, counting over the full solid angle of 4π, and short counting times. High-energy beta emitters can also be counted using an aqueous solution without any scintillators. This method, which is known as Cherenkov counting, relies on the detection of Cherenkov radiation directly by the photomultiplier tubes [24]. However, due to the relatively high background/blank counts, the detection limit is relatively high, thus restricting the determination of low levels of ^{99}Tc. It is also prone to colour and chemical quenching due to undesired chemicals in the final sample, meaning that any electronegative species will capture π electrons, reducing the efficiency of energy transfer [25]. A detection limit of 1.7 mBq g^{-1} with a count time of 2 hours has been reported [26].

Gas ionization detectors measure all the types of ionizing radiation. They consist of a tube containing an inert gas, usually argon. The ionizing radiation creates ion pairs; cations and electrons, in the volume of the gas. When an electric field is applied, the cations are attracted to a cathode and the electrons to an anode. The detectors are commonly constructed in such a way that the outer wall serves as the cathode and a grid in the middle of the gas volume serves as the anode. The count rate of the radionuclide is then determined by the collection of the electric charge [27]. The most common type of detector is the Geiger-Muller, which has been widely used for the detection of ^{99}Tc. In this technique, the sample must be in solid form, usually electrodeposited on metal disks, and as small as possible to minimize self-absorption [28]. A detection limit of 1.5 mBq with a count time of 4 hours has been reported [29]. However, since quantification is not possible and this is not a β-emitter selective method, and also because of its poor detection limit and long counting time it is seldom used for ^{99}Tc detection.

Neutron Activation Analysis (NAA) is based on the two nuclear reactions

$$^{99}\mathrm{Tc}\,(n,\gamma)^{100}\mathrm{Tc} \qquad \text{and} \qquad ^{99}\mathrm{Tc}\,(n,n')^{99m}\mathrm{Tc}$$

and the counting of ^{100}Tc (β-emitter, $t_{1/2}$ = 15.8 s). Because of the short half-life of ^{100}Tc, ^{99}Tc has to be separated from the sample prior to the irradiation. With this technique, a detection limit of 25 mBq has been reported [30]. Although this technique is theoretically more sensitive to ^{99}Tc, the low neutron activation cross section limits its analytical sensitivity, and as a result it is mostly used for high concentration sample of ^{99}Tc, such as nuclear waste [23].

1.3.2 Mass spectroscopic methods

As explained above, radiometric methods are limited by their long analysis times. MS methods normally offer faster analysis and lower detection limits. The most common techniques are inductively- coupled plasma mass spectroscopy (ICP-MS), accelerator mass spectroscopy (AMS), thermal ionization mass spectrometry (TIMS) and resonance ionization mass spectrometry (RIMS).

ICP-MS is one of the most frequently used techniques for the detection of ^{99}Tc in environmental samples [23], [25], [31], [32]. In ICP-MS, chemical compounds contained in the sample solution are decomposed into their atomic constituents in an inductively coupled argon plasma at a plasma temperature of approximately 6000–8000 K. The positively charged ions are extracted from the inductively coupled plasma (at atmospheric pressure) into the high vacuum of the mass spectrometer *via* an interface. The extracted ions are then separated by mass filters of either quadrupole type time-of-flight or combination of magnetic and electrostatic sector, and finally measured by an ion detector. ICP-MS is a rapid and sensitive method, suitable for the determination of low level ^{99}Tc. However, the main challenge of this analytical technique is the interferences of isobaric nuclei and molecular ions, most importantly of Mo and Ru, which also determines the detection limit. Shi *et al.*have reported a detection limit of 7.5 mBq m^{-3}, the equivalent of 11.5 pg m^{-3}, in sea water samples, after the complete separation of ^{99}Tc from the interferences with chromatographic extraction [33].

AMS is one of the most accurate and sensitive methods for the determination of low-level radionuclides in environmental samples, such as ^{99}Tc [23], [25], [34]. In AMS measurements, the isotope of interest must first be prepared in the form of a solid target. Then, negative ions are generated from the target by ion sputtering, usually by using a Cs^+ ion source, and pass through a magnetic sector where they are accelerated by a potential difference of several MV to a positive terminal. At the terminal, the negative ions pass through a thin foil or low-pressure gas and generate positive ions of high charge. They then accelerated back to ground potential where they pass through further electromagnetic selection and are finally measured by an ion detector (normally an ionisation chamber). In this method, the most important interference is the isobaric ^{99}Ru. At the stage of the ion sputtering, interferences that do not form negative ions can be eliminated. For this reason, the conversion of atomic ^{99}Tc to TcO^- anion is preferred to the Tc^- anion, since the yield of the equivalent RuO^- anion is low [35]. With this method, a detection limit of 0.8 pg L^{-1} in seawater samples has been reported [34]. However, due to the high cost of the equipment, there are less than 100 AMS facilities worldwide which mostly operate routine radiometric dating analysis of ^{14}C [23].

In TIMS, the target nuclide must be in the form of an aqueous solution, usually dissolved in 0.5-1 M HNO_3. About 0.5-1 µL of the solution, containing only a few hundreds of ng of the element of interest, are transferred onto a sample filament, usually made of high purity rhenium, and dried by a current of 1 A. The evaporated atoms are then ionized by another filament arranged opposite of the first one, and finally the generated ions are accelerated and focused into a mass analyzer [36]. TIMS has probably achieved one of the lowest detection limits in ^{99}Tc measurement, containing as low as 5 µBq, the equivalent of 7×10^{-15} g, as reported by Rokop *et al.*[37].

Finally, in RIMS, instead of the filament method, a laser ion source is used. The laser ion source contains many cavities with a small hole to inject the laser beam and to extract the ions. In that way, the ^{99}Tc atoms are confined inside the cavity and can interact for a longer time with the laser light. The wavelength of the laser plays a major role in the ionization efficiency [38]. A detection limit of about 10^{-14} g has been reported with the implementation of RIMS [39]. However, there are currently no commercially available with RIMS equipment, making this method quite rare compared to other MS methods, like ICP-MS.

1.4 ^{99}Tc separation methods

The precision of an analytical measurement method for ^{99}Tc depends on its separation level from interferents and other matrix components. Because of the very low concentration of ^{99}Tc in the environmental samples, usually large sample volumes are required in order to obtain adequate signal. This means that the technique for the chemical separation of ^{99}Tc should not only provide sufficient removal of interferences, but also a high chemical yield of ^{99}Tc. However, the difference between the methods of detection, requires separation from different interferences. Radiometric methods require that all other β-emitting radionuclides to be removed, while for the measurement with mass spectrometry, the isobaric and molecular ions of mass 99 ± 1 pose the main challenge [40], the most important of which being ^{99}Mo and ^{99}Ru [35]. The main interferent for both radiometric and mass spectroscopic methods are presented in Table 1.2. The most common methods of chemical separation and purification of ^{99}Tc are co-precipitation, liquid-liquid extraction and extraction chromatography [25],[39],[40]. These techniques are summarized below.

Radiometric methods [43]	
Nuclides	Β-max energy (keV)
^{60}Co	318.1
^{63}Ni	66.9
^{90}Sr	546.0
^{103}Ru	226.6

Mass spectrometric methods [23]	
Isobaric/molecular ions	Natural abundance (%)
^{98}Mo	24.1
^{100}Mo	9.6
^{99}Ru	12.7
^{100}Ru	12.6

^{106}Ru	39.6	$^{98}Mo^{1}H$	24.6
^{110m}Ag	529.8	$^{83}Kr^{16}O$	11.5
^{125}Sb	303.3	$^{51}V^{16}O_3$	99.8
^{137}Cs	514.0	$^{59}Co^{40}Ar$	100

Table 1.2. The most common interferences in the measurement of ^{99}Tc using radiometric and mass spectroscopic methods.

1.4.1 Co-precipitation

As mentioned earlier, under reductive conditions, ^{99}Tc mainly exists in the +IV oxidation state, which easily forms insoluble species of $TcO_2 \cdot H_2O$. As a result the reduction of the soluble Tc(VII) to the insoluble Tc(IV) has commonly been used to separate it from the sample matrix. This can be achieved usually by co-precipitation with a carrier such as $Fe(OH)_2$ or FeS [44]. The sample is first acidified in HCl and reductive agents such as $FeSO_4$ are then introduced which lead to the reduction and co-precipitation of Tc(IV) with $Fe(OH)_2$ [45]. However, ^{99}Tc must then be transferred back into aqueous solution for further separation, this is achieved by oxidation back to Tc(VII by a range of oxidizing agents such as H_2O_2 or $K_2S_2O_8$, which lead to the precipitation of other transition metals and lanthanides, while keeping TcO_4^- in solution [41]. Although co-precipitation is a very simple method, low recovery of ^{99}Tc might be expected in the analysis of large volumes in addition to low decontamination factor, and in practice, it is mostly used to separate ^{99}Tc from major interferences and pre-concentrate the sample before further purification.

1.4.2 Solvent extraction

Several solvents have been studied for the separation of ^{99}Tc from other radionuclides, but the most commonly used are tributylphosphate (TBp), triisooctylamine (TIOA) and cyclohexane.

As was detailed in section 1.2.2, TBP has been widely used in plutonium-uranium extraction in PUREX process during the spent fuel reprocessing, but it is also used for the separation of ^{99}Tc [46]. The mechanism behind the separation is the following. In acidic conditions, TcO_4^- is protonated forming the neutral molecular species $HTcO_4$ which forms a complex with TBP. Relatively low concentrations of aqueous solutions of HNO_3 or H_2SO_4 can be used for this process, however it has been shown that H_2SO_4 offers higher yield of $HTcO_4$ and better distribution coefficient of the species in TBP [47]. Also, TBP has been reported for the extraction of medical ^{99m}Tc, which decays to ^{99}Tc, from urine [48]. After extraction, the organic phase is usually washed with an aqueous solution of NaOH in order to retrieve ^{99}Tc back into the aqueous phase. Although ^{99}Tc can be extracted by TBP in high yield, its separation from Ru is not sufficiently efficient [40].

The use of TIOA for the extraction and separation of ^{99}Tc was first reported by Golchert and Sedlet [49]. The authors reported the formation of a neutral complex of TcO_4^- with TIOA at low acid concentrations which was extracted in the organic phase by a 5% volume ratio TIOA/xylene mixture from 0.5 mol L^{-1} H_2SO_4, and was then easily retained in the aqueous phase with a low NaOH concentration [49]. Later reports suggested that Ru, which is the main interferent, can be effectively removed in this way. When a mild oxidizing reagent, such as H_2O_2, is used at low concentration of H_2SO_4, Tc is oxidized to TcO_4^-, while keeping Ru in a lower oxidation state, which cannot be extracted into the organic phase. In this way, the distribution coefficients obtained between the 5% TIOA/xylene mix and the 0.5 mol L^{-1} H_2SO_4 solution for ^{99}Tc and Ru are 2.5×10^3 and 3.8×10^{-3} respectively. The overall chemical recovery of ^{99}Tc in this process was found to be around 70% [50].

Effective recovery of ^{99}Tc and decontamination from Ru in soil samples has also been reported with the application of cyclohexane. The authors demonstrated that, when the sample solution is treated with 30% H_2O_2 in 1 mol L^{-1} K_2CO_3, extraction of ^{99}Tc by cyclohexane can lead to a decontamination factor of 7.0 x 10^4 for Ru, with a chemical recovery of about 80% for ^{99}Tc [51]. However, later studies showed that removal of Mo with cyclohexane is not adequate [52].

Although solvent extraction offers relatively good selectivity in the separation of ^{99}Tc, it is very time-consuming and requires large volumes of hazardous organic solvents, thus producing large amounts of waste. So, in recent years, it is gradually being replaced by chromatographic techniques.

1.4.3 Extraction chromatography

Extraction chromatography is among the most common methods for the extraction of ^{99}Tc from environmental samples. In this method, the solution containing dissolved TcO_4^- is eluted through a column containing a material that can selectively retain technetium. The technique works either *via* adsorption of ^{99}Tc to porous materials or via anion exchange with anion exchange resins. Activated carbon has been used as an adsorbent in several previous works [53]–[56], with a reported adsorption of up to 99% [53]. However, activated carbon is mostly used for remediation purposes because it is not a selective material, so it cannot be used for accurate detection.

For this reason, several anion exchange resins have been developed which demonstrate high selectivity towards ^{99}Tc. An example is AnaLig Tc-02 gel, by IBC Advanced Technologies. Previous works have reported a chemical recovery of 95.7% for ^{99}Tc. To achieve this, the authors first eluted the resin columns with a NaCl solution in order to adjust ion strength, before eluting ^{99}Tc with hot deionized water ~90 °C [57],[58]. Another example of a strong basic anion exchange resin is Bio-Rad AG1, which has been reported for very high selectivity for TcO_4^- under a wide range of pH, due to its higher affinity compared to other common anions in environmental samples, such as Cl^-, NO_3^- and CO_3^{2-} [43]. Macro-pore anion exchange resins have also been applied, such as

Amberlite IRA-400, which has been reported for the effective decontamination from Mo prior to ICP-MS measurement [59].

However, the most widely used anion exchange resin for the separation of ^{99}Tc is TEVA, by Eichrom Technologies Inc [31], [57], [60]–[63]. The active group of TEVA resin is a trialkyl methyl ammonium salt, also called Aliquat 336, shown in Figure 1-5, which is incorporated into an inert polymeric support substrate. It was developed by Horwitz et al., who also investigated systematically its characteristics, kinetics and elution behaviour and demonstrated a high Tc(VII) retention at low acid concentrations [60].

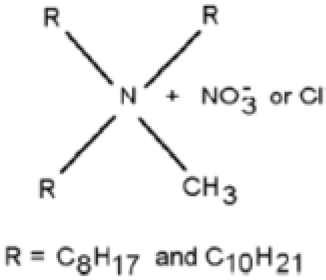

Figure 1-5. The active trialkyl methyl ammonium salt of TEVA resin, also called Aliquat 336.

The capacity factor k’ for Tc(VII) and several tri-, tetra-, peta-, and hexavalent actinides versus HNO_3 and HCl concentrations is shown in Figure 1-6. At low HNO_3 concentrations the retention of Tc(VII) is much greater than that of any actinide, while this difference is even more significant at low HCl concentrations [60]. Later studies also reported significant separation from Mo and Ru, due to the difference in the affinity of TEVA resin towards TcO_4^- compared to that of MoO_4^- and RuO_4^- [64].

For the effective separation of ^{99}Tc with TEVA resin the sample must be prepared in low concentration of HNO_3, typically 0.1 mol L^{-1}. It is then eluted through a chromatographic column loaded with TEVA resin, where TcO_4^- is retained while all other interferences are removed. To retrieve and measure the captured TcO_4^-, the column is then eluted with high concentration HNO_3, usually 8 mol L^{-1}.

More recent research has reported that the use of TEVA resin in the form of coated dip-sticks, which offers more rapid separation and determination, can also lead to quantitative uptake of ^{99}Tc [63]. This report suggests that TEVA resin can also be used for the effective detection of ^{99}Tc in techniques that do not rely on extraction chromatography.

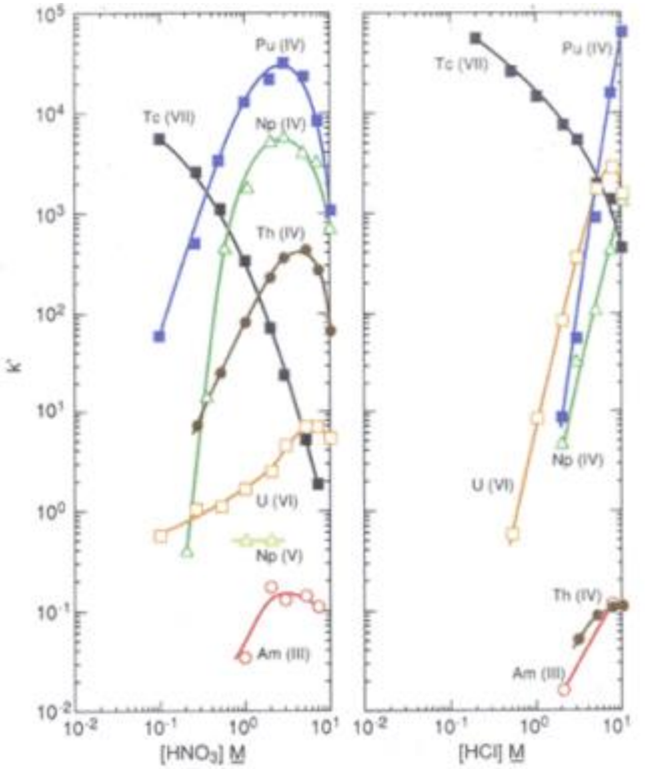

Figure 1-6. The capacity factor k' for Tc(VII) and for various actinides plotted against acid concentration, taken form Horwitz et al. [60].

1.5 Molecular receptors and ligands for TcO_4^-

The previous section summarized the most common methods for the separation of ^{99}Tc from interferences. Other molecular receptors such ligands, as well as porous materials exist. These have been applied to the capture of TcO_4^-, mostly by adsorption through anion exchange or the use of other intramolecular interactions, such as hydrogen bonding. These materials are reviewed in this section.

1.5.1 Inorganic materials

Inorganic materials, such as zeolites and layered double hydroxides (LDHs), have also been used in ion exchange processes. Zeolites comprise framework-based porous structures that can accumulate a wide variety of cations, while LDHs are a group of anionic clay formed by positively charged layers of metal hydroxides, with weakly bound anions between the layers [65]. The adsorption of TcO_4^- on these materials depends on their composition, structure and crystallinity. It has been reported that a highly crystalline Ni-Al-LDH system showed much higher TcO_4^- sorption when the interlayer anion in presence was NO_3^- than with CO_3^{2-}, because of the thermodynamic stability due to the strong interlayer binding of CO_3^{2-} [66].

In a similar fashion, a thorium based material, NDTB-1 (NDTB = Notre Dame Thorium Borate-1) of formula $[ThB_5O_6(OH)_6][BO(OH)_2]\cdot 2.5H_2O$, has been reported [67], [68] which shows excellent TcO_4^- removal efficiency from water, NDTB-1 is a porous supertetrahedral 3D framework built from twelve coordinate Th^{4+} ions surrounded by BO_3^{3-} and BO_4^{5-} anions. The BO_4^{5-} anions chelate the thorium centers, and the BO_3^{3-} groups occupy single vertices. The borate anions further polymerize to form $B_{10}O_{24}$ clusters. The bridging of thorium centers with borate clusters creates a supertetrahedral framework, with a system of channels and cages, as shown in Figure 1-7. The charge balancing $H_2BO_3^-$ anions are present within these channels. The extra-framework, weakly bound $H_2BO_3^-$ anions can readily hydrolyze back to H_3BO_3 at a wide range of pH levels owing to the weak acidity of boric acid. As a result, other anions can readily get inside the channel of NDTB-1 for charge balancing [68].

NDTB-1 shows a high selectivity towards the capture of TcO_4^-, even in the presence of significant excess of other common anions such as Cl^- and NO_3^-, by trapping it within the cavities, while the other anions remain mobile. Its anion exchange capacity was reported to be 162.2 mg g^{-1}. Furthermore, TcO_4^- can be exchanged reversibly out of the framework with anions of higher charge/radius ratios, such as PO_4^{3-} and SeO_4^{2-}, thus making NDTB-1 reusable [67].

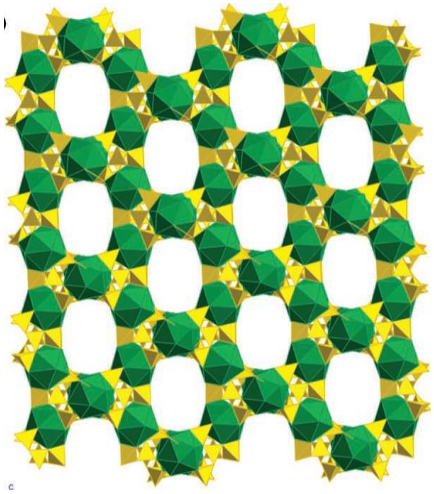

Figure 1-7. A view of the supertetrahedral framework structure of NDTB-1 with channels along cubic [110] directions [67].

1.5.2 Organic materials

Several organic molecular receptors have been developed and applied for the separation of TcO_4^-. In most cases, the removal works though weak electrostatic interactions with an active group of the molecule or by hydrogen bonding. Its low hydration energy, and charge/radius ratio, make TcO_4^- easy to be removed from aqueous phases by a relatively hydrophobic receptor, unlike other oxyanions such as SO_4^{2-} and PO_4^{3-} [65]. These organic hosts can be either cation or anion selective, depending on their chemical nature. An alternative approach to the anion recognition is the selective entrapment of counter cations. Because cations possess lower solvation energies than anions, they are easier to trap, as the related energy penalty is comparatively lower.

An example of TcO_4^- capture through counter cation interaction is given by a crown ether, bis-4,40(50)[(tert-butyl)-cyclohexano]-18-crown-6 [65], [69], the structure of which is shown in Figure 1-8. The crown ether was used in TBP solvent and the mechanism of extraction was reported to be that of the crown formed a complex metal cations such as Na^+, K^+ or Sr^{2+} and TcO_4^- was co-extracted in order to preserve charge neutrality. Its great advantage is that this process works under alkaline conditions, so it can be applied directly into the waste stream, without the need for acidification. However, this method is not selective, as other anions, such as NO_3^-, could be co-extracted [65], [69].

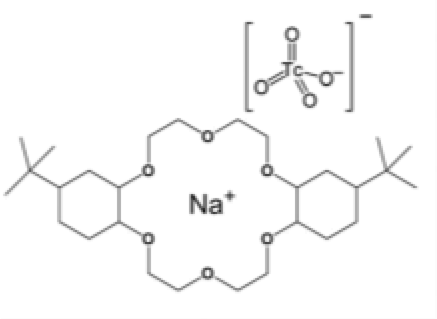

Figure 1-8. The structure of crown ether bis-4,40(50)[(tert-butyl)-cyclohexano]-18-crown-6 [67].

More selective behaviour can be achieved by receptors that can bind both to the anion and cation. Beer *et al.* have reported on a tris(2-aminoethyl)amine (TREN) derivative with crown ethers, called tris(amido benzo-15-crown-5) and shown in Figure 1-9, that can selectively bind Na^+ and TcO_4^-, even in the presence of an excess of chloride [70]. The crown ethers formed a complex with Na^+, while TREN acted as the binding site for TcO_4^-, through H-bonds with the amine hydrogens. The authors reported that the metal cation could also affect the spatial arrangement of the ligand, which could enhance its relative acidity, leading to stronger H-bonds with TcO_4^-. In fact, in the absence of Na^+, the ligand binds strongly with Cl^-, while addition of Na^+ led to significantly higher selectivity towards ReO_4^-, which was used as a surrogate to TcO_4^- [70].

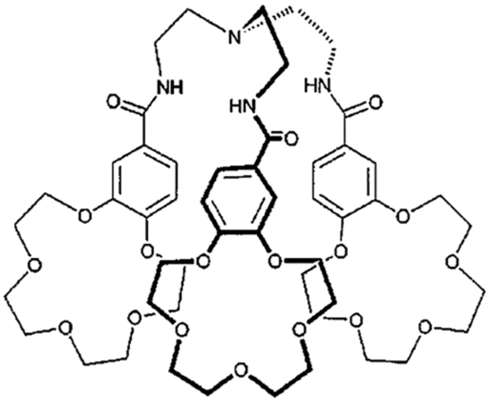

Figure 1-9. The tripodal tris(amido benzo-15-crown-5) ligand [70].

Another derivative of TREN, the azacryptand ligand LH_6^{6+} [71] shown in Figure 1-10, has been reported for the selective binding of TcO_4^-. With this ligand, the binding occurs in acidic environments (pH = 2) when the 6 amine groups are protonated, leading to an overall positive charge of +6. It was found that the large TcO_4^- selectivity over other anions such as NO_3^- and Cl^- originates from the formation of a 1:1 adduct under experimental conditions. Therefore, one TcO_4^- ion within the cavity interacts with the host molecule through intramolecular H-bonding [71].

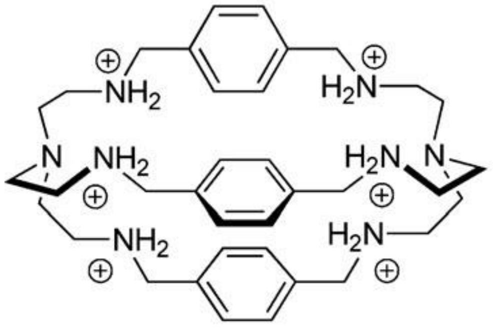

Figure 1-10. The azacryptand ligand LH_6^{6+} [71].

The above examples demonstrate that TREN can form ligands that exhibit great affinity towards TcO_4^-. This concept will be explored in later chapters.

1.5.3 Metal-organic frameworks (MOFs)

Metal organic frameworks (MOFs) also known as porous coordination polymers (PCPs) are highly porous and crystalline complexes comprised of metal centers and organic linkers and are usually synthesized by hydrothermal methods. Originally fabricated for applications in gas storage, gas separation and catalysis, in recent years these materials have been used in separation applications [72][73]. In contrast to amorphous materials, MOFs provide a periodic and strictly defined structural network that can host guest molecules, thus permitting systematic investigation [74].

MOFs have been applied in numerous previous works for the effective adsorption and removal of CO_2 and other harmful gasses such as CO, SO_2, H_2S and NH_3 [73], [75]. The structure and composition of a MOF plays a vital role in the capacity and selectivity of the gas adsorption. For example, Dietzel *et al.* have reported that the metal center can affect the capacity and selectivity towards CO_2. The authors reported that from a series of isostructural MOFs M-CPO-27s (where M = Ni, Co, Zn, Mn, Mg), the total uptake of CO_2 for Mg-CPO-27 was 63% while for Ni-CPO-27, it decreased to 51% [76].

The adsorption of heavy metal ions in MOFs has also been studied. Ke *et al.* have reported the adsorption of Hg^{2+} from water into a thiol-functionalized Cu-BTC, with a very high adsorption capacity of 714 mg g^{-1} [77]. Effective removal of As^{5+} under a wide range of pH was also reported by a Fe-BTC MOF, where the adsorption took place through the formation of Fe-O-As bonds [78].

However, more recent studies have suggested the adsorption of anions in aqueous solutions, through anion exchange of the anion of interest with the counter anion of the metal center of the MOF. In this concept, Oliver *et al.* reported on the effective adsorption and removal of ClO_4^- from aqueous solutions with a Ag(4,4'-bipyridine)NO_3 MOF [79]. The experiments were carried out by immersing and stirring the bulk MOF crystal into aqueous solution $NaClO_4$. The authors then reported that ClO_4^- anions were adsorbed into the framework by exchanging the weakly bound NO_3^- between the cationic Ag(I)-4,4-bipyridine chains. They also demonstrated that this process was reversible by exchanging the NO_3^- anion back into the framework through immersion of the bulk crystals in high concentration $NaNO_3$ solution [79].

In a later study, Zhu et al.used the same Ag(4,4'-bipyridine)NO_3 MOF to test the adsorption of ReO_4^- anions, which is the non-radioactive chemical surrogate of TcO_4^- [80]. The structure of the MOF was characterized by XRD and it was found that each Ag^+ cation is coordinated by two neutral 4,4-bipyridine ligands, while each 4,4-bipyridine connects two Ag^+ cations within the framework, leaving weakly coordinated NO_3^- in the open space as the counter anion. The authors reported that ReO_4^- was adsorbed into the MOF by replacing NO_3^- as the counter anion in the framework, just by soaking bulk crystals in aqueous solutions containing certain amounts of ReO_4^-. The adsorption capacity was found to be around 714 mg g^{-1}, which was stable under a pH range of 5-9, while the selectivity towards ReO_4^- was tested with significant excess of NO_3^-, which is a very common anion in nuclear waste. It was shown that even in the presence of 100-fold NO_3^-, the removal of ReO_4^- was still as high as 90%. However, this anion exchange was shown to be irreversible since it led to a more thermodynamically stable structure in which the crystals have significantly rearranged from an octahedral morphology to needle-like structures, as shown in Figure 1-11. The irreversibility of the process was shown by immersing the exposed bulk crystals to high concentrations of NO_3^-. Unlike in the case of ClO_4^-, the reverse anion exchange was not observed [80].

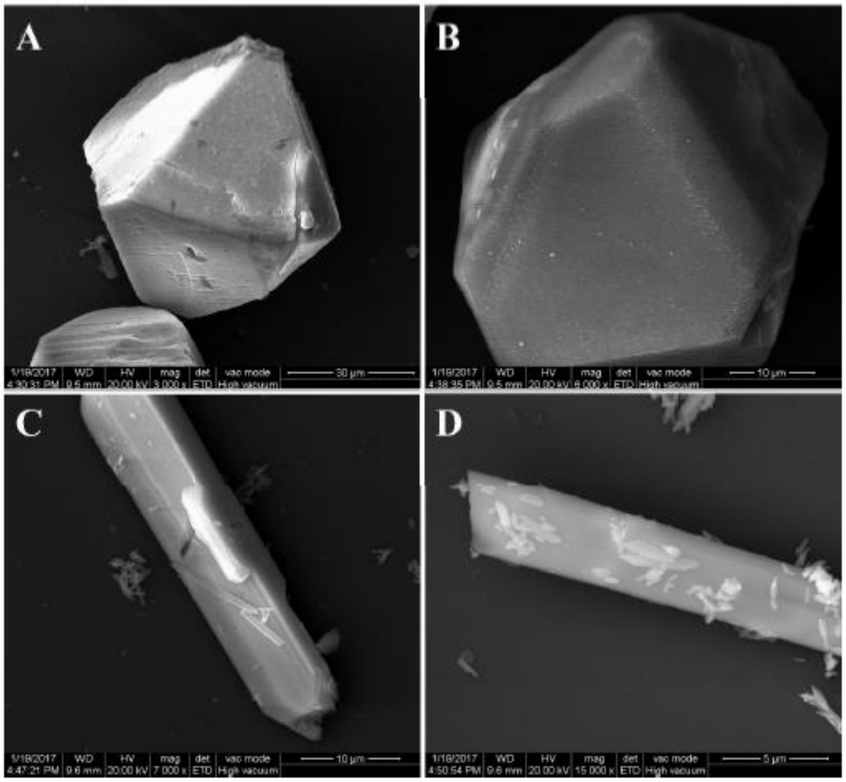

Figure 1-11. SEM images of Ag(4,4-bipyridine)NO_3 (A,B) and Ag(4,4-bipyridine)ReO_4 (C,D), taken from Zhu et al.[80].

Although this MOF shows great anion exchange selectivity towards ReO_4^-/TcO_4^-, it could only serve as a sequestering agent, rather than for detection purposes, since the process of adsorption is irreversible. For this reason, other ways which could exploit this MOF's exceptional selectivity for faster detection of ReO_4^-/TcO_4^- will be explored in later chapters. One of these is to employ the MOF in the form of a thin film on a substrate, as we will return to later.

In summary, molecular receptors that have exhibited strong anion exchange selectivity towards TcO_4^- were reviewed in this section. These included both inorganic and organic materials, as well as MOFs. However, in most cases they served either as separating or immobilizing agents, rather than as detectors. In order to transform their selectivity towards TcO_4^- to real time detection, the real time monitoring of the anion exchanging adsorption is essential. This could be achieved through the Quartz Crystal Microbalance (QCM), which will be described in the next section.

1.6 Quartz Crystal Microbalance (QCM)

As detailed in the previous sections, the currently used methods for the measurement of ^{99}Tc are very time consuming and costly. The low concentration of TcO_4^- in environmental samples require several separation steps, typically taking up to a week, to be carried out prior to analysis. Since the continuous and rapid monitoring of ^{99}Tc in groundwater would allow the identification of and immediate response to any potential contamination events, novel, faster and more cost-effective methods are needed. The Quartz Crystal Microbalance (QCM) can combine the separation and measurement into a single step since it can detect small changes of mass on its surface through adsorption or desorption, while functionalization with selective materials can help it target specific analytes in the adsorption process. The theory and method of operation of the QCM, as well as its applications are described below.

1.6.1 Principles of QCM

The mode of operation of the QCM is based on the piezoelectric effect, discovered by Pierre and Jacques Curie in 1880. This phenomenon is observed when a mechanical stress is applied to certain crystals (such as quartz) which produces a change in the electrical potential with a magnitude proportional to the applied stress [81]. This is a reversible effect, which means that if an electric potential is applied to the same crystal, then a mechanical deformation is observed. According to this effect, Walter Guyton Cady later found that applying an alternating electric field across a quartz crystal resulted in an alternating strain being applied on the quartz, thus leading to the development of a stable oscillator [81].

In this sense, the QCM comprises of a quartz crystal (typically about 300 μm thick), coated with one gold electrode on each side, as shown in Figure 1-12. The gold electrodes provide the AC field that causes the quartz to oscillate at a certain resonant frequency f_o.

Figure 1-12. The front side of the QCM, on the left-hand side, and the back side of the QCM, on the right-hand side. The diameter of the QCM is 14 mm.

From the electrical point of view, the QCM can be modelled by the generic Butterworth-Van-Dyke circuit model, which consists of a series *RLC* motional arm, where C_m represents the energy stored per oscillation, L_m represents the inertia of the vibrating mass of the crystal and R_m represents the energy loss per oscillation, as shown in Figure 1-13. The additional C_o in parallel accounts for the crystal acting as a dielectric material, forming a capacitor [82].

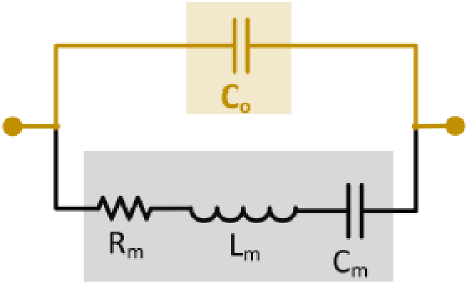

Figure 1-13. The Butterworth-Van-Dyke circuit model [82].

The series resonant frequency f_s of the above circuit, is calculated according to equation 3:

$$f_s = \frac{1}{2\pi\sqrt{L_m C_m}} \tag{3}$$

This serves as the resonant frequency f_o of the QCM. By monitoring the changes in the resonant frequency, changes of mass on the surface of the QCM can be detected. When the mass on the surface increases, the frequency decreases and *vice versa*. The quantitative relationship between the change of frequency and the change of mass is given by Sauerbrey's equation [83]:

$$\Delta f = -\frac{2f_o^2}{A\sqrt{\rho_q \mu_q}}\,\Delta m = -C_f\,\Delta m \tag{4}$$

Where A is the piezoelectric area sandwiched between overlapping area of the two electrodes, ρ_q is the density of the quartz, μ_q is its shear modulus and f_o is the resonant frequency of the QCM. The whole fraction can be substituted by the calibration factor C_f, which can be acquired by calibration experiments.

As previously discussed, the surface of the QCM can be coated with materials, usually in the form of a film, that can selectively adsorb or bind specific analytes. In this way, the QCM is modified to an efficient sensor by monitoring the change in the mass of the coating due to the adsorption, through the changes in the resonant frequency.

1.6.2 QCM coatings

Several types of coating materials have been applied on the surface of QCMs over the past two decades, including self-assembled monolayers (SAM), MOF thin films, molecular imprinted polymers, calixarenes, graphene, hydrogels, ionic liquids and metal oxides. A summary of these coating is presented below.

1.6.2.1 Self-assembled monolayers

Self-assembled monolayers (SAM) consist of a single layer of molecules on a substrate, the gold electrode in the case of the QCM. Those are usually long chain organic molecules, typically alkanethiols with at least ten carbon atoms. On the QCM, SAMs generally rely on the formation of Au-S bonds, which form spontaneously when the gold substrate is immersed in a solution of the thiol compound [84]. The ordered arrangement of the layer is thought to begin with the alkanethiols binding almost parallel to the gold surface, until there are enough molecules to interact with each other so that the carbon chains lift from the surface while remaining tethered to the gold through the thiol group. In the end, the gold electrode is covered by a monolayer in which the alkanethiols extend at an angle of 30^o from the surface [85]. On the distal end of the SAM there is an active group, such as amine, hydroxyl, carboxyl or amide groups that can immobilize selectively specific analytes, or even provide the basis of further functionalization.

1.6.2.2 Metal organic frameworks thin films

Recently, Metal Organic Frameworks (MOF) have been deployed as thin films in a number of applications in the fields of nanotechnology, energy storage and sensors. While the structure and size of the bulk crystals is not directly controlled in the traditional synthetic methods employed for MOFs, they can be adjusted in the preparation of thin films whose thickness can also be controlled [86]. Several processes have been developed for the preparation of MOF thin films, such as electrochemical deposition, chemical vapour deposition and powder deposition [87], although the most widely used is liquid phase epitaxy or layer-by-layer (LbL) assembly [86]–[90].

In LbL assembly, the substrate onto which the film is developed must first be functionalized with a SAM, terminated by a functional group, such as a carboxylic acid, hydroxyl or pyridine group. These functional groups can then anchor either the metal or the organic linker, thus nucleating the growth of the MOF thin film on the substrate and controlling its orientation [86]. The film is then built layer-by-layer by alternately immersing the functionalized substrate in solutions of low concentration containing the metal precursor and the organic linker, while the unreacted or any physically absorbed elements are removed by rinsing between the steps, as shown in Figure 1-14. With this method, the thickness of the film is controlled by the number of cycles, while the film is chemically attached on the substrate.

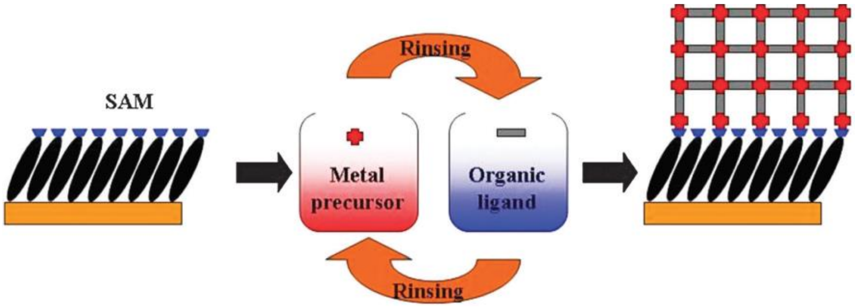

Figure 1-14. Schematic representation of the LbL assembly. The SAM functionalized substrate is alternately immersed in the metal precursor solution and then in the organic linker solution, after rinsing in between. The cycle is repeated several times until the thickness of interest is achieved. Taken from Shekhah et al. [89].

It is worth noting that the exposed functional group can interfere in the orientation of the film. Biemni *et al.* demonstrated that the growth of the MOF thin film $Cu_3(btc)_2$ (btc = 1,3,5 benzyntricarboxylate), also called HKUST-1, varied according to the different SAM on the substrates, which were gold slides modified with $HS(CH_2)X$ (where X = -COOH and -OH). The authors showed that the film was induced in the [100] direction on the -COOH terminated SAM and in the [111] direction on the -OH terminated SAM [91].

There are numerous reports on the fabrication of highly crystalline MOF thin films using the LbL assembly method, which have been used in many different applications [87], [88]. Generally the authors report variation in the behaviour of the thin film compared to that of the bulk. For example, a Ru-btc MOF thin film has been reported as sensitizer to harvest solar radiation in photovoltaic devices. The film was prepared on an amine functionalized glass slide by alternately dipping it in 10 mM $RuCl_3$ in CH_3COOH aqueous solution and in 10 mM H_3btc in CH_3COOH aqueous solution, while XRD analysis showed similar patterns for the bulk crystals and the thin film [92]. In a similar manner, Otsubo *et al.* reported on the fabrication of a $Fe(py)[Pt(CN)_4]$ (where py = pyridine) thin film, built on a gold substrate functionalized with a 4-mercaptopyridine SAM by successively immersing it in ethanolic solutions of $Fe(BF_4)2{\cdot}6H_2O$, $[(C_4H_9)_4N]_2Pt(CN)_4$, and pyridine , with perfectly controlled orientation and high crystallinity [93]. Later studies on the same $Fe(py)[Pt(CN)_4]$ thin film revealed different sorption properties than the bulk crystals of the same MOF. The authors of the study reported that the film exhibited selective guest uptake in contrast to the bulk crystals [94]. Other MOF thin films have been also reported for the selective adsorption of volatile organic compounds, such as the $[Cu_2(ndc)_2(dabco)]$ thin film. Liu *et al.* reported two different films, one fabricated on a pyridine SAM and the other on a carboxylate-terminated SAM, which led to different orientation of the film. The adsorption of benzene, toluene and xylene into the film was tested and it was found that the orientation played a significant role to the selectivity and kinetics [95].

The above examples suggest that MOF thin films can be used for adsorption purposes, while their selectivity can be directly controlled. While many studies have considered the ion exchange properties of bulk MOFs, no work has focused on this aspect for thin film MOFs. This project aims to address that gap by focusing on the interaction of the pertechnetate ion and a thin film of the previously mentioned Ag(4,4-bipyridine)NO_3 MOF, coated on the gold surface of the QCM.

1.6.2.3 Hydrogels

Hydrogels are crosslinked polymers, usually made of acrylamide monomers, which consist of a 3D insoluble network. They are highly hydrophilic and have high density capacity due to their flexible matrix structure. Hydrogel thin films on QCM have been reported in previous works. Sadman *et al.* reported that a copolymer consisting of Nisopropylacrylamide and 2-(N-ethylperfluorooctanesulfonamido)ethyl acrylate was coated on a QCM via spin coating, where the thickness of the film was controlled by the angular speed and time of the spin coating [96].

1.6.2.4 Molecularly imprinted polymers

Molecularly imprinted polymers (MIPs) are synthetic receptors that have built-in selective recognition cavities that mimic the properties of natural antibodies. MIPs are synthesized via a polymerization reaction which takes place in the presence of the target analyte, which serves as a template. The monomers surround the target analyte though weak interactions with its functional groups and polymerize around it, thus producing a 3D structure around the template analyte. After the analyte is eluted from the matrix, recognition cavities are left within the structure that reflect the shape and the positions of the functional groups of the analyte. Consequently, the MIP can selectively immobilize the target molecule though weak interactions in the recognition cavities [97].

QCM crystals can be functionalized with MIPs either by synthesizing them separately as nanoparticles and immobilizing on the electrode, or by directly forming the polymer on the sensor *via* electropolymerisation. The second approach is usually preferred because it creates homogeneous thin films on the QCM surface which minimizes the swelling effect of the layer [98].

1.6.2.5 Graphene

Graphene is a 2D material which consists of sp^2-hybridized carbon atoms arranged in a planar hexagonal lattice and has a thickness less than 1 nm [99]. It is commonly synthesized though chemical vapor deposition, a technique used to deposit solid material on a substrate via a heating and a cooling process. During the heating process, the substrate, which is usually a transition metal, such as Cu, is exposed to a hydrocarbon precursor. The carbon radicals produced by the hydrocarbon decomposition diffuse on the metal surface and then form graphene during the cooling process [100]. QCM crystals can be coated with graphene through a transfer process by using polymethyl methacrylate (PMMA) as a supporting membrane. Typically, graphene grown on a Cu substrate is coated with PMMA and immersed in $FeCl_3$ aqueous solution in order to etch the Cu substrate away. Once removed from the substrate, the PMMA-supported graphene is then transferred onto the QCM and the PMMA is removed with acetone washes [101].

The oxidized form of graphene, graphene oxide (GO), is not uniformly planar and contains functional groups such as carboxyl, epoxy and hydroxyl on the edge of the carbon sheets. It is commonly synthesized by oxidizing graphite powder and exfoliating GO in the liquid phase. QCM crystals are then functionalized with GO via spray coating, spin coating or drop casting [102].

1.6.2.6 Calixarenes

Calixarenes are macrocyclic compounds bearing multiple aromatic rings. Their structure forms a cavity that can host guest molecules, such as different organic compounds and metal ions. The selectivity can be tuned by the number of aryl fragments and the presence of different functional groups in the rings, since they affect the shape and size of the cavity. In Figure 1-15, the general structure of calixarenes is shown. They are usually coated on the QCM via dip coating or thermal evaporation in vacuum [103], [104].

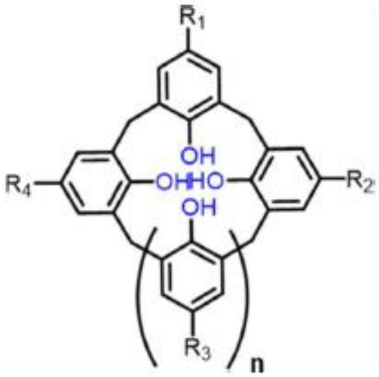

Figure 1-15. Typical structure of calix(n)arenes, where n is usually 4 and higher [103].

1.6.2.7 Metal oxides

Metal oxides are robust materials, resistant to physical and chemical deformation effects, but very sensitive to any physicochemical changes in the environment, and thus have been used in many applications such as gas sensing, solar cells, thin film transistors and anti-corrosion coating [105]. Several transition metal oxide films have been coated on QCM surfaces, such as TiO_2, MoO_3, ZnO, WO_3 or CeO_2, either through wet chemistry, electrodeposition or pulsed layer deposition [105], [106].

1.6.3 QCM based sensors

The QCM can be transformed into one of the most efficient sensing devices thanks to its real time rapid response and low cost. All aforementioned coating materials have been reported on the development of QCM-based sensors for the detection of numerous analytes, such as volatile organic compound, gases, heavy metals, anions, or even biological molecules. Thus, the capabilities of the QCM based sensors will be reviewed in this section.

1.6.3.1 Detection of volatile organic compounds (VOCs)

Volatile organic compounds (VOCs) are organic compounds that evaporate under normal conditions, and include light hydrocarbons, alcohols, ethers, esters, halocarbons etc. They are of great concern due to their high toxicity and links to global warming. Traditionally, gas chromatography and mass spectrometry are the most commonly employed techniques for the detection and quantification of VOCs. However, those techniques require expensive equipment and are time consuming. For this reason, the detection of VOCs is a significant focus of QCM-based sensors [103], [107]. A selected number of examples are reviewed below.

A QCM sensor coated with a MIP consisting of styrene, methacrylic acid and ethylene glycol has been reported for the detection of formaldehyde, with a detection limit as low as 500 ppb [108]. The authors recorded frequency drops that were proportional to the concentration of the formaldehyde exposed to the coated QCM, as it is shown in Figure 1-16.

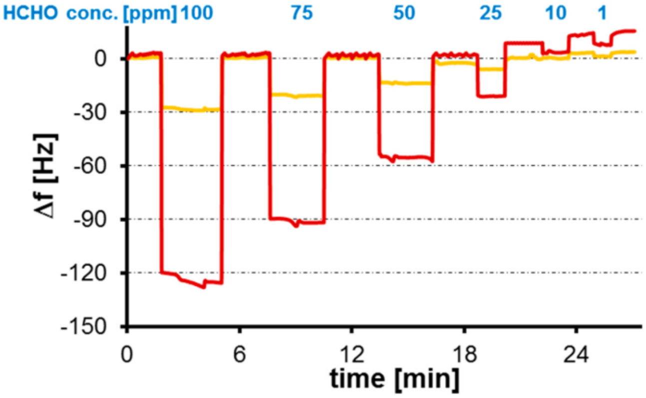

Figure 1-16. Response of a QCM coated with a MIP in the presence of different vapor concentrations of formaldehyde, taken from [108].

In another study, a calix[4]arene modified QCM sensor was reported for the detection of benzene, chloroform, ethyl acetate, hexane, methyl chloride and toluene in aqueous media. The authors used modeling with Langmuir and Freundlich isotherms to show that this sensor had higher affinity towards toluene, with a detection limit of as low as 5 ppm [109].

MOF thin films have also been applied for the detection of VOCs. For example, Huang *et al.* developed a QCM sensor coated with a MIL-101(Cr) ($C_{24}O_{15}FCr_3.O$) thin film for the effective adsorption of methanol, n-hexane, butanone, toluene, n-butylamine and dichloromethane. In this study, it was found that the MIL-101 has high affinity for VOCs containing heteroatoms or aromatic rings and that the metal sites are important for the adsorption ability of the MOF [110].

Quang *et al.* designed a graphene-coated QCM sensor which showed good reproducibility and reversibility with fast recovery time for the detection of butanol, acetone, isopropanol and ethanol. The authors found that the sensor had the highest affinity towards ethanol, with a sensitivity of about 4.5 ppm per 1 Hz [111].

1.6.3.2 Detection of gases

Several QCM based sensors have been developed for the detection of hazardous gases. Qi *et al.* modified a GO coated-QCM with nanoparticles of SnO_2 and silver to develop a sensor for the detection of low concentration of NO_2. The authors reported the detection of 2.05 mg/m^3 of NO_2, indicating that surface modifications of GO can lead to an enhanced sensitivity[112].

A highly selective and reproducible QCM sensor based on metal oxide ZnO nanorods has been reported for the detection of NH_3. The ZnO nanorods were vertically aligned and grown directly on the QCM with a diameter of 100 nm and height of 3 µm, while the sensor was proved to be selective towards NH_3 over CO, NO_2 and CO_2 [113], as shown in Figure 1-17, with a sensitivity of about 9 Hz per 50 ppm.

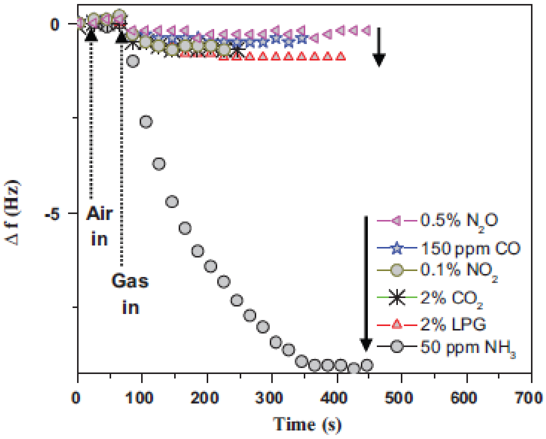

Figure 1-17. Comparison of the frequency change for the ZnO coated QCM sensor when exposed to different gases, taken from [113]

Monitoring the concentration of CO_2 is also very important for air quality and early fire detection and QCM sensors targeting CO_2 have been developed. For example, Muraoka *et al.* fabricated a CO_2 sensor by coating acrylonitrite-styrene copolymer membrane onto a QCM, which was selective to CO_2 over O_2 and Ar [114]. In a later study, Devkota *et al.* coated a ZIF-8 thin film, which is a MOF composed of zinc ions and 2-methylimidazole organic linkers, on the surface of a QCM by LbL assembly and were able to reversibly detect CO_2. It was found that the response was linearly proportional to the concentration of CO_2, with a maximum frequency shift of approximately 217 Hz in 100 vol-% CO_2 [115].

1.6.3.3 Detection of heavy metals

Excessive concentration of heavy metal ions such as Cr^{2+}, Cu^{2+}, Hg^{2+} or Pb^{2+} in aquatic ecosystems can be extremely harmful to human health and the environment due to their accumulation overtime in living organisms. Hence, QCM sensors have been developed for their rapid detection. A few examples are reviewed below.

Cao *et al.* reported on a N-vinylimidazole and 2-mercaptobenzothiazole copolymer film with was coated on a QCM electrode by spin-coating. The copolymer contains many nitrogen and sulfur sites which act as electron donors and can form complexes with heavy metal ions. This QCM sensor was able to detect many ions in aqueous solutions such as Co^{2+}, Cd^{2+}, Ni^{2+}, Zn^{2+} and Pb^{2+}, however it exhibited higher selectivity and stability towards Cu^{2+}. The detection limit was reported as low as 10 ppm, which resulted in a frequency shift of 3 Hz [116].

In another study, Sartore *et al.* reported on a 2,2-Bis(acrylamido)acetic acid polymer coated QCM sensor, where the monomers were polymerized *in-situ* on a QCM modified with a cystamine SAM. In this way, the film was chemically attached to the surface of the QCM, thus increasing the reliability of the sensor. The authors evaluated the performance of the QCM sensor by monitoring the frequency changes induced by the presence of Cu^{2+}, Pb^{2+}, Cr^{3+} and Cd^{2+} in aqueous media [117]. They also showed that the film could be regenerated after it was eluted with HCl solution, as showed in Figure 1-18, where a gradual frequency decrease was observed due to adsorption of Pb^{2+} in the polymer film and then a steep frequency increase due to desorption of Pb^{2+} from the film as a result of the elution with HCl solution [117].

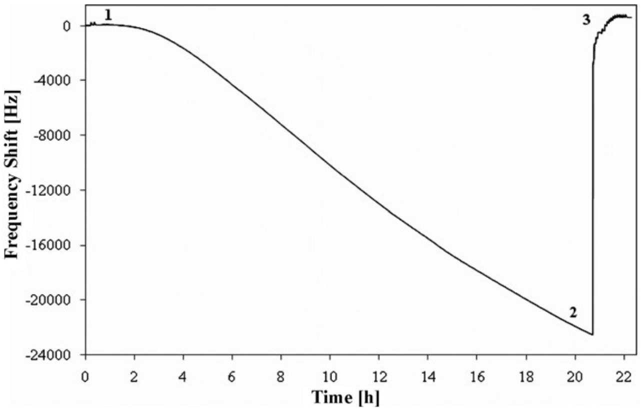

Figure 1-18. Response of the coated QCM over time (1) QCM in equilibrium with natural water flow (0.4 ml/min); (2) Frequency decreases due to flowing Pb^{2+} solution 0.363 mg/L for 20 h; (3) Regeneration by 100 µl HCl solution 0.1 M, taken from [117].

A QCM sensor coated with a thiol functionalized SBA-15 mesoporous silica for the selective detection of Hg^{2+} in water has also been reported. The sensor showed a linear relationship between the concentration of Hg^{2+} and the frequency shift, while the frequency response was found to be about 175 Hz per 1 ppm and the response time as short as 1 minute [118].

1.6.3.4 Detection of anions

Although QCM sensors have not been commonly applied for anion sensing, a few examples of this have been reported. Eun *et al.* have reported on the development of a QCM sensor for the detection of sulfate anions. The sensor was based on barium sulfate crystals, which were grown on a SAM of phosphorylated 11-mercapto-1-undecanol. The response of the modified QCM increased with increasing sulfate ion concentrations in the sample solutions ranging from 6.8×10^{-5} to 4.5×10^{-3} mol L^{-1} due to the adsorption of the ions in the solution/solid interface. The authors found that the sensor was selective to SO_4^{2-} over other anions such as NO_3^-, I^-, Br^- and SCN^- [119].

In a later study, Erbahar *et al.* coated a QCM with a cobalt corrinoid complex via spray coating on a 1-dodecanthiol SAM and were able to selectively detect cyanide anions. The experiments were conducted with aqueous NaCN samples in increasing concentration between the range 4-80 μM. The detection limit was reported as low as 1 μM while the sensitivity to other anions like chloride was at least one order of magnitude lower [120].

1.6.3.5 Detection of biomolecules

A QCM sensor coated with a MIP has been reported for the determination of albumin concentration in human serum, in which albumin was imprinted in a 3-dimethylaminopropyl methacrylamideacrylate film. The developed sensor had a linear response in a range from 60 to 150 ppm of albumin, while the values obtained by MIP-

QCM and clinical assay were 4.80 g/dL and 4.60 g/dL, respectively, which showed good correlation [121].

Another MIP-coated QCM sensor has been reported for the real-time detection of insulin in aqueous solutions and artificial plasma. Insulin was imprinted in a poly(hydroxyethyl methacrylate)-N-methacryloyl-(L)-histidine methyl ester based film, which was synthesized by UV polymerization and characterized with ellipsometry, FT-IR and AFM. The detection limit was found to be as low as 0.00158 ng/mL, while the results were well fitted with the Langmuir adsorption isotherm [122].

Luo *et al.* reported on a QCM biosensor that was designed to detect the recombinant human interferon-β protein. The surface of the QCM was coated with an ethane-dithiol SAM, upon which an antisense peptide AS-1 was immobilized, which possessed a sequence corresponding to the N-terminal fragment of the interferon-β protein. The coated QCM was mounted in a flow-through system and 100 μL of solutions containing the protein in various concentrations were injected into the fluid system, while the sensor was regenerated by glycine-HCl injections [123].

1.7 Viability of a real-time QCM sensor

As it was discussed in the previous sections, QCM sensors have been applied in many ways for the detection of various analytes. However, the sensors were applied in a controlled laboratory environment in all the cases found in literature, due to nature of the QCM, which is very sensitive in changes in temperature and to external forces, such as minor changes in liquid flow or vibrations, limiting its use in an open environment and especially in the field. Thus, the candidate QCM sensors proposed in this work are not meant to completely replace the existing detection methods, but to be applied as an assisting means for faster detection. A possible way is the following. A QCM sensor can be used in a laboratory on site for the fast monitoring of samples collected on site. If TcO_4^- is detected, then the corresponding samples can be sent out of site for proper determination with the traditional methods, hence reducing the number of samples to be tested. Thus, the use of QCM as preliminary monitoring technique would be advantageous, as it is a small device that does not take up a lot of bench space and the development a QCM sensor would not cost more than a few hundred dollars.

1.8 ReO_4^- as a surrogate for TcO_4^-

The radiotoxicity of technetium means that direct study of TcO_4^- has been limited and is generally approached though the study of its chemical analogue, Rhenium. [124]. Tc and Re exhibit [Kr]$4d^5 5s^2$ and [Xe]$4f^{14} 5d^5 6s^2$ electronic configurations, respectively, with the seven outer electrons making possible valence states between 0 and +7 for both elements. As with Tc, the solubility of Re is also dependent on its oxidation state and the chemical environment, with most stable states being +4 and +7. The E_h-pH diagrams for both Tc and Re are presented in *Figure 1-19*, and show that, under oxidizing conditions Re(VII) is stable, with the dominant species being ReO_4^-, the isostructural form of the Tc(VII) species [125].

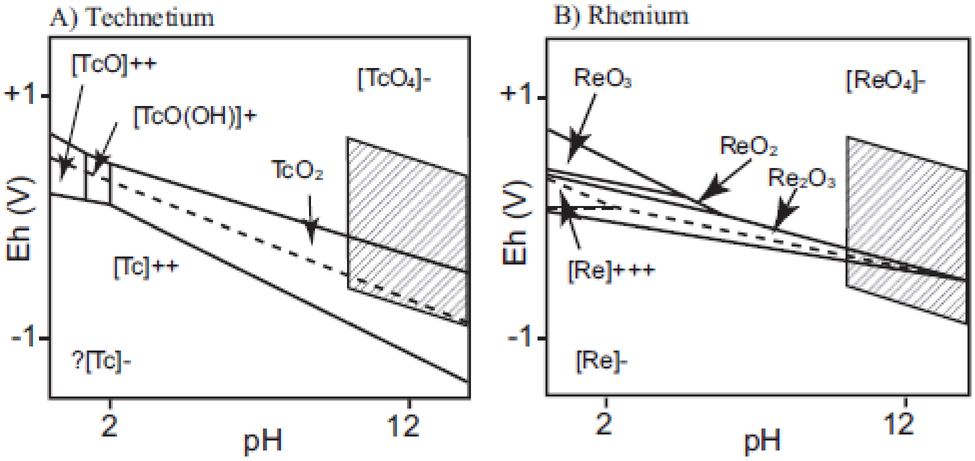

Figure 1-19. E_h-pH diagrams for A) Tc and B) Re. It should be noted that the stability region of TcO_2 is much larger than that of ReO_2, while there is no stability field for Tc(III). However, the stability fields for TcO_4^- and ReO_4^- are almost identical. The shaded areas represent the conditions in waste environment [125].

Perrhenate ion, having similar size, geometry and chemical properties with pertechnetate, has been used as its chemical surrogate [126], [127]. A comparison between the properties of the two anions can be seen in Table 1.3. Both have tetrahedral geometry and similar M-O bond lengths (1.71 A for Tc-O and 1.72-1.73 for Re-O). Also, their charge/volume ratio is identical and they both have low hydration energy (-330 kJ mol^{-1} for ReO_4^- and -251 kJ mmol^{-1} for TcO_4^-). Consequently, it should be expected that the binding behavior with receptors containing positively charged binding sites will be similar for ReO_4^- and TcO_4^- [126].

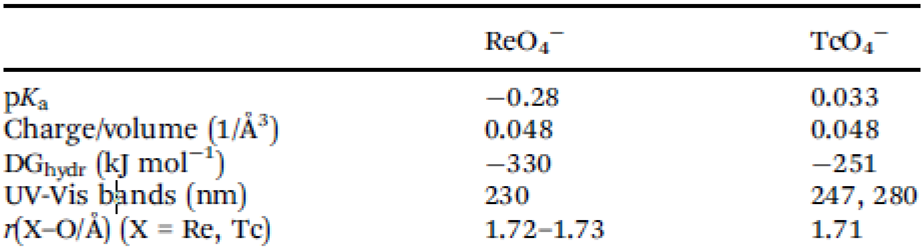

	ReO_4^-	TcO_4^-
pK_a	−0.28	0.033
Charge/volume (1/Å^3)	0.048	0.048
DG_{hydr} (kJ mol^{-1})	−330	−251
UV-Vis bands (nm)	230	247, 280
r(X–O/Å) (X = Re, Tc)	1.72–1.73	1.71

Table 1.3.Characteristic properties of ReO_4^- and TcO_4^- [126].

The perrhenate ion has extensively been used as a surrogate for the pertechnetate ion or studies alongside it in detection or separation experiments that have showed similar selectivity trends of pertechnetate and perrhenate over other anions [80], [124], [126]–[131]. For example, the removal of ReO_4^- and TcO_4^- from aqueous solution using a polyethylenimine-epichlorohydrin resin with similar sorption coefficients in a wide range of pH and in the presence of background electrolyte has been reported [127]. Moreover, the extraction of both anions with azacryptands, where 1:1 complexes were formed, with a maximum extractability of 82% for TcO_4^- and 76% for ReO_4^- has also been reported

[128]. Therefore, for the reasons explained above, the experiments that will be presented in the next chapters, will be targeting the detection of ReO_4^-.

1.9 Summary

In summary, nuclear reprocessing sites such as Sellafield Ltd have a statutory requirement to monitor the radionuclide concentration in the groundwater on their site. Technetium-99 is a contaminant of significant importance, since it forms the extremely water mobile TcO_4^-. Its lack of natural occurrence means that early detection of Tc is crucial because it can help identify leaks of radioactive contaminants into the environment. However, the current methods of determination of Tc in environmental samples, both radiometric and mass spectroscopic, are time consuming and require expensive equipment. In addition, because of its low concentration in environmental samples, Tc must be first isolated form other matrix components that could interfere in the measurement, such as other β-emitters or isobaric nuclei like Ru.

The purpose of this work is to develop a novel, real-time sensor for Tc based on a Quartz Crystal Microbalance, which can detect small changes of mass on its surface. QCM sensors can be coated with a range of materials selective to specific analytes and detect them in many different environments and in very low concentrations. This suggests that a QCM sensor could decrease the number of steps of Tc determination in environmental samples. Thus, in the following chapters, the development of a QCM sensor modified with Tc-selective materials will be presented. More specifically, the synthesis of TREN-derivative ligand is described in Chapter 3, work with TEVA resin and the synthesis of a ligand based on its active compound, Aliquat-336, is presented in Chapter 4 and the synthesis of Ag-4,4'-bipyridine MOF and its thin film is described in Chapter 5. These materials were coated on the QCM surface and their adsorptive behaviour and selectivity was evaluated by exposing the modified QCM to ReO_4^-, the non-radioactive chemical surrogate of TcO_4^-, and other common interferences present in groundwater, while the adsorption data was modelled with adsorption isotherms, such as Langmuir, Freundlich and Sips in Chapter 6. Furthermore, part of the work described in Chapters 5 and 6 has been reported in the Journal of Electrochemical Society [132]. In the next chapter, the materials, methods and equipment used in the following experiments will be presented.

CHAPTER 2

2 Materials and methods

2.1 QCM crystals and equipment

The QCM crystals used in this study were supplied by Quartz Pro AB (Jarfalla, Sweden). The crystals had a resonant frequency of 5 MHz, 14 mm diameter and were AT cut. A titanium adhesion layer is used to bind the gold to the quartz. A diagram of both faces of the crystal is shown in Figure 2-1. The front big gold electrode wraps around the quartz and extends to an arch on the back side of the crystal, though which the crystal is connected to the QCM holder.

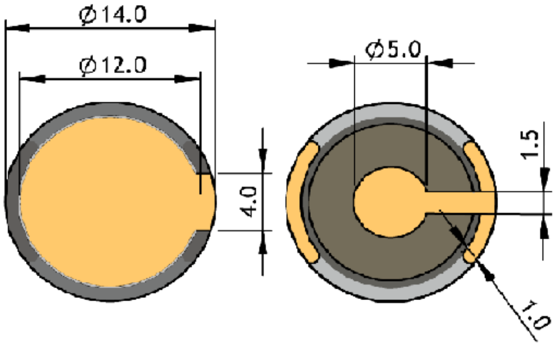

Figure 2-1. Diagram of the front electrode (left-hand side) and the back electrode (right-hand side) of the gold plated QCM crystals used in this work.

The QSH-dip sensor holder was provided by Microvacuum Ltd (Budapest, Hungary) and is shown in Figure 2-2. Through this holder, the modified front electrode of the QCM is only exposed to the solution containing the analytes. The holder is then connected to a Maxtek RQCM system, provided by Testbourne Ltd (Basingstoke, England), connected to a Personal computer running Maxtek RQCM 2.0 software, though which the chronomassograms were recorded.

Figure 2-2. The Microvaccum Ltd QSH-dip sensor holder.

2.1.1 QCM calibration

The QCM system must be calibrated in order to determine the mass sensitivity factor. This was done by carrying out concurrent cyclic voltammetry and voltamassogram experiments using a 3-electrode cell, where a calomel electrode served as the reference electrode, a platinum wire served as the counter electrode and the front face of the QCM served as the working electrode. The electrolyte was a 10 mmol L^{-1} Cu_2SO_4 in a 0.5 mol L^{-1} H_2SO_4 aqueous solution. The cell configuration is shown in Figure 2-3. This experiment allowed to corelate the change in frequency with the change in mass on the QCM surface. This was achieved by reducing and depositing metallic Cu on the QCM and then removing it by oxidizing it back to Cu^{2+}, while at the same time monitoring the change in frequency. In this way, the mass of Cu deposited and then removed from the QCM was calculated electrochemically by the current passed through the system and was then related to the change in frequency.

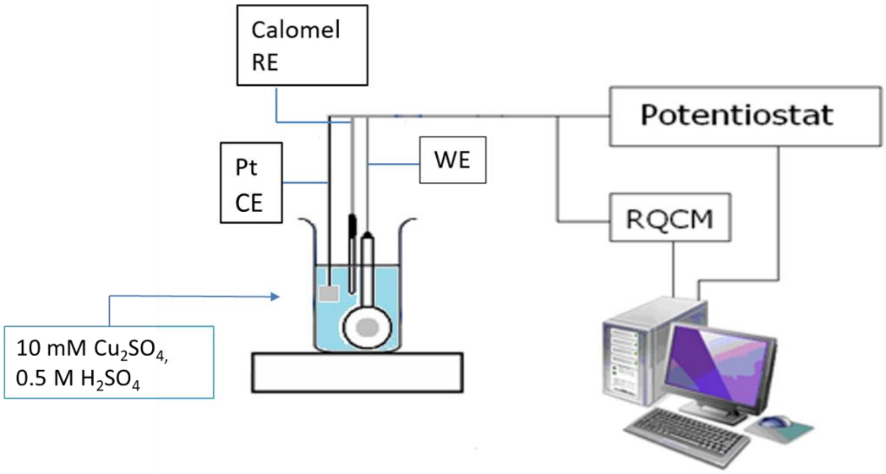

Figure 2-3. QCM calibration through a three electrode cyclic voltammetry configuration. QCM is the working electrode, a calomel electrode is the reference electrode and a platinum wire is the counter electrode, while the cell is filled with 10 mmol L^{-1} Cu_2SO_4 in a 0.5 mol L^{-1} H_2SO_4 aqueous solution.

The voltage window was scanned from 0.5 V down to -0.5 V and then back up to 0.5 V at a scan rate of 50 mV/s and a step size of 2 mV. The cyclic voltammogram produced is presented alongside the change in frequency of the QCM in Figure 2-4. The negative-going portion of the scan shows a reduction peak at -0.4 V with a simultaneous frequency drop, indicating that Cu is being deposited on the QCM, through the half-reaction:

$$Cu^{2+} + 2e^{-} \rightarrow Cu$$

the positive-going portion of the scan shows a sharp oxidation peak at about 0.15 V with a simultaneous frequency increase, indicating Cu is removed from the QCM back to the solution through the half-reaction:

$$Cu \rightarrow Cu^{2+} + 2e^{-}$$

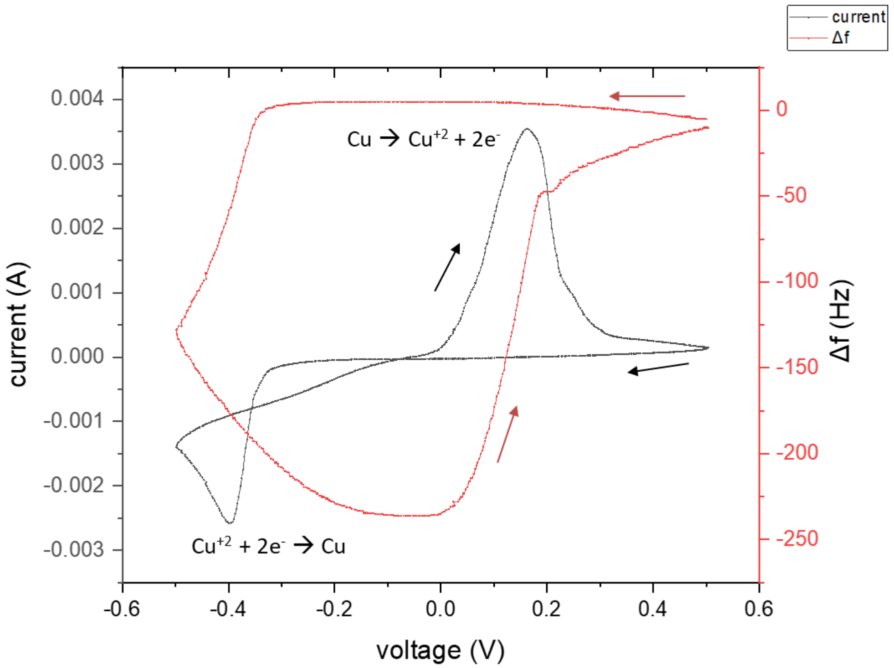

Figure 2-4. Cyclic voltammogram (shown in black line) with the change in frequency of the QCM (shown in red line). The arrows indicate the direction of the cycle. Starting from 0.5 V and scanning down to -0.5 V, there is a reduction peak at -0.4 V and a simultaneous frequency drop, indicating Cu is being deposited on the QCM. Then scanning back to 0.5 V, there is a sharp oxidation peak at about 0.15 V and a simultaneous frequency increase, indicating mass loss.

The current and the change in frequency can be plotted against time, as shown in Figure 2-5. In this way, the alignment of the current and the frequency is even more obvious. The yellow area in the diagram contains the oxidation peak and the frequency increase at the same time because of the removal of metallic Cu from the QCM. By integrating the grey area below the peak, the total charge passed though the electrode is obtained and thus the total mass of the metallic Cu that was oxidized can be obtain through Faraday's law of electrolysis [133]:

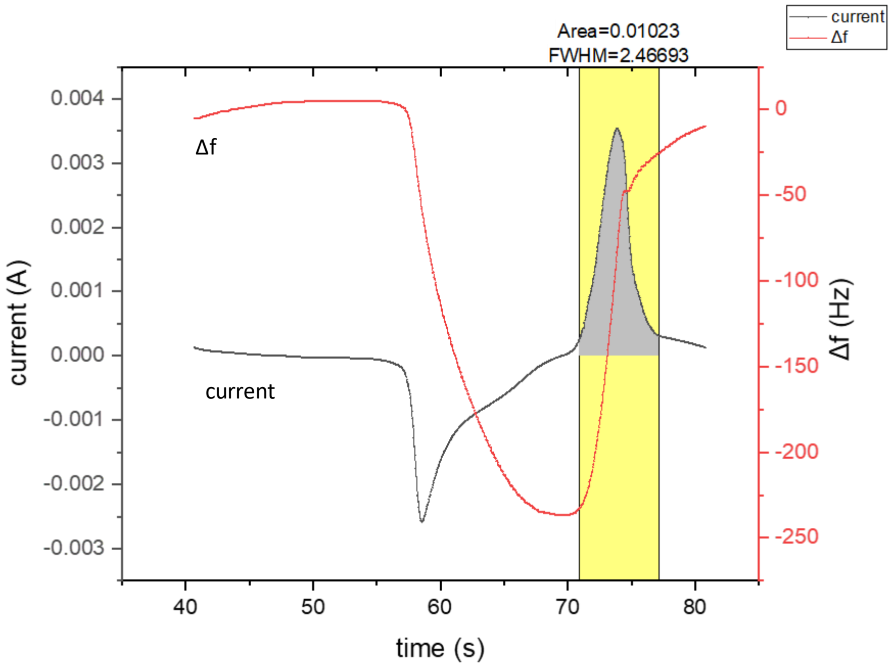

Figure 2-5. The current of the cyclic voltammetry (black line) and the change in frequency (red line) plotted against time. The yellow area marks the oxidation peak through which the total charge can be obtained.

$$\Delta m = \frac{QM}{Fn} = \frac{0.01023\ C * 63.546 \frac{g}{mol}}{96485.33289 \frac{C}{mol} * 2} = 3.369\ \mu\text{g}$$

where *Q* is the total charge that passed through the electrode, *M* is the molar mass of Cu, *F* is the Faraday constant and *n* is the number of electrons in the semi-reaction. Hence, the mass sensitivity factor can now be obtained through Sauerbrey's equation:

$$C_f = -\frac{\Delta \text{f}}{\Delta \text{m}} * A_e = \frac{203\ \text{Hz}}{3.396\ \mu g} * 0.950\ cm^2 = 56.81 \frac{Hz\ cm^2}{\mu g}$$

where Δf is the frequency change during the oxidation, marked by the yellow area in Figure 2-5, Δm is the mass obtained by Faraday's law of electrolysis and A_e is the electroactive area of the QCM, which is the exposed part of the front electrode of the QCM, defined by the surface area of the O-ring. The value obtained through the calibration experiments is in very good agreement with that given by the manufacturer, which is 56.6 Hz cm^2 μg^{-1}. This indicates that our QCM system operates according to it designed specifications and is ready to progress with the experiments, with no need of further calibration. All analysis presented in the later chapters was conducted with the experimental mass sensitivity factor C_f = 56.81 Hz cm^2 μg^{-1}.

2.2 Reagents

All the chemicals used in this work were of analytical grade or higher and purchased by different suppliers. All the reagents used in the organic synthesis processes described in sections 3.1.1 and 4.2.1 were supplied by TCI Chemicals (Tokyo, Japan). The chemicals used in the preparation of the hydrogel described in section 4.1.1 were supplied by Fisher Scientific (Hampton, New Hampshire, USA). The reagents used for the preparation of the MOF bulk crystals and thin film described in sections 5.1 and 5.3.1 were purchased by Sigma-Aldrich (St Louis, Missouri, USA). The chemicals used as analytes in the adsorption experiments described through sections 5.3.2 - 5.3.5 were supplied by Alfa Aesar (Haverhill, Massachusetts, USA). All solutions were freshly prepared, aqueous solutions were prepared in deionised water produced in a direct-Q UV water deionization system (Millipore, MA, USA) with a resistivity of 18MΩ cm^{-1}. Nitrogen was generated in house from a nitrogen extraction plant (L60-10, AMSystems, Livingston, UK).

2.3 Characterisation techniques

2.3.1 X-ray diffraction (XRD)

In X-Ray Diffraction, samples are irradiated with X-rays which are then diffracted/reflected back by planes of atoms within the crystalline lattice of the sample. The reflected/diffracted X-rays are then detected. The resultant diffraction pattern provides information relating to the arrangements of the atoms in the unit cell, including the distance between planes of atoms within the crystalline lattice. This is referred to as the d-spacing (d), and can be calculated from fixed and measured experimental parameters by employing Bragg's law [134]

$$n\lambda = 2dsin\theta$$

Where λ is the wavelength of the irradiating X-ray (a constant value of 0.1542 nm for the experiments discussed here), ϴ is the scattering angle in degrees or angle at which a diffracted reflection of X-rays is observed from the sample (ϴ being measured relative to the direction of the incident X-ray beam) and n is an integer representing the order of the diffraction peak.

The X-ray diffraction patterns presented in section 5.3.1 were recorded using an Agilent SuperNova diffractometer (Agilent Technologies, Santa Clara, California, USA) at an irradiation wavelength of 0.154 nm and at room temperature.

2.3.2 SEM/EDX

Scanning Electron Microscopy (SEM) is used to image the topology of a sample on micrometer scale by scanning the surface with a focused electron beam. In the most commonly used mode of operation, secondary electrons emitted by atoms excited by the primary electron beam are detected using a secondary electron detector [135].

The SEM technique usually offers the possibility of mapping the elemental composition of the studied surface using energy dispersive X-ray spectroscopy (EDX). Linked to SEM, this is a technique that identifies and quantifies elements present in the sample simultaneously with the acquisition of a SEM image of the sample surface. Its operation is based on the fundamental principle that each element has a unique electronic structure, which allows the emission of characteristic X-rays. To stimulate this emission, a beam of electrons is focused onto the sample exciting an electron in an inner shell, creating an electron hole. This hole is then filled with an electron from an outer shell, emitting an X-ray to cover the energy difference. EDX has a typical analysis depth of 1-3 μm [135].

Scanning Electron Microscopy of the samples, coupled with Energy Dispersive X-ray spectroscopy (EDX) presented also in section 5.3.1 was carried out using a JEOL 6010-LV (JEOL (UK) Ltd., Herts, UK) scanning electron microscope (SEM). The examinations were performed at 20 keV using compositional backscatter imaging (BEC) in low vacuum mode, with an instrument resolution ∼5 nm.

2.3.3 Nuclear Magnetic Resonance (NMR)

Nuclear Magnetic Resonnance is most commonly used to charasterise the chemical structure of organic molecules. Its operation is based on the interaction of the nuclei of certain isotopes with a static magnetic field. This magnetic field makes the possible spin states of the nucleus differ in energy and can create observable transitions between the spin states. The utility of NMR relies on the fact that chemically distinct nuclei differ in resonance frequency in the same magnetic field. This phenomenon is known as the chemical shift. In addition, the resonance frequencies are affected by neighboring NMR active nuclei, depending on the bonding electrons that connect the nuclei. This is known as spin-spin coupling, which allows the identification of connections between atoms on a molecule, through the bonds that connect them. Combined with quantitative information acquired by integrating the peak intensities, the molecular structure of the sample can be identified. Most common NMR active nuclei in organic chemistry are ^{1}H and ^{13}C. In solution state NMR, which is the most common mode, the sample is dissolve is a deuterated organic solvent [136].

The ^{1}H and ^{13}C NMR experiments presented in sections 3.1.1 and 4.2.1 were carried out using a Bruker AVANCE III 400 (Bruker Corporation, Coventry, UK).

2.3.4 Infrared spectroscopy (IR)

Infrared spectroscopy is used to identify functional groups of molecules through the interaction of infrared radiation with a sample, by measuring reflection, emission and absorption. IR spectroscopy works on the principle that molecules absorb specific frequencies that are characteristic of their structure. At temperatures above absolute zero, all the atoms in molecules are in continuous vibration with respect to each other. The IR spectra indicates what types of vibrational modes the molecule responds with after it absorbs that light, while the size and shape of every peak in the spectrum corresponds to a specific motion of a specific chemical bond.

IR analysis presented in sections 3.1.1 and 4.2.1 was carried out using a Cary 630 FTIR Spectrometer (Agilent Technologies Ltd, Santa Clara, California, USA)

2.3.5 Mass spectrometry (MS)

The basic principle of MS is to generate ions from either inorganic or organic compounds by any suitable method, to separate these ions by their mass-to-charge ratio (m/z) and to detect them qualitatively and quantitatively by their respective m/z, abundance and the time required to travel the length of the flight tube. In the Matrix Assisted Laser Desorption Ionization (MALDI) methodology used in this work, the sample is ionized in an automated mode with a laser beam.

MS analysis presented in sections 3.1.1 and 4.2.1 was caried out with a Shimadzu Axima iDplus Performance MALDI-TOF mass spectrometer (Shimadzu Scientific Instruments, Kyoto, Japan).

CHAPTER 3

3 Preparation of tris(2-aminoethyl)amine (TREN) functionalised QCM

Ligands based on tri(2-aminoethyl)amine (TREN) that can effectively bind and extract from solution the pertechnetate and perrhenate anions have been reported in the literature. The tripodal tris(amido benzo-15-crown-5) ligand, shown in Figure 3-1a, contains a tripodal tetrahedral amide hydrogen bond donor anion recognition site in combination with crown ether cation binding moieties. The binding of alkali metal cations by the crown ethers allows for a favourable cation-anion electrostatic interaction to augment the neutral amide N-H hydrogen bond donating to the tetrahedral anion. The authors demonstrated binding and extraction of TcO_4^- with Na^+ in the presence of excess chloride under conditions which mimic aqueous nuclear waste streams. [70]. More recently, the azacryptand ligand LH_6^{6+} shown in Figure 3-1b, can provide a powerful tool for the selective capture of TcO_4^-. In this ligand, the binding occurs in acidic environment (pH = 2) when the 6 amine groups are protonated, leading to an overall positive charge of +6. So, pertechnetate is selectively bound by electrostatically augmented hydrogen bonds in comparison to other potentially interfering anions such as nitrate and chloride. [137].

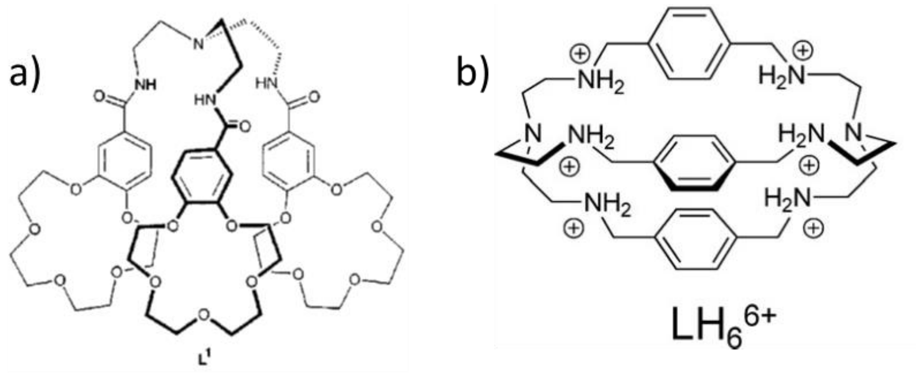

Figure 3-1. a) the tripodal tris(amido benzo-15-crown-5) ligand L1 [70] *and b) the azacryptand ligand* LH_6^{6+} [137].

Both aforementioned ligands have been synthesized from tris(2-aminoethyl)amine or TREN, which constitutes the active group with which the perrhenate and pertechnetate anions interact. In a similar concept, the synthesis of a novel TREN ligand derivative, shown in Figure 3-2, that can be attached on the gold surface of the QCM, in the form of a self-assembled monolayer (SAM), will be presented in this chapter. The attachment of the ligand onto the QCM is designed to occur by reaction of the disulfide with the Au surface, while the detection of pertechnetate and perrhenate anions will occur by binding of the anions at the TREN functional group, which will be exposed in the solution.

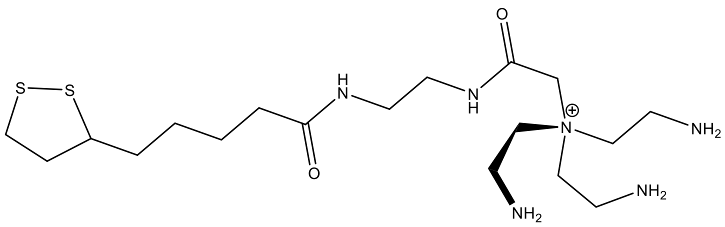

Figure 3-2. Structure of the novel TREN ligand

With this structure, the three amines can be protonated in acidic environment, thus creating a higher positive charge in the active group that could lead to stronger electrostatic bonds with the pertechnetate anion. The synthesis of the ligand will be presented in detail in the next section.

3.1 Synthesis and characterisation of the ligand

For the synthesis of the novel TREN ligand derivative, a synthetic route consisting of 6 steps was designed, as shown in Figure 3-3. The basic commercially available materials of this synthetic route are TREN and thioctic acid. These were connected though the formation of amides. To achieve the necessary regioselectivity in *Steps 2 and 5*, the primary amines of TREN must be masked by use of the Boc protecting group. In this way, only the tertiary nitrogen of TREN is free to react in *Step 2* to yield the quaternary ammonium. The Boc protection process of TREN, which yielded compound 1, was straightforward with relatively high yield (84%) and has been reported before [138].

The alkylation process, which yielded compound 2, was a quite slow reaction and an accurate calculation of the yield is impossible since the counter anion of the quaternary amine is not known, as it will be explained in the experimental section, however an estimation would fall between 40% - 55% yield. Then, the hydrolysis of compound 2, which yielded compound 3, was also a fast reaction with a relatively good yield (76 %). While similarly structured quaternary amines to compounds 2 and 3 have been reported [139], [140], these are entirely novel and were fully characterised with ^{1}H NMR, ^{13}C NMR, IR and MS.

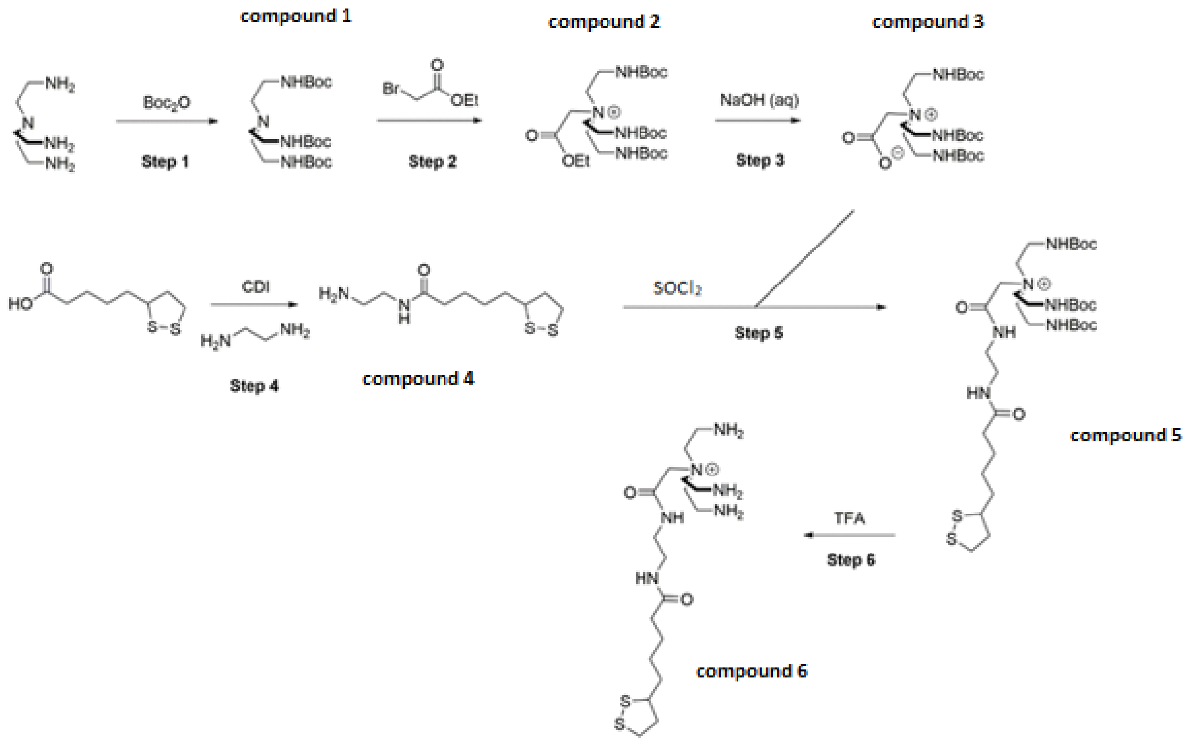

Figure 3-3. Synthetic route of the TREN based ligand.

Thiotic acid had to be first reacted with ethylenediamine, and then the resulting free amine (compound 4) reacted with compound 3 to form the tri-Boc-protected ligand (compound 5). This reaction proved to be challenging to achieve and extremely time consuming. Carboxylic acids, such the one produced in step 3, require activation in order to react with an amine. Table 3.1 shows the activating agents and the solvents that were used for this reaction, alongside with the yields of compound 5.

Activating agents	Solvents	Yield
Carbonyldiimidazole (**CDI**)	anhydrous CH_2Cl_2	0%
N,N′-Dicyclohexylcarbodiimide/N-Hydroxysuccinimide (**DCC/NHS**)	anhydrous CH_2Cl_2	0%
1-Ethyl-3-(3-dimethylaminopropyl)carbodiimide/ Hydroxybenzotriazole (**EDC/HOBt**)	anhydrous CH_2Cl_2	0%
$SOCl_2$	anhydrous CH_2Cl_2	3%
$SOCl_2$	anhydrous THF	15%

Table 3.1. Activating reagents and solvents used in the reaction of step 5 of the synthetic route, alongside with their yields.

Carbonyldiimidazole, which is a most common activating agent for this type of reaction, as exemplified by its use in *Step 4,* did not yield any product at all. Other coupling reagents, such as DCC in coupling with NHS and EDC in coupling with HOBt also failed to yield the reaction. Finally, $SOCl_2$, which when used carefully has been shown to activate similar molecules which contain acidic sensitive protecting groups [141], was trailed and found to successfully achieve formation of compound 5. However, the yield achieved was quite low (~ 15%). This may be due to low reactivity of the carboxylic acid group of compound 3 due to the formation of intramolecular hydrogen bonds between the O atom and the N-H of the Boc carbamate groups. Nevertheless, it should be noted that this is a novel molecule, which was fully characterized with ^{1}H NMR, ^{13}C NMR, IR and MS.

Finally, removal of the Boc protecting groups was attempted using TFA, which is the typical reagent for this reaction [142]. However, the ^{1}H NMR spectrum of the product was not clear, possibly because of excess TFA distorting the recorded spectral data. Given the low yield of the previous step, there was insufficient material to record a ^{13}C NMR spectrum. However, it was decided to react the material with a QCM surface, and see if a response could be detected upon addition of anions. The exact procedure of each synthetic step is presented in detail below.

3.1.1 Experimental section

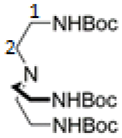

Compound 1

Tris(2-aminoethyl)amine (TREN) (4.88 g, 33,4 mmol) was dissolved in 150 mL of CH_2Cl_2. Di-tert-butyl dicarbonate (Boc_2O) (3 eq, 21.8 g, 100.1 mmol), also dissolved in 150 mL of CH_2Cl_2, was added dropwise into the TREN solution, resulting in the formation of a white precipitate. The reaction was stirred for 2 days and cooled in 0 °C. Then, the solvent was removed and the remaining white sticky solid was dissolved in 50 mL of ethyl acetate (EtOAc). The solution was washed 2 x 100 mL of 0.5 M NaOH (aq) and then the aqueous layer was diluted with brine and the product was extracted with 100 mL of EtOAc. Finally, the EtOAc solution was dried with solid $MgSO_4$ and then the solvent was removed. The crude material was purified with silica gel column chromatography (96/4 CH_2Cl_2/CH_3OH) to yield compound 1 (12.5 g, 84%) as a crumbly white solid. Since this is not a novel compound, the product was sufficiently characterized by ^1H NMR, with data consistent with previous reports [138].

δH (400 MHz; $CDCl_3$) 5.13 (3*H*, s, N*H*), 3.16 (2*H*, q, C^1*H*), 2.53 (2H, t, C^2*H*), 1.46 (27*H*, s, Boc*H*)

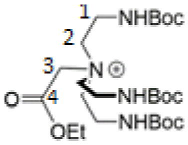

Compound 2

Compound 1 (6.0 g, 13.4 mmol) was dissolved in 40 mL of dry acetonitrile (MeCN) under argon atmosphere and was cooled down to 0 °C in an ice bath. Ethyl bromoacetate (1.5 eq, 3.36 g, 20.1 mmol) was added dropwise in the above solution and the reaction was stirred overnight. Analytical TLC revealed that the reaction had not reached completion, so it was heated up to 80 °C and was stirred overnight again. The next day, quick TLC tests showed that yet again the reaction had not occurred, NaI (2 eq, 4.02 g, 26.8 mmol) was added in order for I^- to replace Br^- as a better leaving group. Finally, the next day TLC tests showed that the reaction had occurred and the solvent was removed. The crude material was purified with silica gel column chromatography (96/4 CH_2Cl_2/CH_3OH) which yielded two fractions, the first one 2.76 g containing a mix of the starting material (compound 1) and ethyl bromoacetate, and the second one 4.14 g containing a mix of the starting material and the product (compound 2). The second fraction was purified one more time by silica gel column chromatography (98/2

CH_2Cl_2/CH_3OH) which finally yielded 2.71 g of pure product, confirmed by ^{1}H NMR, ^{13}C NMR, IR and mass spectroscopy.

The first fraction of the first column containing the mix of compound 1 and ethyl bromoacetate was put to react again in MeCN solvent, under Ar atmosphere, in NaI presence and with an excess of ethyl bromoacetate on 70 ^oC for 2 days. Solvent was removed and the crude material was purified again two times with silica gel chromatography first with 96/4 CH_2Cl_2/CH_3OH and then with 98/2 CH_2Cl_2/CH_3OH, yielding a further 1.44 g of pure compound 2.

*δ*H (400 MHz; $CDCl_3$) 5.75 (2*H*, s, N*H*), 4.69 (2*H*, s, C^3*H*), 4.30 (2*H*, q, EtCH_2), 4.05 (2*H*, t, C^2*H*), 3.73 (2*H*, q, C^1*H*), 1.45 (27H, s, Boc*H*), 1.36 (3H, t, EtCH_3)

*δ*C (100 MHz; $CDCl_3$) 164.05, 80.60, 28.29 (3 Boc C environments), 156.26 (C^4), 62.84 ($EtCH_2$), 59.80 (C^2), 57.60 (C^3), 35.12 (C^1), 14.02 ($EtCH_3$)

ν_{max} / cm^{-1} (neat) 3287 (N-H), 2976, 2935 (C-H), 1748, 1690 (C=O), 1248 (C-N), 1159 (C-O)

m/z (ES) $[M]^+$ 533.3539, $C_{25}H_{49}N_4O_8$ predicted 533.3545

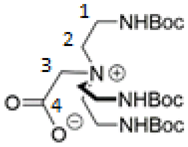

Compound 3

Compound 2 (1.38g, 2.25 mmol) was dissolved in a 1/1 mix of 40 mL THF/CH_3OH. An aqueous solution (5mL) of KOH (2 eq, 0.252 g, 4.502 mmol) was added to the above solution and the reaction was stirred overnight. Then, the solution was concentrated on the rotary evaporator in about 7-10 mL and 50 mL of CH_2Cl_2 were added. The solution was washed 3 times with 50 mL of deionised water, in order to remove the ethanol produced by the hydrolysis of the ester and any inorganic salt that may had been formed. The aqueous layer was collected and washed 2 times with CH_2Cl_2. Finally, all the organic layers of CH_2Cl_2 were collected in one solution which was concentrated and dried to yield compound 3 (0.868 g, 76%) as an ochre crumbly solid, confirmed by ^{1}H NMR, ^{13}C NMR, IR and mass spectroscopy.

*δ*H (400 MHz; $CDCl_3$) 6.10 (3H, s, N*H*), 3.92 (2H, t, C^3*H*), 3.84 (2H, q, C^2*H*), 1.46 (27*H*, s, Boc*H*)

*δ*C (100 MHz; $CDCl_3$) 166.10, 79.95, 28.36 (3 Boc C environments), 156.29 (C^4), 60.56 (C^3), 58.77 (C^2), 34.68 (C^1)

v_{max} / *cm*$^{-1}$ (neat) 3360, 3257 (N-H), 2974, 2933 (C-H), 1701, 1630 (C=O), 1246 (C-N), 1159 (C-O)

m/z (ES) $[M+H]^+$ 505.3236, $C_{23}H_{44}N_4O_8$ predicted 505.3232

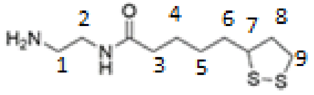

Compound 4

Thioctic acid (81 mg, 0.396 mmol) was dissolved in 5 mL of dry CH_2Cl_2 under Ar atmosphere and the solution was cooled to O °C using an ice bath. Then carbonyldiimidazole (96 mg, 0.594 mmol) was added and the solution was stirred for 5 min, until it was dissolved. Finally the ethylenediamine (0.26 mL, 3.96 mmol) was added dropwise, stirring the solution for 2 hours in room temperature. The product was washed with brine (20 mL) three times. The combined organic phase was dried with anhydrous Na_2SO_4 and then the solvent was removed in the rotary evaporator, yielding the final product as yellow oil. Due to the nature of the product, which would form a very sticky gel, insoluble in solvents of various polarities, such as CH_2Cl_2, THF, MeCN, acetone and hexane, the solvent could not be completely removed, so an accurate yield cannot be calculated for this reaction. The product was only characterized with ^{1}H NMR, with data consistent with previous reports [143].

δH (400 MHz; $CDCl_3$) 5.94 (1H, s), 3.56 (1H, q), 3.30 (2H, q), 3.15 (2H, m), 2.81 (2H, t), 2.45 (1H, m), 2.18 (3H, q), 1.92 (1H, m), 1.68 (4H, m), 1.47 (2H, m)

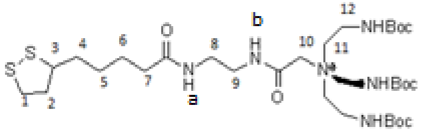

Compound 5

Compound 3 (100mg, 0.198 mmol) was dissolved in 5mL dry THF under Ar inert atmosphere. Then triethhylamine (83 μL, 0.594 mmol) and compound 4 (80 mg, 0.321 mmol) were added and the solution was cooled down to 0 ^{0}C. Then $SOCl_2$ (58 μL, 0.792 mmol) was added and the reaction was stirred overnight at room temperature. The solvent was removed and the crude material was purified with silica gel column chromatography (90/10 DCM/MeOH) yielding compound 5 (20 mg, 15%) as a thin film in the walls of the flask.

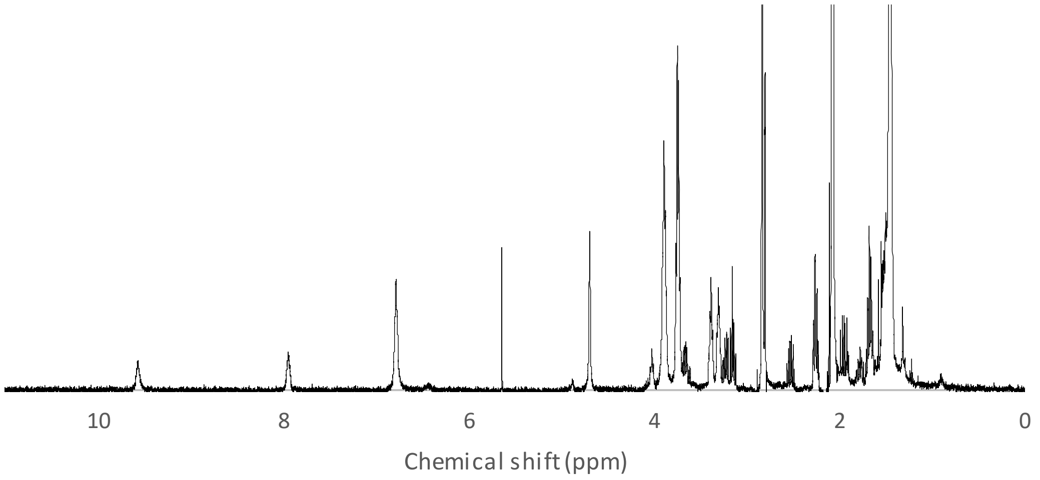

Figure 3-4. ^{1}H NMR spectrum of compound 5, in d6-acetone.

δH (400 MHz; d6-acetone) 9.58 (1H, s, CON^{a}H), 7.95 (1H, s, CON^{b}H), 6.78 (3H, s, NH), 4.69 (2H, s, C^{10}H), 3.89 (6H, t, C^{11}H), 3.73 (6H, q, C^{12}H), 3.65 (1H,m), 3.38 (2H, q, C^{9}H), 3.30 (2H, q, C^{8}H), 3.15 (2H, m), 2.51 (1H, m), 2.26 (2H, t), 1.94 (2H, c), 1.64 (4H, q), 1.50, 1.44 (27H, s, BocH)

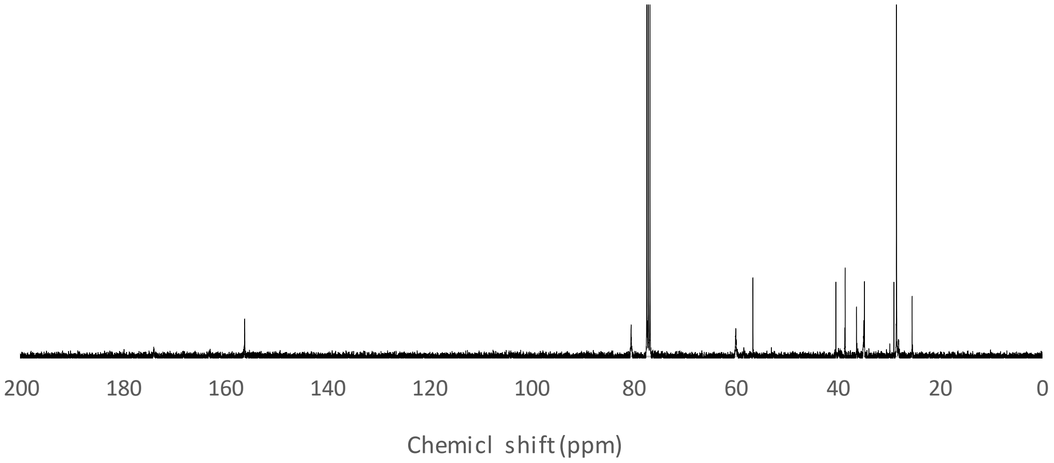

Figure 3-5. ^{13}C NMR spectrum of compound 5, in CDCl$_3$.

δC (100 MHz; CDCl$_3$) 153.80, 80.5, 58.99 , 56.51, 58.77, 40.27 36.20, 34.78, 34.50, 28.41, 25.28

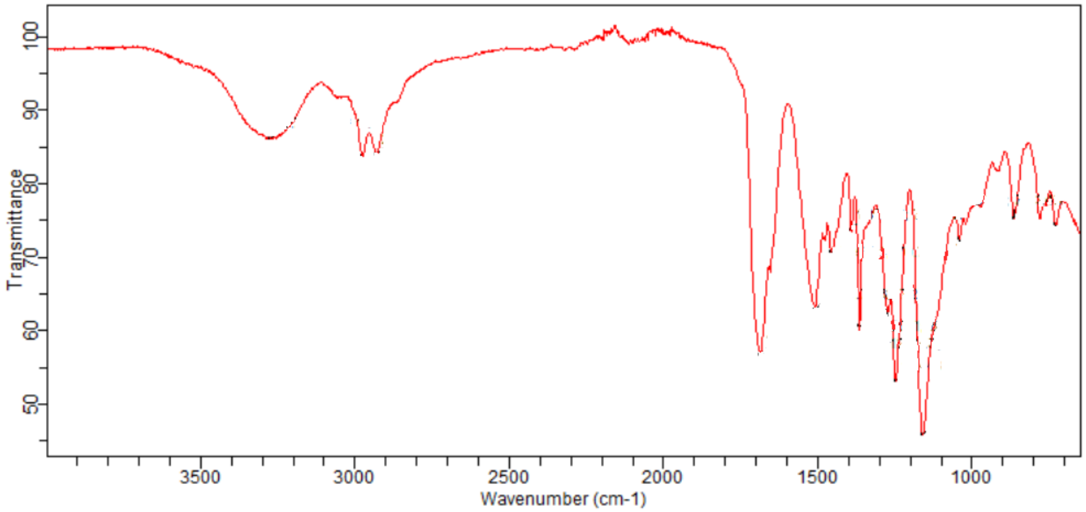

Figure 3-6. IR spectrum of compound 5.

ν_{max} / cm^{-1} (neat) 3272, (N-H), 2976, 2931 (C-H), 1686, 1507 (C=O), 1246, 1366 (C-N), 1159 (C-O)

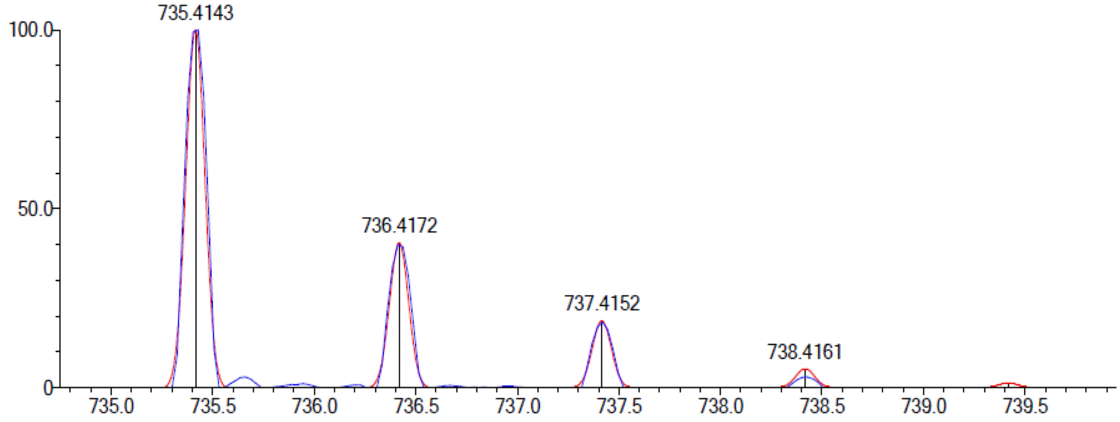

Figure 3-7. Mass spectrometry of compound 5.

m/z (ES) $[M]^+$ 735.4159, $C_{33}H_{63}N_6O_8S_2$ predicted 735.4143

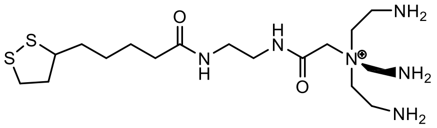

Compound 6 / final product

Compound 5 (20 mg) was dissolved in 2 mL of CH_2Cl_2 and 0.5 mL of trifluoroacetic acid were added in the solution, which was stirred for 2 hours in room temperature. Then the solvent was removed in the rotary evaporator leaving in the flask 15 mg of material in the form of a very thin film. The ^1H NMR was not clear, but this could be due to possible presence of TFA as impurity within the final product, which might form a salt with the free amines.

3.2 Deployment of the ligand on the QCM

With the small amount of material in hand (15 mg), the deployment of the final product on a QCM was tested.

Modification of the QCM crystal was achieved by self-assembled monolayer (SAM) of compound 6 by exploiting the strong affinity of sulfur for gold, as previously state. The QCM crystal was treated with piranha solution, which is a 3:1 mixture of H_2SO_4 and H_2O_2, in order to remove any organic residues and impurities off its gold surface. Then, a 10 mM ethanolic solution of the ligand was prepared and the front side of the QCM was exposed to it for 24 h. This is a standard procedure for the preparation of thiol or disulfide SAMs on gold surfaces [144], [145]. An attempt to measure the mass of the SAM deposited on the QCM failed, because the procedure is very slow and the QCM is very sensitive to minor changes in the environment, leading to a very noisy signal (changes include lights and air-conditioning of the lab going on and off).

After the SAM was prepared, the QCM was immediately tested for the detection of ReO_4^-. The coated QCM crystal was placed in the QCM holder and was left in a beaker with 50 mL of DI water to equilibrate in room temperature for a few minutes. Then aliquots of 0.9 mM of $NaReO_4$ were added in the beaker, but no change in the frequency was observed, as shown in Figure 3-8. This means that either ReO_4^- did not interacted with the ligand, or that any interaction was on too small a scale to be detected by the QCM. To understand some of the possible reasons for that, we have to go back to synthesis of the ligand.

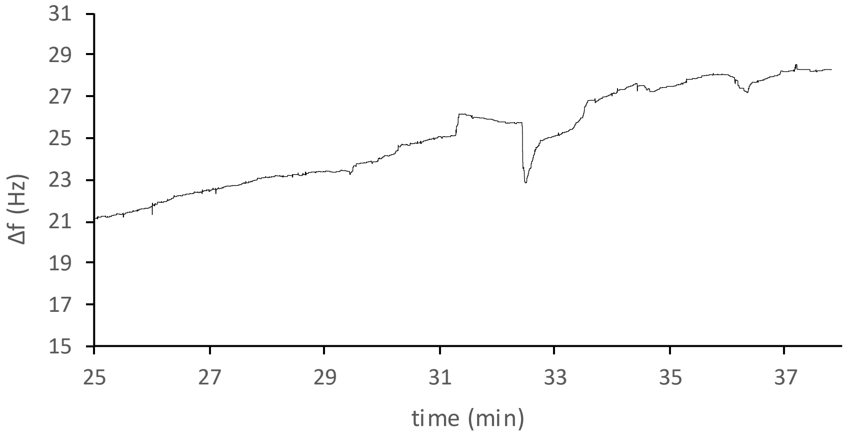

Figure 3-8. Behaviour of the TREN derivative coated QCM in the presence of ReO_4^-. Aliquots of 0.9 mM of $NaReO_4^-$ are being introduced in the solution at minute 31 and every 1 minute afterwards, but only an instant perturbations of ± 4 Hz due to the stirring are observed.

In the last step of the synthetic route, the fully characterised Boc-protected ligand was treated with excess of TFA. So, a possible explanation could be that the free amines were protonated in the acidic environment and trifluoroacetate anions were present as counter anions, constraining the electrostatic interaction of the ligand with other anions.

3.3 Conclusion

By multi-step chemical synthesis, a novel tri-Boc protected ligand was prepared and characterized by NMR, IR and mass spectrometry. However, the synthesis was difficult, and in the limited time available, only a small amount of material was prepared. The subsequent Boc deprotection was attempted using well-established reaction conditions but ^{1}H NMR spectroscopic data did not conclusively show that deprotection was successful without degradation of the rest of the molecular structure. However, the amount was enough to produce a few SAMs and test its anion exchange capacity. Hence, a SAM preparation was attempted, but no detection of ReO_4^- was observed. This could be due to issues with the quality of the final product, very small frequency deviations resulting from only a small number of anions being accepted within the TREN derivative structure caused by the presence of only a single monolayer onto the crystal, or a decreased affinity for the target anion as a result of the modifications made to the base TREN ligand.

For the reasons explained above, it is safe to assume that effective detection of ReO_4^-, and consequently of TcO_4^-, cannot be achieved using a SAM of the TREN ligand derivative. Thus, it was decided to abandon this line of enquiry and refocus the project to make use of other segregating materials such as Teva resin and its active group, as presented in the next chapter.

CHAPTER 4

4 Preparation of TEVA resin and Aliquat-336 functionalized QCM

TEVA resin is probably one of the most widely used resins for TcO_4^- separation through extraction chromatography [31], [57], [60]–[63]. As previously discussed in Chapter 1, the active component of the TEVA resin is an aliphatic quaternary amine called Aliquat 336, shown in Figure 4-1. The most commonly used procedure to determine the levels of TcO_4^- in water is the following. First, a TEVA resin column is prepared and TcO_4^- is separated from other interfering species through anion exchange chromatography. Then, technetium is desorbed by washing the column with high concentrated HNO_3 solution, the eluent is collected and measured by using liquid scintillation spectrometry or ICP-MS [33], [146].

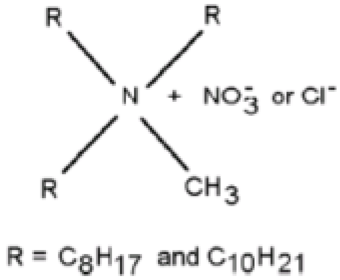

Figure 4-1. The structure of the active component of TEVA resin, trialkyl methylammonium nitrate (or chloride) or Aliquat 336.

In this chapter, investigations towards a TEVA- functionalized QCM that could immediately detect TcO_4^- in real time by the changes in mass occurring as a result of the exchange of with the lighter NO_3^- or Cl^- as the counter anion of Aliquat 336 is reported.

4.1 Immobilization of TEVA resin particles on QCM within a hydrogel matrix

TEVA resin is commercially available from Eichrom Technologies LLC as a granular product with a particle size in the range of 20-50 µm. An effective way to tether the TEVA grains onto the QCM surface may be by incorporating them into a hydrogel coated onto the sensing area of the QCM as a film, an approach that has been attempted in the literature. Water can permeate through the hydrogel and facilitate contact with the TEVA grains, where the selective capture of TcO_4^- will take place by the TEVA resin particles.

The hydrogel was prepared, as reported in the literature [147], [148] by the free-radical crosslinking copolymerization of an acrylamide (AAm) monomer with N,N'-methylenebisacrylamide (MBAAm) acting as a crosslinker, while ammonium persulfate (APS) and tetramethylethylenediamine (TEMED) aqueous solutions were used as redox initiators. However, the procedure was optimized to achieve the viscosity needed to coat the film on the QCM via spin coating and TEVA particles were also added in the reaction mixture.

The first step in the polymerization process is a reaction between TEMED and APS which generates free radicals from persulfate. The persulfate free radicals covert AAm monomers to free radicals which then react with other inactivated monomers to begin the polymerization reaction. The TEMED molecule is also left with an unpaired valence electrone, which is transferred to monomeric MBAAm units. The reactive MBAAm units are then able to create cross-links between polyacrylamide chains, thus creating a network rather than unconnected linear chains. More monomers or comonomers can therefore be activated and attached in the network in this way. A reaction scheme of the polymerization process is shown in Figure 4-2.

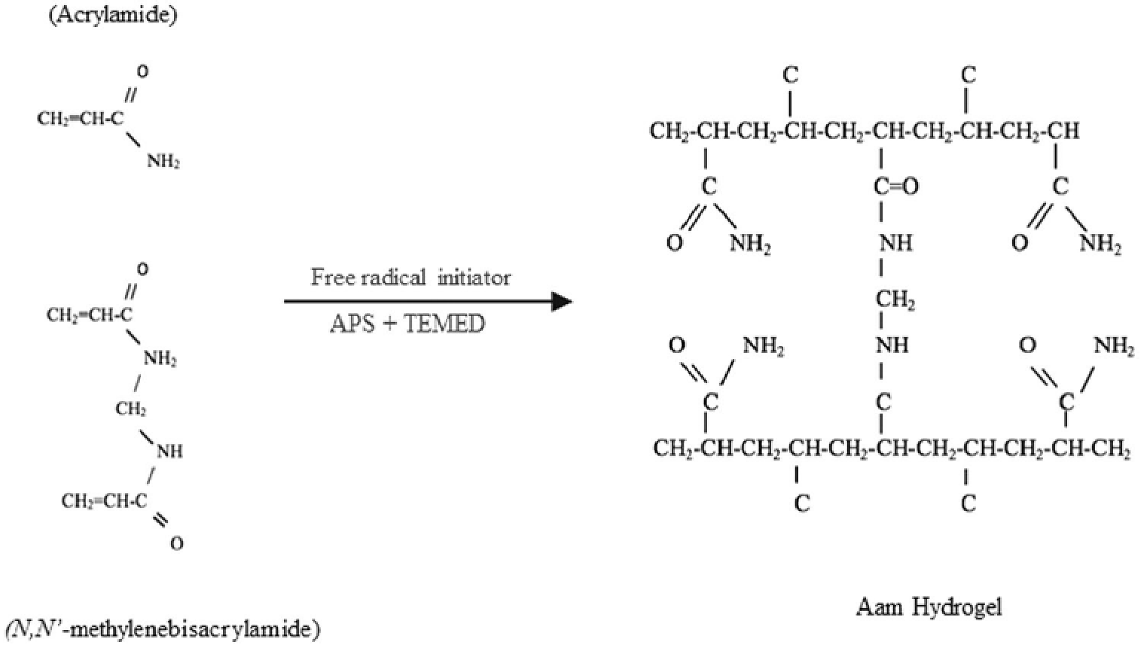

Figure 4-2. The polymerization process of the AAm-MBAAm hydrogel.

4.1.1 Preparation of the hydrogel coating

Specifically, 400 mg of AAm/MBAAm 37.5:1 mix, 1.0 mL $(NH_4)_2S_2O_4$ 0.06 M aqueous solution, 1.0 mL TEMED 0.06 M aqueous solution and 20 mg TEVA resin were added in 2.0 mL of DI water. Then, 20 µL of the above solution were added on the QCM, which was spin coated for 3 min at 6000 rpm. Finally, after the film was homogeneously dispersed on the surface of the QCM, the crystal was left to dry overnight at 60 ^oC. As it can be seen in

Figure 4-3 shows an optical microscope image of the hydrogel coating where it may be seen that the hydrogel is clean, free of air bubbles that could constrain the even absorption of water, and the TEVA grains are evenly dispersed on the surface of the QCM.

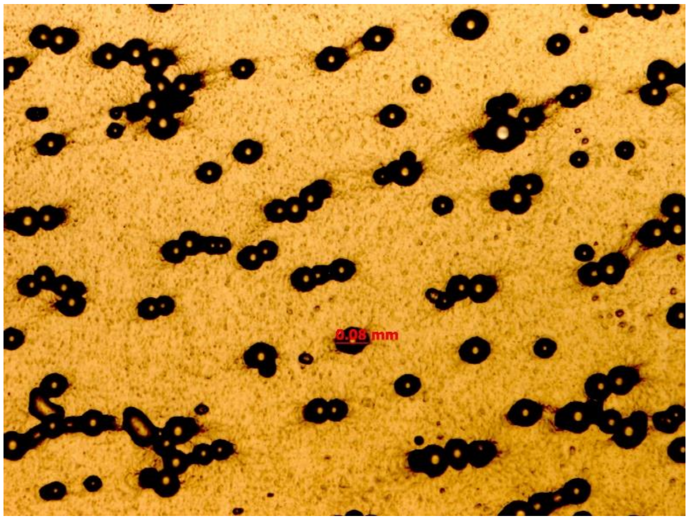

Figure 4-3. Optical microscope picture of the coated QCM. The hydrogel is clean of air bubbles and the TEVA grains are evenly distributed on the surface. The average size of the beads is 50-80 μm.

4.1.2 QCM response

After the coating was prepared, the hydrogel-coated QCM was immediately tested for the detection of the non-radioactive surrogate, ReO_4^-. So, the coated QCM was mounted on the QSH-dip sensor holder and connected to the MAXTEK RQCM system. The holder was immersed in 50 mL of DI water and allowed to equilibrate for 6 min prior to titrating and then aqueous solution of $NaReO_4$ was titrated, increasing the concentration by 0.9 mM with every titrant addition at 1 min intervals. The resulting chronomassogram is presented in Figure 4-4. From this, it may be seen that, the behaviour of the QCM was rather unexpected. Immediately after it was immersed in the water, there was a very steep increase in the resonant frequency, which was stabilized just after just 2 min at $\Delta f = 913$ Hz. At the 6 min mark and every minute thereafter, 0.9 mM of $NaReO_4$ were titrated in the solution, but no meaningful change in the frequency was observed, apart from ± 3 Hz caused by the mixing of the solution, as may be seen in Figure 4-5.

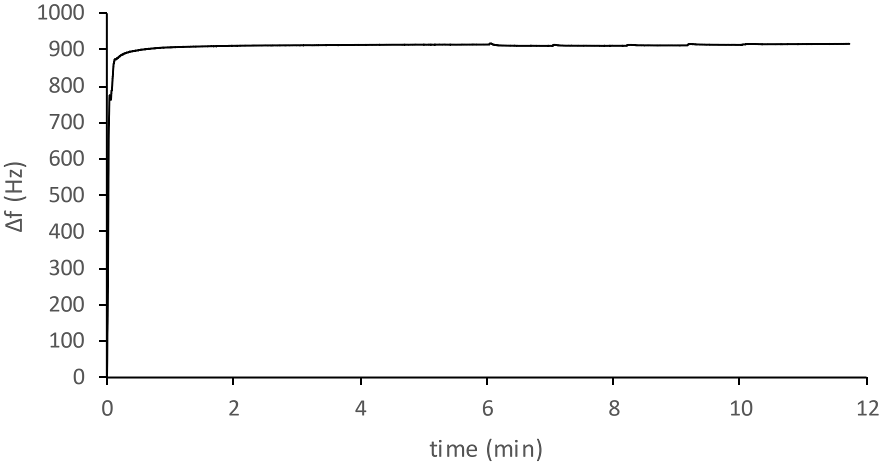

Figure 4-4. Behaviour of the QCM coated with TEVA-loaded hydrogel in the water and in presence of NaReO$_4$*. At 6 min and every minute after, 0.9 mM of NaReO*$_4$ *were titrated in the solution.*

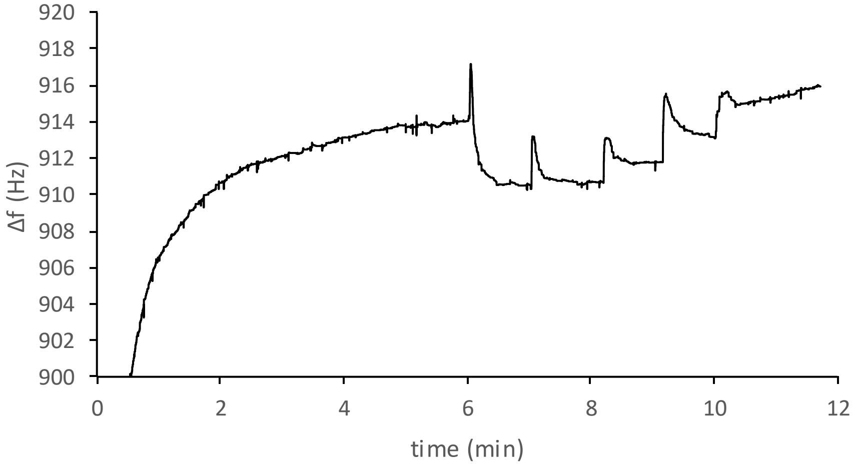

Figure 4-5. Zoomed-in version of Figure 4-4, between 900-920 Hz. Behaviour of the QCM coated with TEVA-loaded hydrogel in the water and in presence of NaReO$_4$*. At 6 min and every minute after, 0.9 mM of NaReO*$_4$ *were titrated in the solution.*

A number of competing factors must be considered when analyzing the above data. First, the dry hydrogel is expected to swell rapidly as a result of hydration when exposed to water [149], which would lead to an increase in the mass of the layer and therefore a decrease in the frequency. At the same time, the layer transforms from a rigid film into a larger more flexible structure, leading to damping of the signal which should also lead to an apparent mass increase and therefore frequency decrease. This change will also resolve some of the stresses induced at the QCM-hydrogel interface created as the film was allowed to dry these are likely to be very significant as the hydrogel was deposited in its hydrated form and can contain up to 5.7 g water per g of dry polymer. This would be equivalent to a mass loss (frequency increase). The introduction of water into the film matrix may also lead to a kind of induced buoyancy between the hydrogel and the water, leading to an apparent mass decrease (frequency increase) on the QCM and the swelling of the film may move some of the expanded layer outside the reach of the sensing element resulting in an apparent mass loss.

It appears that the swollen hydrogel restricts anion detection in an aqueous solution, so it was decided not to investigate tethering of TEVA resin to a QCM any further. In fact, the size of the TEVA resin grains appear to be too large, having a diameter of 20-50 µm, to sit comfortably within the sensing layer of the QCM, since any coating would exceed by far the maximum distance of detection from the QCM surface, which ranges between the upper hundreds of nm to a few µm, depending on the viscosity and density of the liquid media and the coating [150]. For this reason, it was decided to investigate the direct tethering of its active molecule, Aliquat 336, by synthesizing a derivative that can form a self-assembled monolayer on the gold electrode of the QCM.

4.2 Synthesis of Aliquat 336 derivative

Aliquat 336 comprises of a quaternarized amine consisting of a methyl group and three alkyl chains of 8-10 carbons in length, as shown in Figure 4-6. In order to facilitate the tethering of this derivative onto the QCM in the form of a SAM, a disulfide should be present on the molecule, similarly to the TREN ligand described in the previous chapter 3. The structure of the novel Aliquat 336 derivative is shown in Figure 4-6. So, in the same way as in Chapter 3, attachment of the ligand onto the QCM will occur by reaction of the disulfide with the Au surface, while the detection of pertechnetate and perrhenate anions will occur by binding at the Aliquat 336 active group, which will be exposed in the solution.

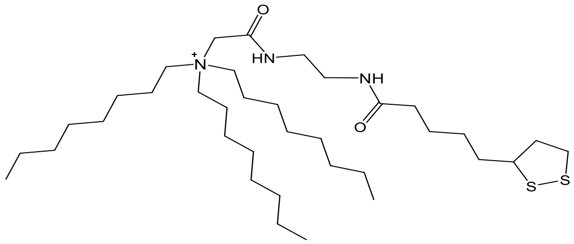

Figure 4-6. Structure of the novel Aliquat 336 derivative.

For the synthesis of the Aliquat 336 derivative, a synthetic route consisting of 4 steps was designed, as shown in Figure 4-7. Since the methyl group of Aliquat 336 is not labile, direct modification of the actual the Aliquat 336 molecule is not possible. Instead, since the methyl group is not a removable agent, trioctylamine was used as the basic starting material since it replicates the three long carbon chains of the target molecule and is commercially available material. As in Chapter 3 for the TREN derivative, thioctic acid was used as the carrier of the disulfide, and was connected to the trioctylamine through the formation of amides.

The alkylation process, which yielded compound 1, was a quite slow reaction and an accurate calculation of the yield is impossible since the counter anion of the quaternary amine is not known, as it will be explained in the experimental section, however an estimation would be 60% - 70% yield. The synthesis of this molecule has been reported before [151]. Then, the hydrolysis of compound 1, which yielded compound 2, was a fast reaction with a yield estimate of 80% - 90%. This molecule has also been reported [152].

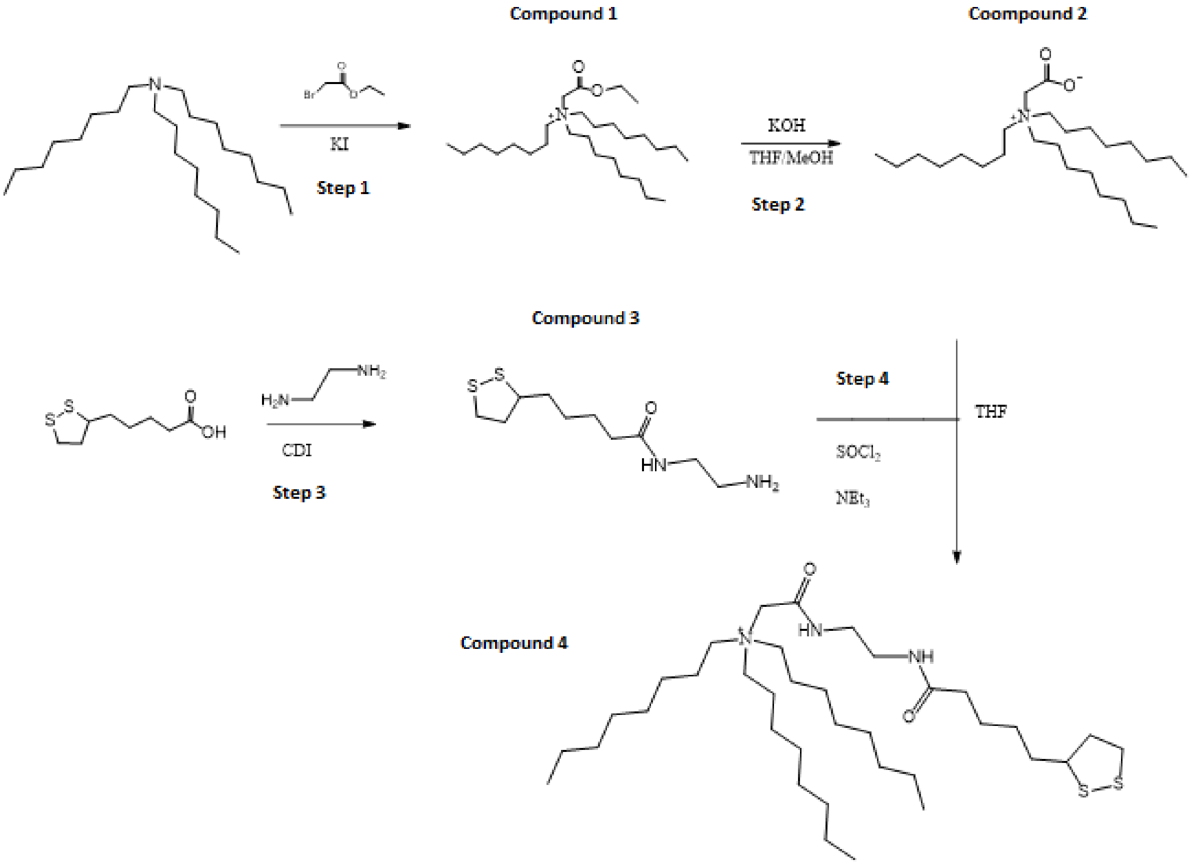

Figure 4-7. Synthetic route of the novel Aliquat-336 derivative.

Step 3 of the above synthetic route is exactly the same as step 4 of the TREN synthetic route discussed in Chapter 3, concerning the handling of thioctic acid. Finally, compound 4 was synthesized by using the same activating agents and solvents that were proved effective in the amide formation of the TREN derivative. This time the yield was slightly better (~ 25%), and compound 4, which is a novel molecule, was fully characterized with ^{1}H NMR, ^{13}C NMR, IR and MS.

4.2.1 Experimental section

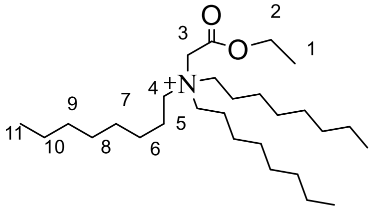

Compound 1

Trioctylamine (800 mg, 2.27 mmol) was dissolved in 10 mL of MeCN under Ar atmosphere. Ethyl bromoacetate (1.13 g, 6.81 mmol) was added dropwise and then the reaction was heated to 70 °C and stirred overnight. Inspection with TLC the next day showed that the reaction had not occurred yet, so KI (753 mg, 4.54 mmol) was added in order for I^- to replace Br^- as a better removing agent and the solution was stirred for another 48 hours. Analytical TLC showed that the reaction had occurred but also that the product needed to be purified. So, the solvent was removed and the crude material was purified with silica gel column chromatography (96/4 CH_2Cl_2/CH_3CN) which yielded 804 mg of compound 1 as yellow oil. It is not known if the counter anion is Br^-, I^- or a mix of both, so the actual yield cannot be calculated. The product was characterised with ^1H NMR , IR and mass spectroscopy.

*δ*H (400 MHz; $CDCl_3$) 4.69 (*2H, s, C^3H*), 4.27 (*2H, q, C^2H*), 3.63 (*6H, t, C^4H*), 1.75 (*6H, quint, C^5H*), 1.34 (*3H, t, C^1H*), 1.26 (*30H, s, $C^{6-10}H$*), 0.87 (*9H, s, $C^{11}H$*)

ν_{max} / cm^{-1} (neat) 2924, 2856 (C-H), 1742 (C=O), 1209 (C-N), 1032 (C-O)

m/z (ES) $[M]^+$ 440.4453, $C_{28}H_{58}NO_2$ predicted 440.4462

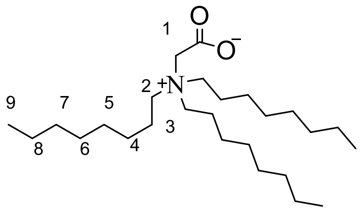

Compound 2

Compound 1 (300 mg) was dissolved in a 1/1 mix of 30 mL THF/CH_3OH. An aqueous solution (2 mL) of KOH (76 mg, 1.36 mmol) was added to the above solution and the reaction was stirred overnight. Then, the solution was concentrated in the rotary evaporator in about 7-10 mL and 50 mL of CH_2Cl_2 were added. The solution was washed with deionised water (3 x 50 mL), in order to remove the ethanol produced by the hydrolysis of the ester and any inorganic salt that may had been formed. The aqueous layer was collected and washed 2 times with CH_2Cl_2, as some of the product could have remained there. Finally, all the organic layers of CH_2Cl_2 were collected in one solution which was concentrated and dried to yield compound 2 (200 mg) as an amber resin, confirmed by ^{1}H NMR, IR and mass spectroscopy.

*δ*H (400 MHz; $CDCl_3$) 3.65 (*2H, s, C^1H),* 3.50 (*6H, t, C^2H)*, 1.64 (*6H, quint, C^3H)*, 1.28 (*30H, s, $C^{480}H$*), 0.90 (*9H, s, C^9H*)

ν_{max} / cm^{-1} (neat) 2924, 2853 (C-H), 1638 (C=O), 1354 (C-N)

m/z (ES) $[M]^+$ 412.4142, $C_{26}H_{53}NO_2$ predicted 412.4149

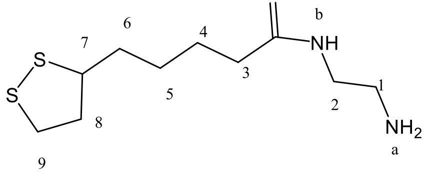

Compound 3

Thioctic acid (120 mg, 0.584 mmol) and carbonyldiimidazole (190 mg, 1.16 mmol) were dissolved in 5 mL of dry CH_2Cl_2 under Ar atmosphere and cooled down to 0 ^oC. Ethylene diamine (0.39 mL, 5.84 mmol) was added dropwise into the above solution and the reaction was stirred at room temperature for 2 hours. Then, the solution was washed with brine (2 x 20 mL), in order to remove the excess of ethylene diamine, and the organic phase was dried with Na_2SO_4. Finally, the solvent was removed to yield compound 3 as a yellow oil. The product was only characterized with ^1H NMR, with data consistent with previous reports [143].

δH (400 MHz; $CDCl_3$) 5.93 *(1H,s)*, 3.59 (*1H, m),* 3.33 *(2H, q)*, 3.15 (*2H, m)*, 2.86 (*2H, t),* 2.48 *(1H, m),* 2.22 (*2H, t),* 1.93 *(1H, m),* 1.71 *(4H, m),* 1.51 *(2H, m)*

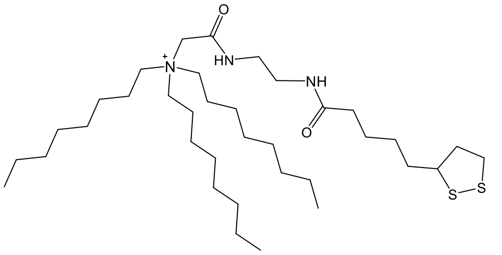

Compound 4 / final product

Compound 3 (115 mg, 0.467 mmol), compound 2 (120 mg, 0.292 mmol) and trimethylamine (0.12 mL, 0.876 mmol) were dissolved in 5 mL anhydrous tetrahydrofuran under Ar atmosphere and cooled down to 0 ^oC. Then, $SOCl_2$ (104 mg, 0.876 mmol) was added dropwise and the reaction was stirred for 3 hours at room temperature. After that, 20 mL of CH_2Cl_2 was then added and the solution was washed with brine (3 x 30 mL). The combined organic phases were dried with Na_2SO_4 and the solvent was removed in vacuum. The crude material was purified with silica column chromatography 98/2

CH_2Cl_2/CH_3OH to yield compound 4 as amber sticky resin (45 mg, 25%). Compound 4 was characterized with ^1H NMR, ^{13}C NMR, IR and mass spectroscopy.

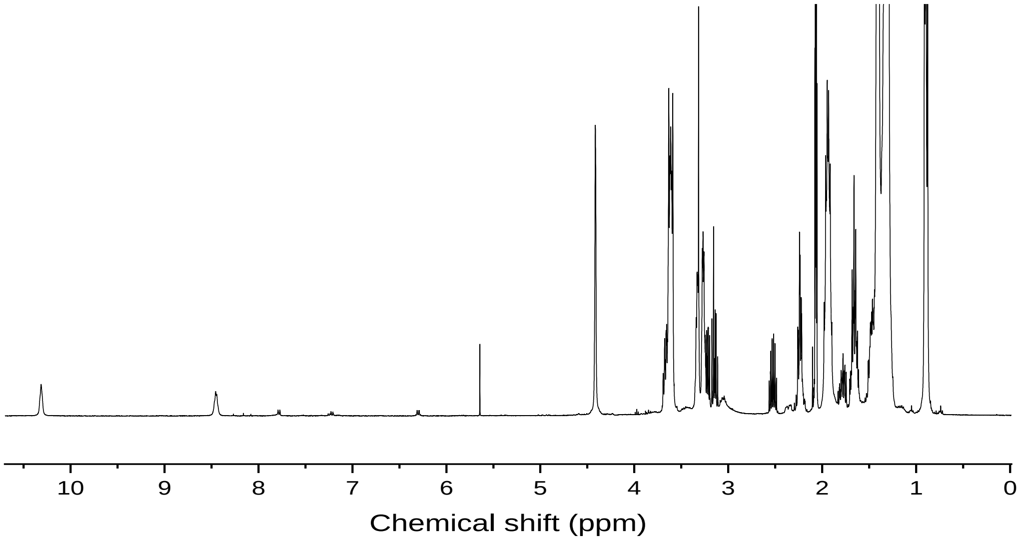

Figure 4-8. ^1H NMR spectrum of compound 4, in $CDCl_3$.

δH (400 MHz; $CDCl_3$) 10.35 *(1H,s)* 8.48 *(1H,s)*, 4.41 *(4H,s), 3.65 (2H, s),* 3.59 (*1H, m), 3.32 (6H, t),* 3.26 *(2H, q)*, 3.16 (*2H, m)*, 2.50 (*2H, m), * 2.13 *(1H, m),* 1.95 (*2H, t),* 1.83 *(1H, m),* 1.71 *(3H, m), 1.64 (6H, quint),* 1.28 (*27H,*), 0.90 (*9H, s*) ppm.

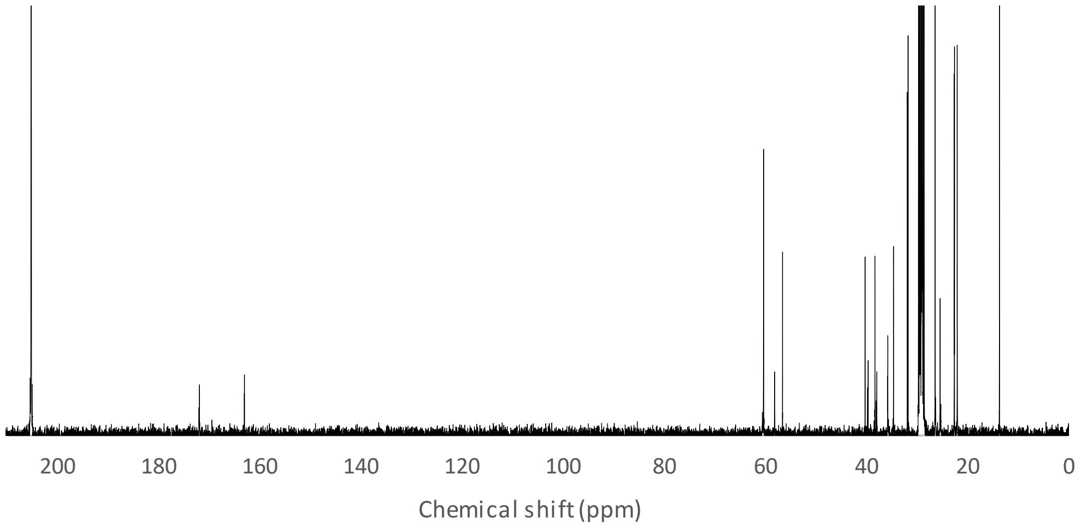

Figure 4-9. ^{13}C NMR spectrum of compound 4, in d6-acetone.

δC (100 MHz; d6-acetone) 171.90, 163.02, 60.13, 58.03, 56.48, 40.12, 39.64, 39.52, 38.15, 37.90, 37.78, 35.57, 34.46, 31.74, 31.60, 26.21, 25.27, 22.39, 21.88, 13.50

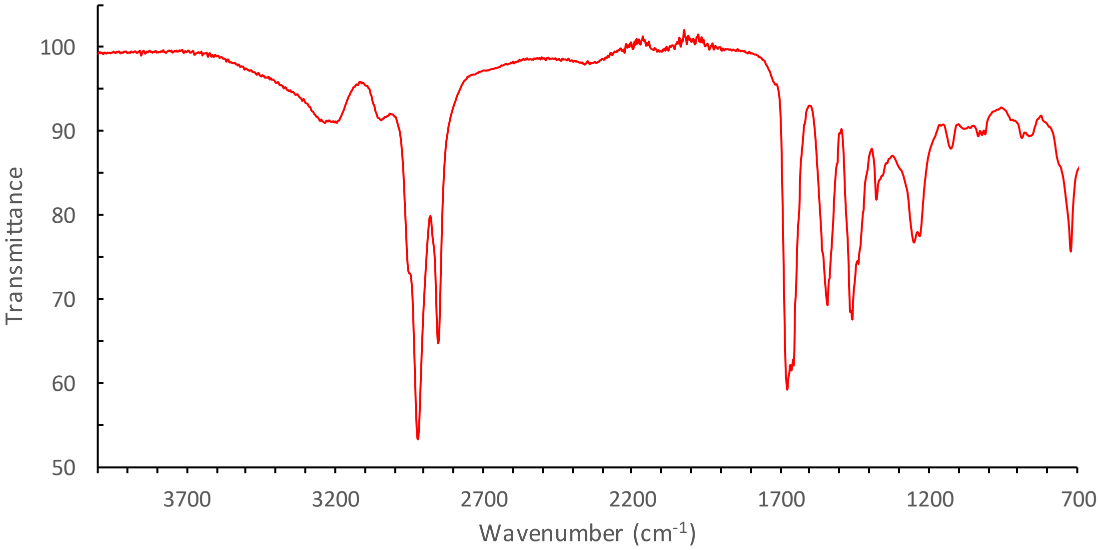

Figure 4-10. IR spectrum of compound 4.

ν_{max} / *cm^{-1}* (neat) 3201 (N-H), 2924, 2853 (C-H), 1671, 1539 (C=O), 1230 (C-N)

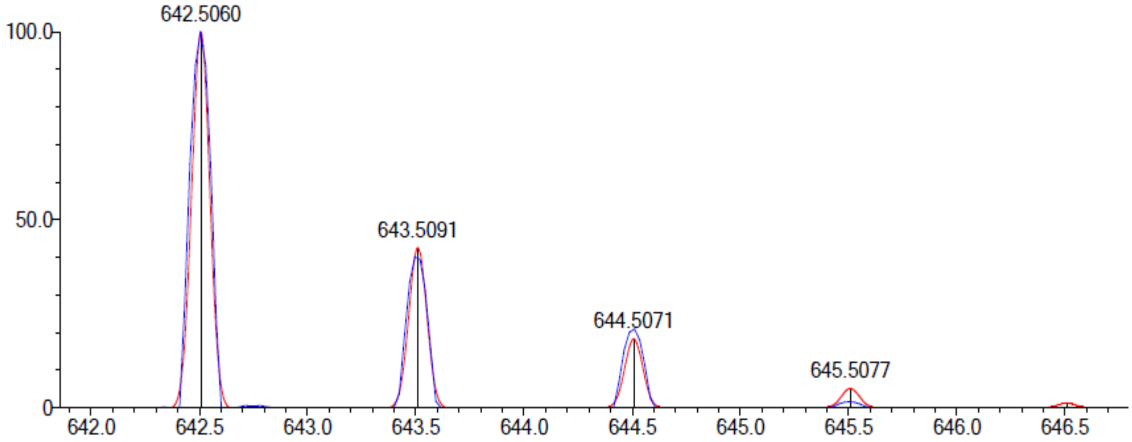

Figure 4-11. Mass spectrum of compound 4.

m/z (ES) $[M]^+$ 642.5041, $C_{36}H_{72}N_3O_2S_2$ predicted 642.5060

4.3 Deployment of the Aliquat-336 derivative on the QCM

Modification of the QCM crystal was achieved by the formation of a SAM of compound 4 by exploiting the strong affinity of sulfur for gold, as it was explained in Chapter 3. The QCM crystal was treated with piranha solution, which is a 3:1 mixture of H_2SO_4 and H_2O_2, in order to remove any organic residues and impurities off from its gold surface, and its front side treated by exposure to. Then the front side of the QCM was exposed to a 10 mM ethanolic solution of ligand for 24 h.

After the SAM was prepared, the coated QCM was immediately tested for the detection of ReO_4^-. The coated QCM crystal was placed in the QCM holder and was suspended in a beaker with 50 mL of DI water to equilibrate at room temperature for a few minutes. Then 0.9 mM solution of $NaReO_4$ was added in the beaker from minute 20 and every 2 minutes, as shown in Figure 4-12. However, no change in the frequency was observed, apart from some ± 4 Hz due to the perturbation induced by stirring the solution. This was repeated several times, but no detection was monitored.

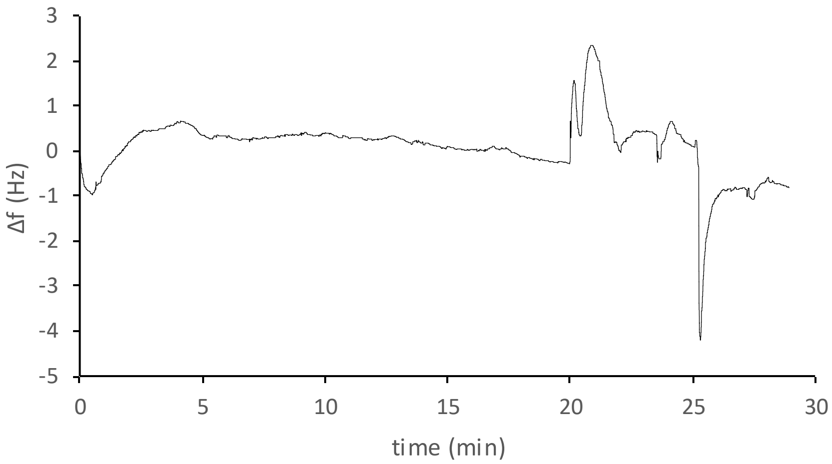

Figure 4-12. Behaviour of the Aliquat-336 coated QCM in the presence of ReO₄⁻. Aliquots of 0.9 mM of NaReO₄ were introduced in the solution at minute 20 and every 2 minutes afterwards, but only an instant perturbations of ± 4 Hz due to the stirring were observed.

Since the ligand was fully characterised, a possible explanation for this is that a single monolayer is not enough to provide traceable frequency deviation of a light molecule such as ReO_4^-. As it was previously explained, Aliquat-336 has been reported for the selective capture of ReO_4^-, but it had been always used in the form of column chromatography, which provides a huge active surface area. So, when it is reduced to just a single monolayer, its effectiveness may also be reduced.

In order to make more sense of this, it would be helpful to estimate the number of molecules of the Aliquat-336 derivative in a single SAM. Figure 4-13 shows the structure of the Aliquat-336 ligand and its dimensions, calculated in Å via the "Avogadro" software [147]. Assuming a 30 ° angle between the disulfide of the ligand and the QCM gold surface [85]leads to an estimated molecular footprint of 432 $Å^2$, indicating that a SAM of the Aliquat-336 ligand on the 19.63 mm^2 piezoelectric area, defined by the 5 mm back electrode, contains 4.545×10^{12} molecules.

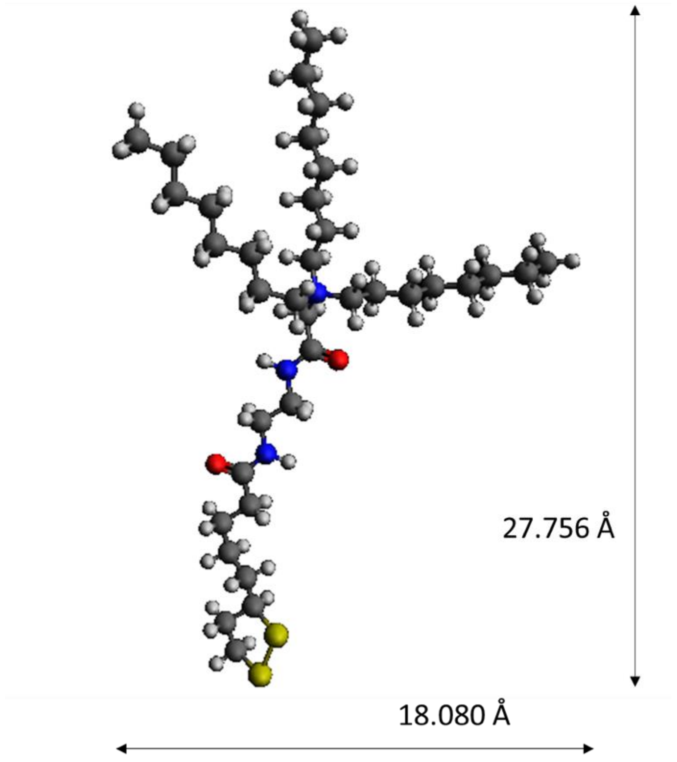

Figure 4-13. Footprint of the Aliquat-336 derivative.

A few more assumptions have to be made at this point, including that the counter anion in presence before the exposure is Cl^-, since the final product was treated with brine, and that every molecule in the SAM interacted with ReO_4^-. So, taking into account the 233 g/mol mass difference between ReO_4^- and Cl^- and the number of molecules present in the SAM, a mass change of 1.76 ng should be expected after the anion exchange. This corresponds to a 0.5 Hz shift in the frequency, which actually lies on the error margin of the QCM response. Of course, the above is only a crude estimation, but it helps us understand why a single monolayer of the Aliquat-336 ligand may not be enough to detect ReO_4^-.

4.4 Conclusion

An attempt to tether TEVA resin grains directly on the QCM through a Aam/MBAAm hydrogel coating was undertaken However, the swelling of the hydrogel because of the water absorption constrained its use a means of coating. For this reason, a novel derivative of the active component of TEVA resin, Aliquat 336, that can be tethered on the QCM through a SAM was prepared by multi-step chemical synthesis. The novel compound was fully characterized by ^{1}H NMR, ^{13}C NMR, IR and MS. However, no detection of ReO_4^- was observed when the compound was added to the QCM surface. This could be due to very small frequency changes resulting from only a small number of anions being accepted within the Aliquat-336 derivative caused by the presence of only a single monolayer on the crystal.

Considering the potential issues in using SAM modified QCMs for the detection of ReO_4^- identified in Chapters 3 and 4, it was decided to explore multi-layered functionalized QCMs. Thus, in the next chapter, the work towards a multilayer metal-organic framework thin film is reported.

CHAPTER 5

5 Ag-4,4’-bipyridine metal organic framework

Metal organic frameworks (MOFs) also known as porous coordination polymers (PCPs) are highly porous and crystalline complexes comprised of metal centers and organic linkers. Originally fabricated for applications in gas storage, gas separation and catalysis, in recent years these materials have been used in separation applications [72][73]. In contrast to amorphous materials, MOFs provide a periodic and strictly defined structural network that can host guest molecules, thus permitting systematic investigation [74].

The particular MOF under investigation, Ag-4,4'-bipyridine, was first reported by Robinson *et al.* [154], and forms a network where each silver ion is linked to two nitrogens of different but symmetrical 4-4,bipyridine units, which are aligned in a nearly linear coordination, crosslinked through silver-silver bonds leading to a 3-D framework. Nitrate counter anions serve to neutralize the charge of the cationic metal centers [155][156]. Recently, this MOF was reported as an effective adsorbent for the removal of ClO_4^- from aqueous solution with remarkably high capacity through anion exchange. Thus, the ClO_4^- anions were exchanged with the NO_3^- in the network, stabilizing the structure of the crystal itself. This process was found to be reversible, meaning that the perchlorate ions could be removed from the crystal structure by exposure to a very highly concentrated solution of NO_3^- [79]. This framework was later also reported by a different team as an exceptionally selective adsorbent for ReO_4^-, the stable chemical surrogate for TcO_4^-. Although the mechanism was again anion exchange, namely the ReO_4^- anions replaced the NO_3^- in the network, the process was found to be irreversible, as the [Ag-4,4’-bipyridine]ReO_4^- structure seemed to be significantly more stable than the initial [Ag-4,4’-bipyridine]NO_3^- [157].

The selective adsorption of ReO_4^- by the Ag-4,4-bipyridine MOF motivated us to synthesize and tether it to the QCM surface in order to monitor the adsorption of perrhenate in real time and consequently determine the potential viability of a pertechnetate specific in-situ monitoring sensor.

5.1 Synthesis of the bulk crystals

Metal Organic Frameworks are usually synthesized by hydrothermal methods, where a mixture of $AgNO_3$, 4,4'-bipyridine and deionized water is loaded in an sealed autoclave and heated up to 150 °C for several hours [79], [158]. However, since our approach relies on the production of a thin film tethered to the surface of a QCM crystal we adapted the methodology to enable the deposition of the MOF onto our preferred substrate, as follows.

An aqueous solution of silver nitrate (10 mg in 1mL of deionized water) and a solution of 4,4-bipyridine (10 mg in 1mL acetonitrile) were mixed at room temperature, forming a white precipitate. A 10 µL aliquot of the suspension was then spin-coated onto the surface of a QCM at 4000 rpm for 30 seconds. The coated QCM was subsequently heated in a furnace at 150 °C for 16 hours. Figure 5.1 shows an SEM image of the crystals obtained from this procedure (A) and the SEM found in the literature for the bulk production of the same MOF (B) [158].

As may be seen from Figure 5.1A, the morphology of the crystals is clearly visible. In comparison to the crystals shown in Figure 5.1B, which is taken from the literature [158], we can see that while their structure looks quite similar, our crystals are significantly smaller (approximately 5-10 µm in comparison to 30-50 µm), probably as a result of the different synthetic processes used. The structure of the crystals is of great significance, as will be seen in the following section, because it can provide evidence of ReO_4^- adsorption.

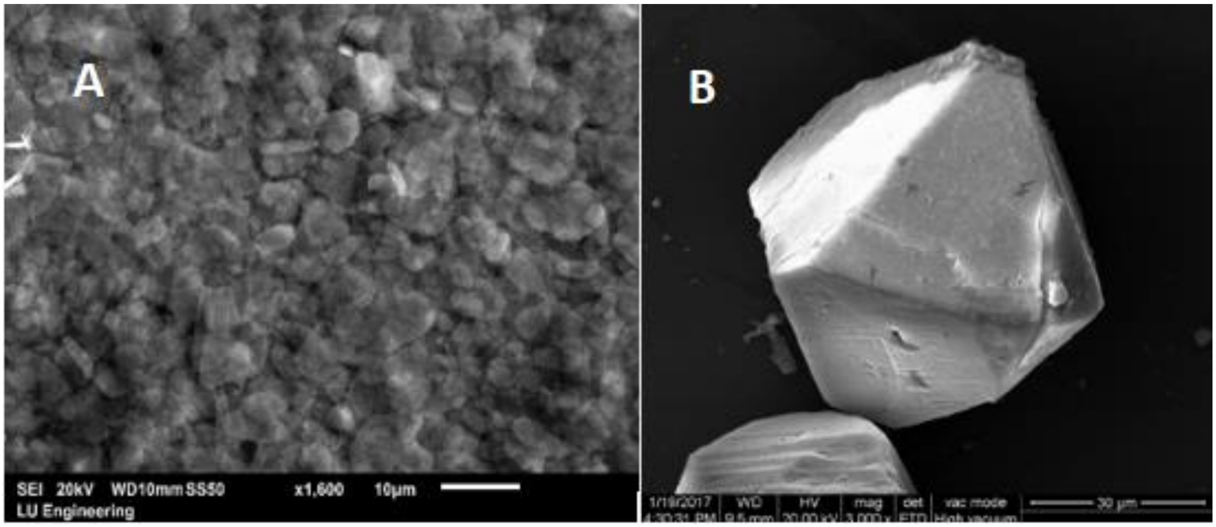

Figure 5-1 A) SEM picture of our Ag-4,4-bipy crystals after the spin coating at 4000 rpm for 30 seconds and 16 hours in the furnace at 150 °C. B) SEM picture of the same MOF taken from Zhu et al 2017 [158]

5.2 Exposure of the bulk crystals on $NaReO_4$

Adsorption experiments were carried out by exposing the coated QCM to a solution containing $NaReO_4$. In this procedure, the QCM was mounted on the QSH-dip sensor holder connected to a MAXTEK RQCM Quartz Crystal Microbalance Research System, which monitors the changes of the resonant frequency of the crystal. The holder was suspended in a 100 mL beaker containing 50 mL of deionized water and was left to equilibrate before an aliquot of an aqueous solution of $NaReO_4$ was titrated into the beaker. The experiment took place at room temperature and at pH 7. Figure 5-2 shows the response of the coated QCM to the addition of 2.76 mmol L^{-1} $NaReO_4$ at 2.8 minutes.

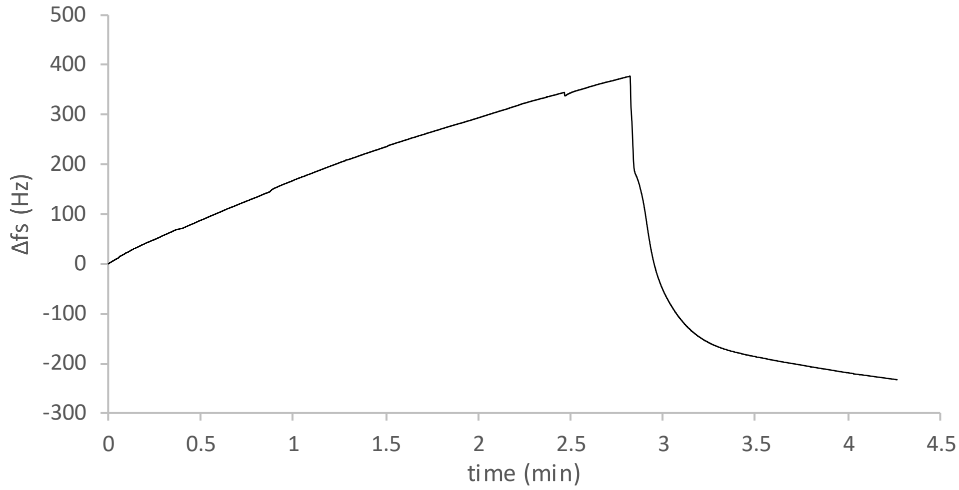

Figure 5-2 The change in resonant frequency of the coated QCM in the presence of 2.76 mmol L^{-1} $NaReO_4$.

Typically, a QCM is left to equilibrate for a relatively long time (>10 min) in the solution of interest, in our case deionized water, before starting the experiment. This needs to be done because the QCM is very sensitive and even small change in temperature, for example, could have a significant effect on the measurements. However, in this case, a significant increase of 376 Hz in the resonant frequency is observed over the first 2.8 minutes. This is interpreted as a decrease in mass from the QCM surface, which could be due to a partial detachment (via solubilization or otherwise) of the MOF crystals from the QCM surface into the solution.

As a result, at 2.8 minutes, an aliquot of $NaReO_4$ was titrated into the 50 mL deionized water, and the solution gently homogenized to produce a bulk concentration of 2.76 mM $NaReO_4$ in the test solution. At this point, a very steep decrease in observed in the resonant frequency. This can be explained by the adsorption of ReO_4^- anions into the MOF crystal structure.

Since perrhenate adsorption appears to occur concurrently to the detachment of the MOF crystals from the QCM surface, it is instructive to attempt to separate these effects in order to estimate the take up of perrhenate into the MOF structure. The initial increase in frequency in the absence of perrhenate ion can be extrapolated to predict the effect of the loss of MOF content up until the end of the experiment and used as the baseline to determine the frequency change due to the adsorption of perrhenate onto the crystal. This was carried out using a 2nd degree polynomial equation up to minute 4.26, as shown in Figure 5-3, which marks the total frequency decrease due to the adsorption of ReO_4^-. This extrapolation does not contain any physical meaning that may assist to understand the process, but it produces the theoretical total increase in frequency if the adsorption had not taken place, which would be 461 Hz. The total decrease in frequency can now be estimated as -694 Hz, corresponding to a mass increase of about 12 µg/cm^2.

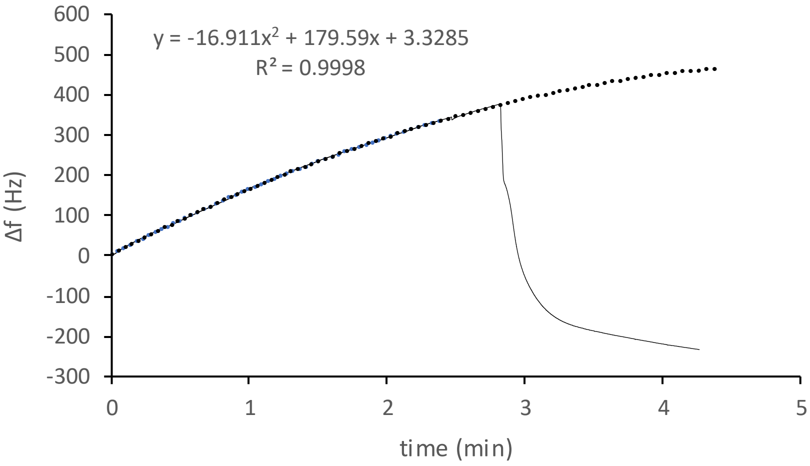

Figure 5-3. Extrapolation of the increase in frequency observed until minute 2.5, shown with the dotted line.

Figure 5-4 shows the coating of the MOF crystals on the QCM surface after the experiment presented previously. It is clearly visible that some of the MOF crystals initially deposited on the QCM substrate have become detached and no longer cover the entire piezoelectric area. This means that the QCM data, recorded in mass per surface area, can only be partially analysed. It is also clear from Figure 5-4, that where crystals are present, the coating is not uniform, as crystals of different sizes can be observed. Although the thickness of the coating cannot be accurately measured, it can be estimated in the range of a few micrometers up to 10-20 µm, according to the scale of Figure 5-4. This means that some of the coating may exceed the maximum distance of detection from the QCM surface, which ranges from several hundreds of nm to a few µm, depending on the viscosity and density of the liquid media and the coating [150]. It is therefore possible that some of the ReO_4^- adsorbed outside of this sensing layer and was not recorded. For those reasons, quantitative analysis of the adsorption data is restricted, but qualitative analysis remains possible.

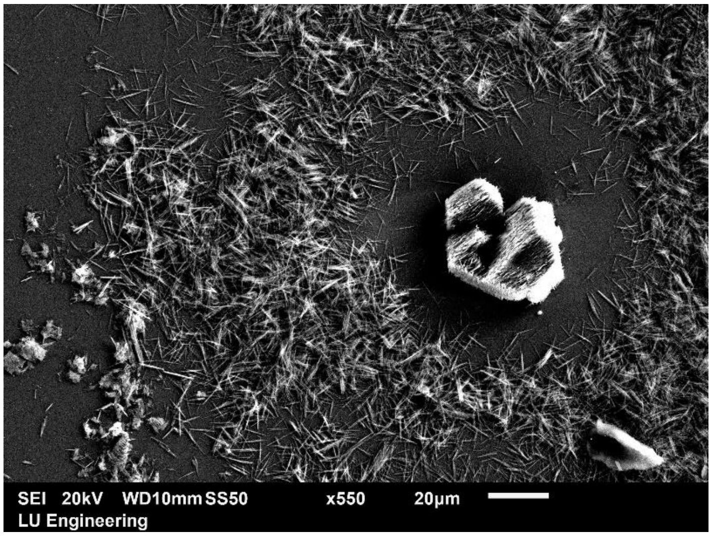

Figure 5-4. SEM pictures of the Ag-4,4-bipy MOF crystals on the QCM surface after the exposure to ReO_4^-.

Figure 5-5 shows the Ag-4,4-bipy crystals after exposure to ReO_4^- anions under the conditions described above (zoomed-in form Figure 5-4) (A) and from reports in the literature (B) [158] . As it can be seen by comparison with Figure 5-1, the structure of the crystals is critically affected by exposure to perrhenate. In their report, Zhu *et al.* [158], show that the exchange of NO_3^- by ReO_4^- favors the formation of a much denser hydrogen bond network, altering irreversibly the structure of the MOF from octahedral crystals to needle-like structures as shown in Figure 5-5.B. Figure 5-5A shows the morphology of the MOF crystals attached to the QCM after exposure to perrhenate and confirming the transformation into needle like structures.

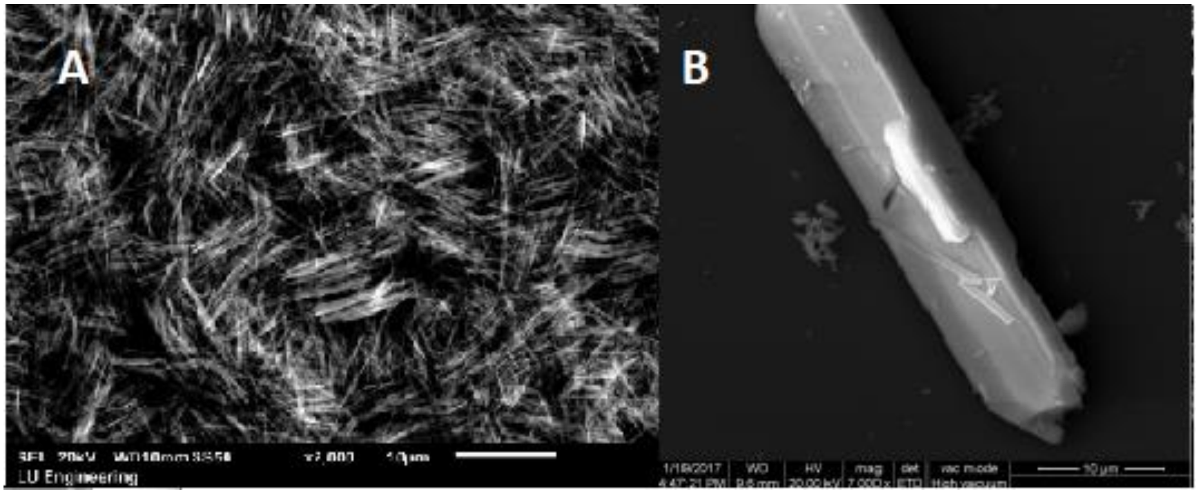

Figure 5-5 SEM pictures of the Ag-4,4-bipy MOF crystals after the exposure to ReO_4^- A) on our QCM (scale bar 10 µm) and B) taken from Zhu et al 2017 (scale bar 10 µm) [158].

In addition, the EDX spectrum taken of the QCM surface post exposure, confirms the presence of Re, as shown in Figure 5-6. Other elements shown on the spectrum are Ag, C and O from the MOF, Au, Ti and Si from the QCM. The N peak, from the 4,4-biyridine is overlapped by the C peak.

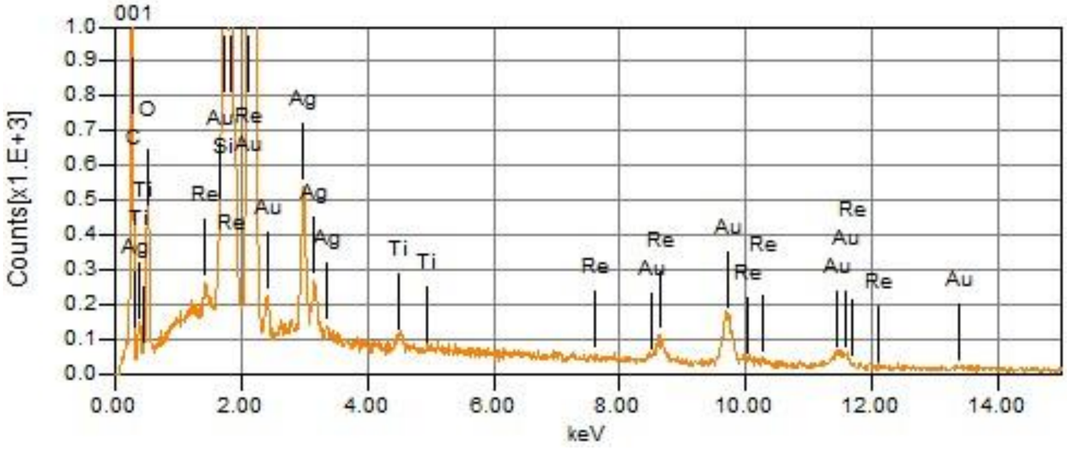

Figure 5-6 EDX spectrum on the coated QCM, after the exposure to ReO_4^-.

The results presented in this section show that a real time sensor incorporating a thin layer of Ag-4,4-bipy MOF on a QCM transducer could be developed for the real time in-situ monitoring of pertechnetate ions. However, the initial loss of mass from the QCM surface suggests that the production methodology of the crystals must be refined to prevent a decrease of sensitivity over time and to produce a uniform and stable coating. Layer by layer methodologies have been employed for the production of thin film layer of MOFs onto QCM transducers and the following section explores the feasibility of deploying these for the tethering of Ag,4,4'-bipy onto QCM crystals.

5.3 Thin film

The main problem of the coating with the bulk crystals is that it is not chemically anchored on the surface of the QCM, making it easy for the crystals to detach by small perturbations in the solution. On the contrary, a MOF thin film is chemically tethered to the surface of the QCM and thus much more stable.

There are several different approaches to the synthesis of MOF thin films, as it was explained in detail in section 1.6.2.2, such as electrochemical deposition, chemical vapour deposition and powder deposition [87], although the most widely applied is the liquid phase epitaxy or layer-by-layer (LbL) assembly [86]–[90]. The process that was used in our study was the layer-by-layer growth (LbL). In this approach, the substrate, usually a gold surface, is functionalized with a self-assembled monolayer (SAM), through a thiol-gold bond with an exposed active group such a carboxylic acid, hydroxyl or pyridine group, on which the film is built [88]. This method allows the control of the orientation and thickness of the film and has been used by several teams for the growth of MOF thin films on QCM surfaces [159][90].

5.3.1 Synthesis and characterization

The film was prepared in accordance with literature reports of layer-by-layer MOF thin film formation on QCM [93][159]. The QCM was initially soaked in an ethanol solution of 4-mercaptopyridine (10mM) for 24 h, establishing a thiol-based SAM. After this treatment, the QCM was thoroughly washed with ethanol and dried under nitrogen flow. Next, the functionalized QCM was alternately dipped in an aqueous solution of $AgNO_3$ (50mM) and an ethanolic solution of 4-4,bipyridine (50 mM). Between the immersions, the QCM was washed with the corresponding solvent, water or ethanol, respectively, and dried under nitrogen flow. Figure 5-7, shows a schematic illustration of the MOF thin film produced using this method.

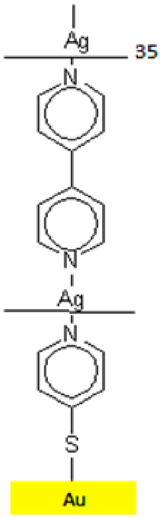

Figure 5-7 Schematic illustration of the MOF thin film on the QCM

The film is developed from a 4-mercaptopyridine SAM which provides chemical attachment to the QCM. The film is expected to grow perpendicularly to the QCM surface, as silver forms almost linear bonds, while adjacent chains are cross-linked, forming a 3-D network [155].

X-ray diffraction analysis of the so-formed thin film revealed that it was too thin to provide a useful XRD pattern. Thicker films were prepared to address this issue. The

LbL process of building MOF thin films is extremely labour intensive, and an automated procedure was developed to produce thicker films. A Successive Ionic Layer Adsorption and Reaction (SILAR) coating system (HO-TH-03S, Holmarc) was used to program immersion cycles in aqueous solution of $AgNO_3$, deionized water to wash away the excess of the metal analyte, ethanolic solution of 4-4,bipyridine and finally ethanol to wash away the excess of the organic analyte. Using this SILAR coating system, thin films of 50, 100 and 150 cycles were produced.

Figure 5-8 presents the XRD patterns of those films, taken using X-rays of a wavelength of 0.154 nm. The 50 cycles film was again too thin to produce a pattern, but it is shown to exemplify the positions of the background gold peaks. The sharp peak at 38 degrees is characteristic of the Au(111) plane and the small peak at 45 degrees corresponds to the Au(200) plane. It may be seen that the patterns produced using the 100 and 150 cycles films are quite similar to each other, suggesting that the structure of the 35 and 50 cycles thin films must be similar to those, though their XRD patterns cannot be observed.

For comparison, an XRD pattern of the bulk crystals reported by Colinas *et al.* [160] is also shown in the top section of Figure 5-8. It can be observed that the patterns of our thin film and of the bulk crystals are quite similar. This suggests that the structure of the thin film is similar to that of the bulk crystals.

By using Bragg's law (Equation 5.1),

$$n\lambda = 2dsin\theta \qquad 5.1$$

where n is an integer, d is the distance between planes in the crystal and θ is the angle of incidence of an x-ray of wavelength λ, the Miller indices h, k and l can be calculated by equation 5.2,

$$\frac{1}{d^2} = \frac{h^2}{a^2} + \frac{k^2}{b^2} + \frac{l^2}{c^2} \qquad 5.2$$

where a, b and c are the unit cell dimensions which for the Ag-4,4'-bipy MOF are given by Yaghi *et al.* as a=9.914 Å, b=34.488 Å and c=12.963 Å [155]. Thus, the peaks of the XRD spectra can be assigned to a corresponding plane, marked by a 3-digit number for *hkl*, as shown in Figure 5-8.

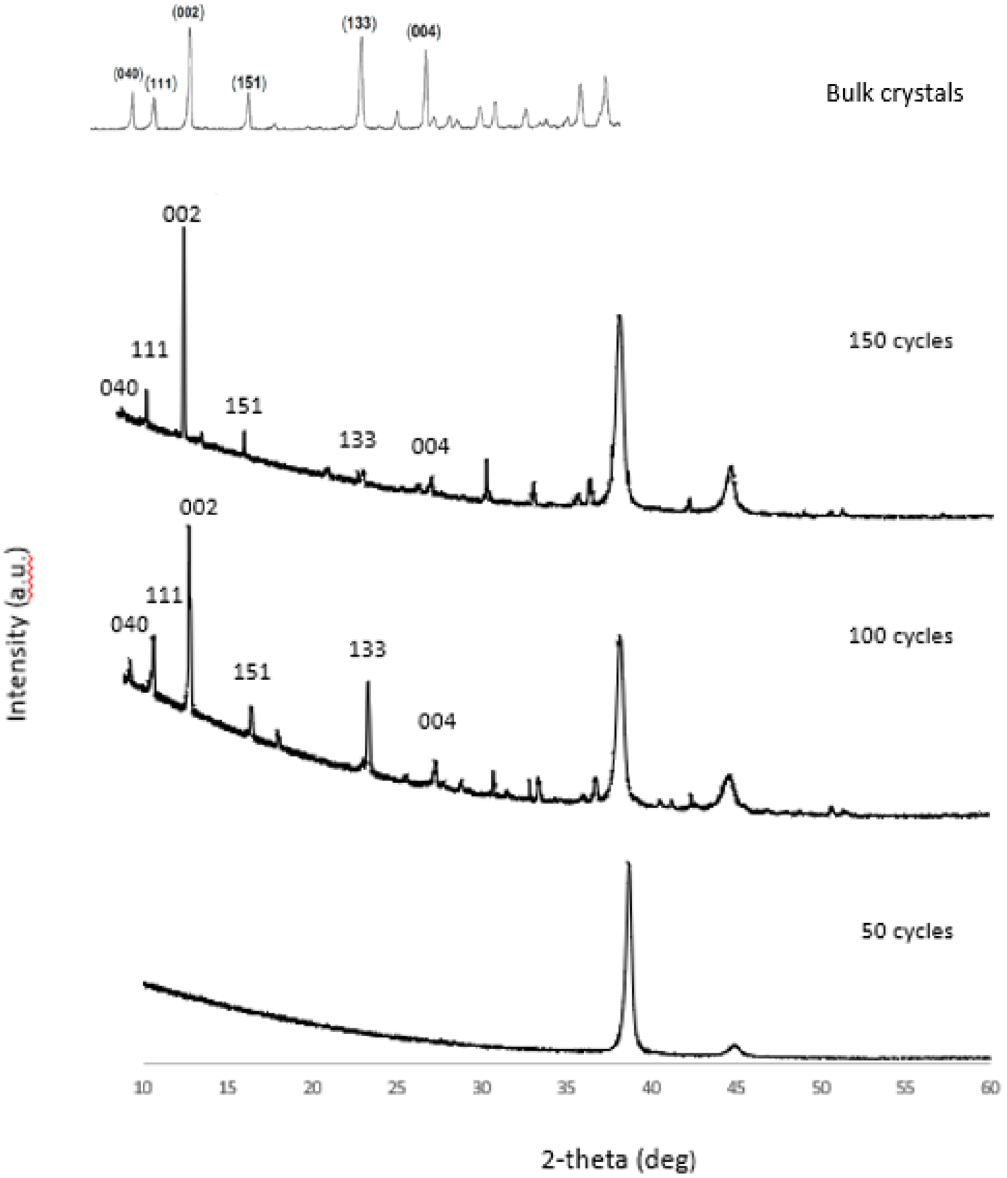

Figure 5-8. XRD patterns for Ag-4,4'-bipyridine Metal organic framework (top: bulk crystal taken from Colinas et al. [160]*, middle top: 150 layers thin film, middle bottom: 100 layers thin film, bottom: 50 layers thin film)*

Figure 5-9 shows the SEM images of the 35-, 50- ,100- and 150-layer MOF films. SEM analysis of the samples was carried out using a JEOL 6010-LV (JEOL (UK) Ltd., Herts, UK) scanning electron microscope (SEM). The examinations were performed at 20 keV using compositional backscatter imaging (BEC) in low vacuum mode, with an instrument resolution ~5 nm. Since the thickness of the films is in the range of a few tens to a few hundreds of nm, the 3-D structure is not quite definite, but it is clear that the surface of every sample is porous, which becomes more evident as the number of layers grows. Therefore, this suggests that, despite the molecular level similarities revealed by XRD, the microscale morphology of the film differs from the spheroidal shape of the bulk crystal. This is possibly due to the tethering of the film on the solid gold surface of the QCM and the layer-by-layer preparation, which restricts the growth of the film to a given orientation which might have implications for the behaviour of the Ag-4,4'-bipyridine MOF in this configuration. In the next section we will consider the adsorption of ReO4- in to the prepared thin films.

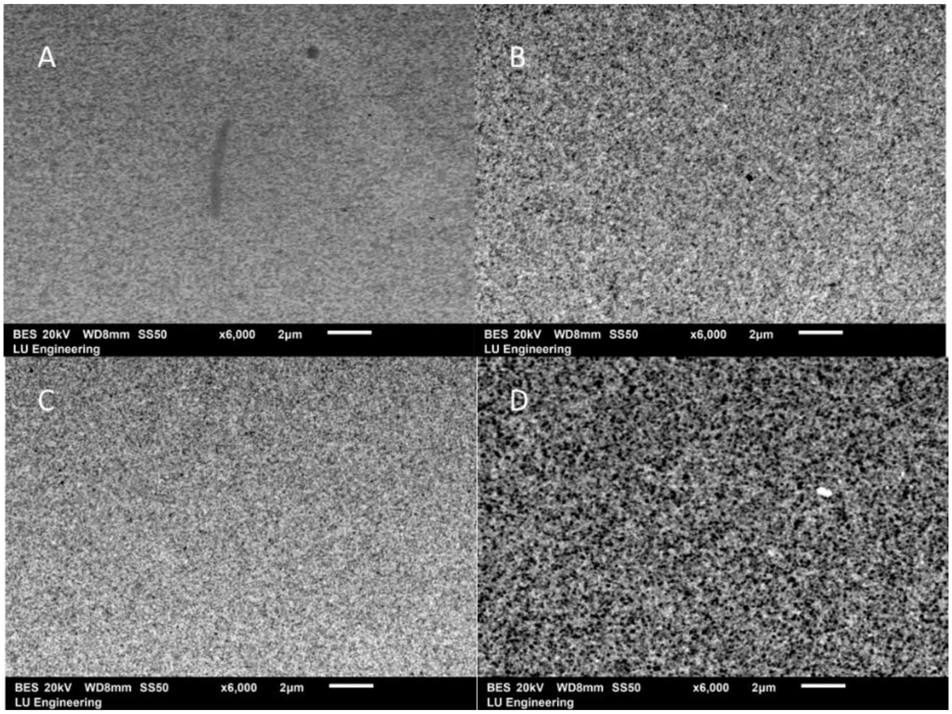

Figure 5-9. SEM images of the A) 35-, B) 50-, C) 100- and D) 150-layer MOF thin film

5.3.2 Experiments with $NaReO_4$

Adsorption experiments were conducted as follows. The coated QCM was mounted on the QSH-dip sensor holder which was then immersed in a beaker containing 50 mL of deionized water, where it was left for several minutes to equilibrate. Small aliquots of an aqueous $NaReO_4$ solution were then titrated into the beaker, while the resonant frequency was monitored.

5.3.2.1 35-layer film

Figure 5-10 shows the change in resonant frequency measured at the QCM coated with a 35-layer thin film exposed to increasing concentrations of $NaReO_4$. The QCM was left to stabilize in pure deionized water (pH=7, room temperature) for over 40 min, before the titrations of $NaReO_4$ started. Each drop in frequency (or step) corresponds to an increase in the concentration of $NaReO_4$ of about 0.9 mmol L^{-1}. It may be seen that as the concentration increases, the total frequency decreases as mass is being adsorbed in the surface of the QCM. However, the rate of the frequency drop, meaning the size of the steps, is decreasing as the concentration increases, due to the gradual saturation of the film.

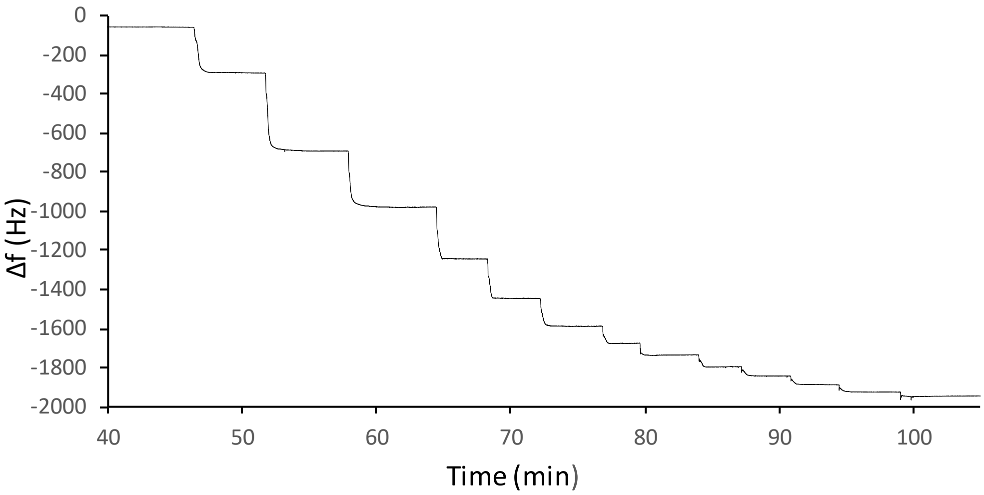

Figure 5-10. Change in frequency in presence of NaReO$_4$ *for the 35 layers MOF thin film. Every drop in frequency correspond to an increase in concentration of NaReO*$_4$ *of about 0.9 mmol dm*$^{-3}$*.*

In contrast to the bulk crystals, adsorption into the thin film appears to be a reversible process. Figure 5.10 shows a chronomassogram for a repeat of the experiment shown in figure 5.9, where at t=71 minutes the QCM is removed from the test solution and placed in a beaker containing fresh deionized water. At this point, the frequency increases significantly which is indicative of a large mass loss, most likely due to the removal of perrhenate ions from the thin film. The reasons for this behaviour will be discussed later, but suggest that a sensor built on this template would be reusable.

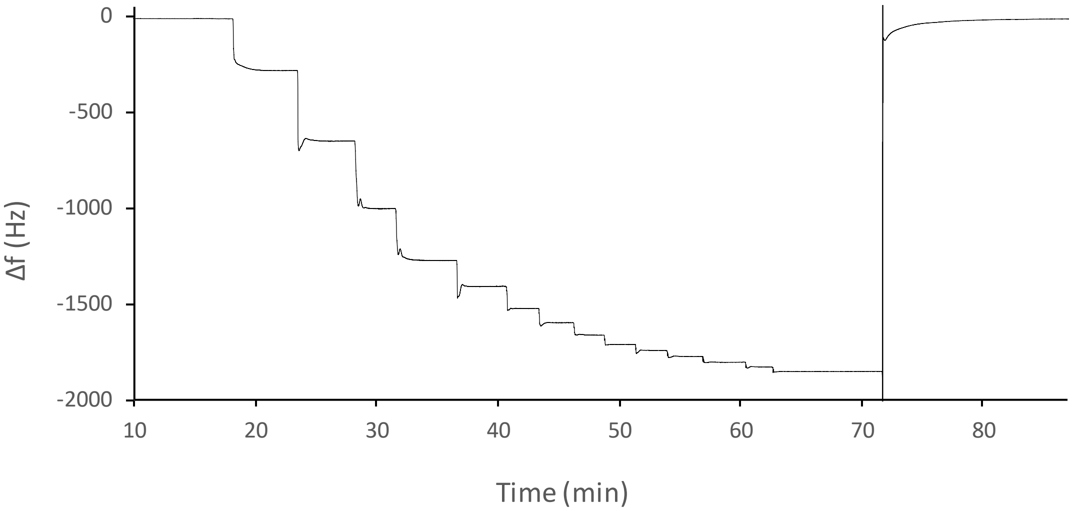

Figure 5-11. Decrease in Δf in the presence of NaReO₄ and then increase in Δf at min 71 when removed from solution for the 35 layers MOF thin film coated QCM. The adsorbate was removed from the film when the QCM was placed in clean deionised water and the frequency went back to the starting value.

The reusability of the thin film enabled us to repeat the experiment of figures 5.9 and 5.10 to ensure the reproducibility of these results. Figure 5-12 shows the change in frequency as a function of the perrhenate ion concentration obtained from 6 different adsorption experiments including those shown in figures 5.9 and 5.10. The QCM crystal was thoroughly rinsed and dried between experiments.

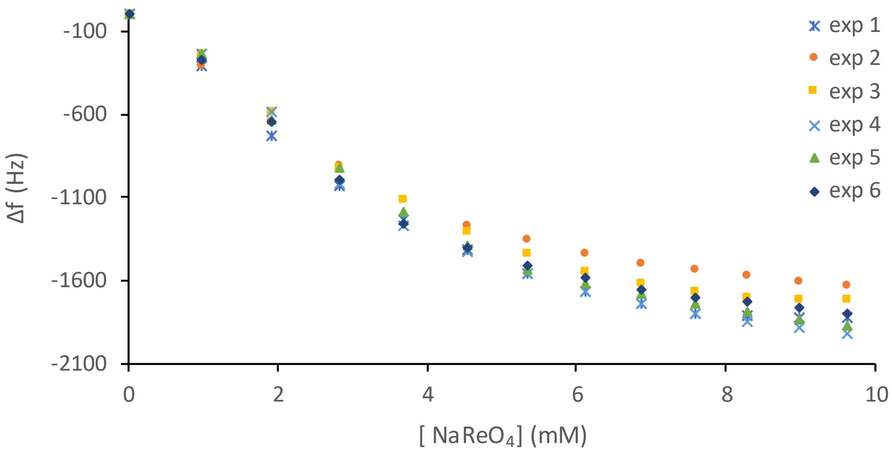

Figure 5-12. Change in resonant frequency plotted against the change in total concentration of $NaReO_4$ for the 35 cycles MOF thin film coated QCM, for 6 different experiments with the same crystal.

Figure 5-13 shows the data of figure 5.11 recast as mass of adsorbed perrhenate vs bulk concentration, this was computed using Saurbrey's equation and a value of the mass sensitivity factor C_f= 56.81 Hz cm^2 μg^{-1}, as it was calculated in Chapter 2.

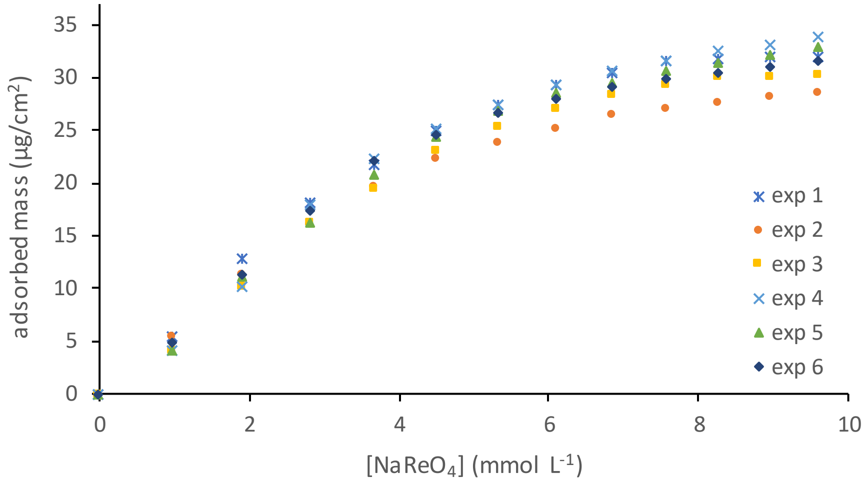

Figure 5-13. Adsorbed mass per surface area plotted as a function of NaReO4 concentration for the 35 layers MOF thin film coated QCM, for 6 different experiments with the same crystal.

As may be seen in Figure 5-13, the absorbed mass increases rapidly at low bulk concentrations, reaching a plateau of about 31 μg/cm^2 for concentrations higher than 9 mmol L^{-1}. This suggests the gradual saturation of the thin film, as mentioned earlier.

5.3.2.2 50-layer film

Figure 5-14, shows the change in frequency of a 50-layer MOF thin film-modified QCM when exposed to increasing concentrations of NaReO$_4$. The experiments were conducted as for the 35-layer crystal, and each titration corresponds to an increase in the concentration of NaReO$_4$ of about 0.9 mM.

It may be seen from figure 5.13 that, in the first 5 minutes of the experiment, the frequency increases up to 230 Hz, which may be explained by the removal of impurities from the thin film. Between t=5mins and t=22mins the frequency signal has stabilized somewhat but is less consistent that what was observed with the 35-layer QCM (Figure 5-10).

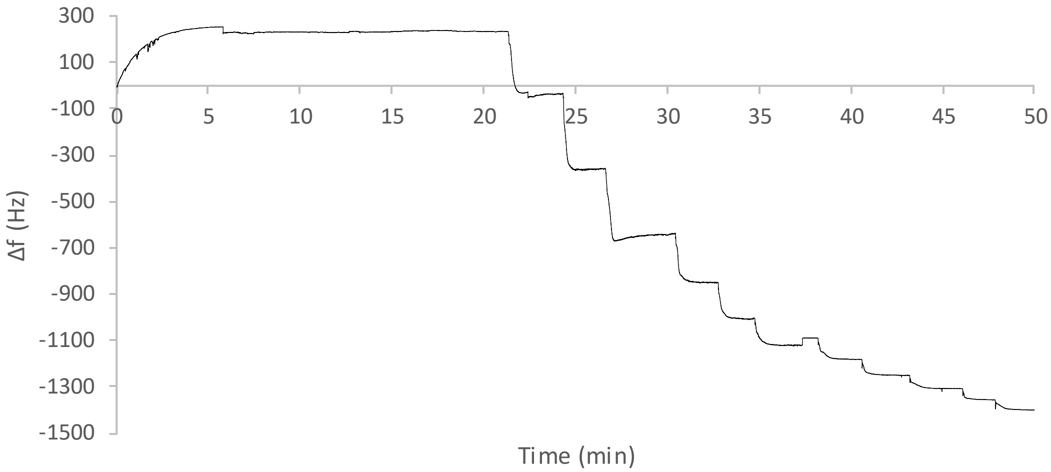

Figure 5-14. Change in frequency in presence of $NaReO_4$ for the 50 layers MOF thin film. At first, the QCM was left to equilibrate in 50 mL of DI water at room temperature. The increase in frequency in the beginning probably corresponds to impurities being removed from the film in the solution. Every drop in frequency correspond to an addition of about 0.9 mM $NaReO_4$ in the solution.

The data of figure 5.13 and that of three additional repeats were treated using the same procedure as the data from the 35-layer crystal to show the frequency change as a function of the bulk concentration in $NaReO_4$ for the 50 layers MOF thin film and is presented in Figure 5-15. As may be seen, there are significant deviations in the results at low and high concentrations, while in the intermediate range (4-6 mmol L^{-1}) there is better agreement.

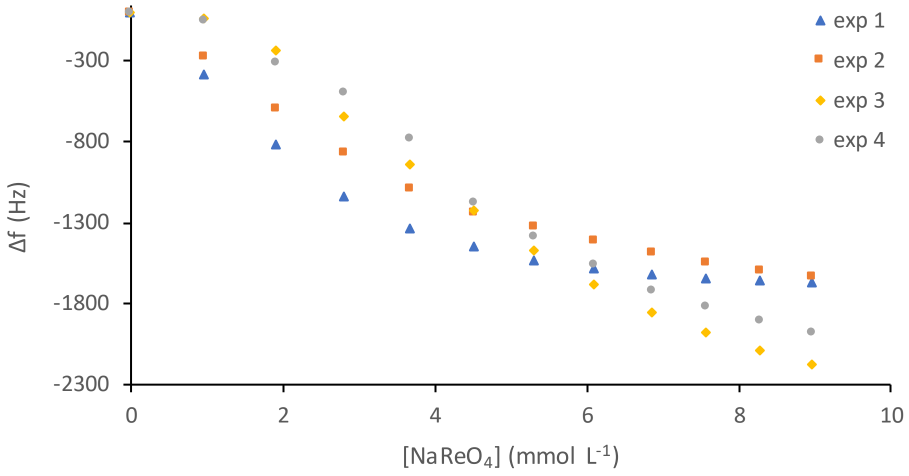

Figure 5-15. Change in resonant frequency plotted against the change in total concentration of $NaReO_4$ for the 50 cycles MOF thin film coated QCM for 4 different adsorption experiments.

Finally, after converting the change in frequency to change of mass through Sauerbrey's equation as demonstrated earlier, the relation between adsorbed mass per surface area and the concentration of $NaReO_4$ is obtained, as shown in Figure 5-16

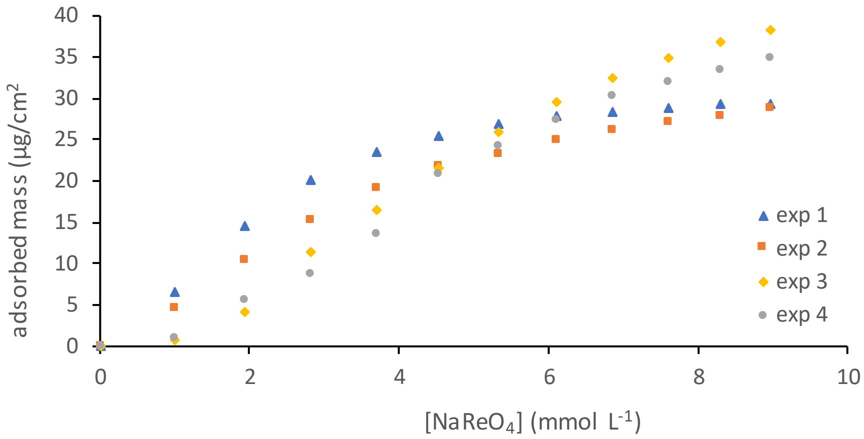

Figure 5-16 . Adsorbed mass per surface area plotted as a function of NaReO4 concentration for the 50 layers MOF thin film coated QCM, for 4 different experiments with the same crystal.

Again in this case, the rate at which mass is being adsorbed in the film starts to decrease at a concentration of 4 mM, finally reaching a slightly maximum plateau of 33 μg/cm^2, as expected, since this is a thicker film hence having greater capacity. However, it is observed that the differences between the experimental data are quite bigger than the ones demonstrated in Figure 5-13 for the 35 layers film, suggesting that the thinner film could provide more accurate results.

Having demonstrated satisfying reproducibility for the adsorption of $NaReO_4$, let us now proceed with the presentation of the results of adsorption experiments conducted with interferences that are abundantly found in groundwater. The below experiments serve as a selectivity test for our Ag-4-4-bipyridine MOF thin film.

5.3.3 Experiments with NaCl

The typical proximity of nuclear sites to large bodies of water including seas and oceans encourages us to consider the effect of commonly encountered ions on the behaviour of the sensor. One of the most commonly encountered anions in sites' ground water is Cl^-. On the Sellafield site, its reported maximum concentration is 3190 mg/L and average concentration is 79.7 mg/L in 2016 [4]. Hence, it was of great interest to determine the response of the Ag-4-4-bipyridine MOF thin film in the presence of Cl^-. The NaCl salt was used so that the cation in presence is the same and to avoid any additional interferences.

5.3.3.1 35-layer film

The experiments were conducted as described previously. The QCM coated with the 35 layers MOF thin film was mounted in the holder, left to rest in 50 mL deionized water and then titrations of NaCl solution, increasing the concentration by 0.9 mM each time, took place. The raw data of this experiment is presented in Figure 5-17. As with $NaReO_4$, this was identified to be a reversible process and the experiments were repeated for 4 times, rinsing the QCM thoroughly with Deionised water between each run.

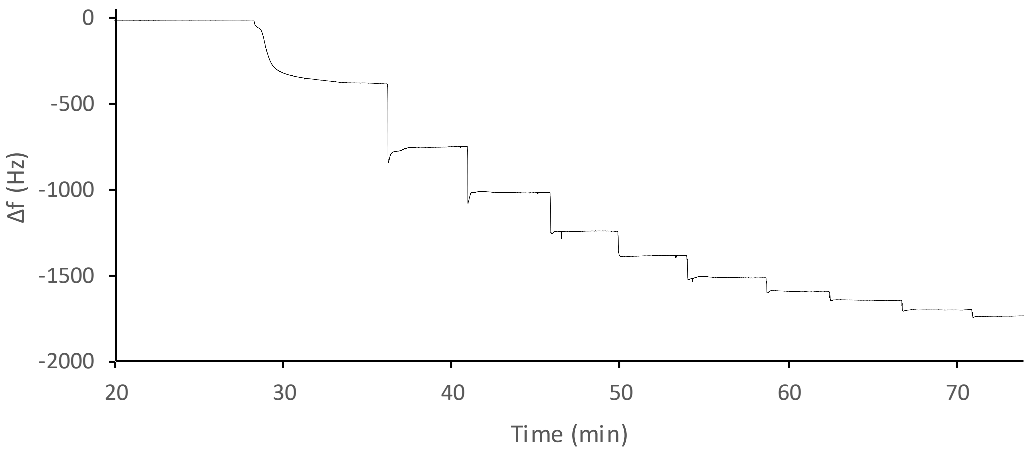

Figure 5-17. Change in frequency in presence of NaCl for the 35 layers MOF thin film. Every drop in frequency correspond to an addition of about 0.9 mM NaCl in the solution.

Working like previously, the relation between the change in frequency and the concentration was acquired from the 4 different adsorption experiments, as shown in Figure 5-18. The really small difference between the sets of data provides proof of quite good reproducibility and accuracy.

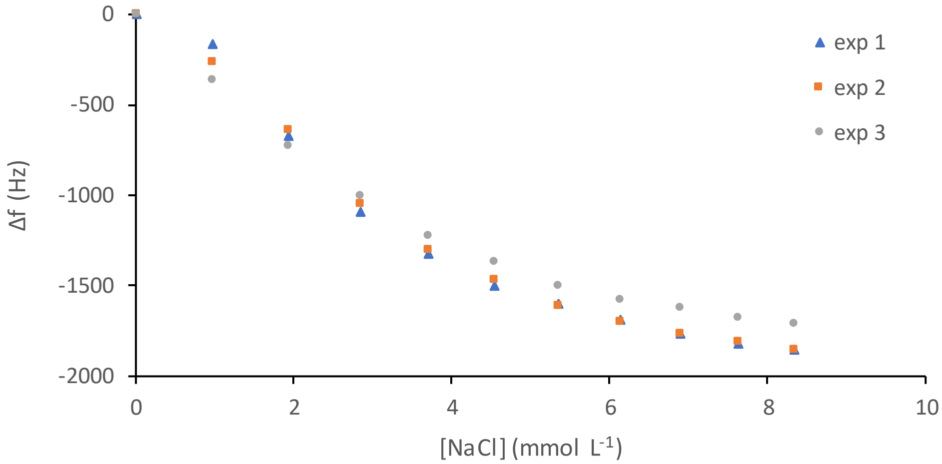

Figure 5-18. Change in resonant frequency plotted against the change in total concentration of NaCl for the 35 cycles MOF thin film coated QCM, for 3 different experiments with the same crystal.

Finally, using Sauerbrey's equation, the change in frequency is converted to change in mass per surface area. In Figure 5-19, the relation between the latter and the NaCl concentration is shown. We can see that the shape of the curve and the maximum value of the plateau are quite similar to that of $NaReO_4$, but this will be discussed later.

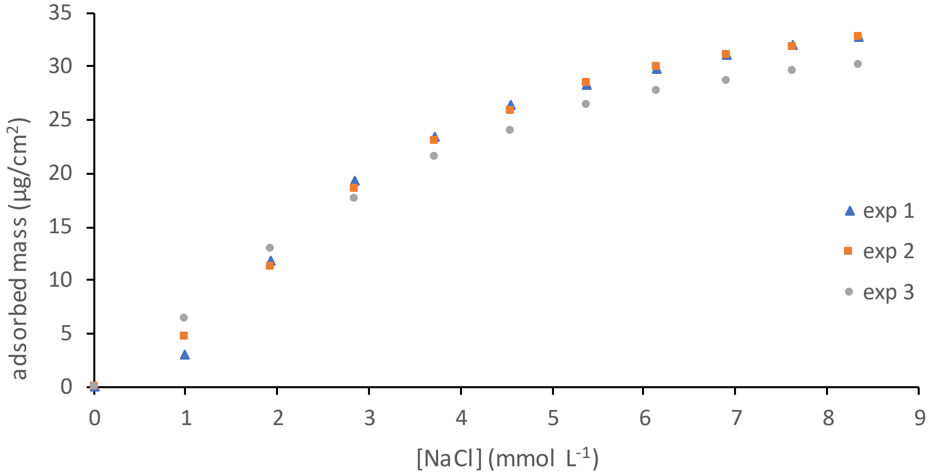

Figure 5-19. Adsorbed mass per surface area plotted as a function of NaCl concentration for the 35 layers MOF thin film coated QCM, for 3 different experiments with the same crystal.

5.3.3.2 50-layer film

Continuing with the results of the 50 layers MOF thin film with NaCl, the raw data of the QCM response is presented in Figure 5-20. What can be observed from that graph is that the time it takes the QCM to stabilize its frequency is slightly longer than this of the 35 layers thin film. While in Figure 5-17, showing the response of the 35 layers film, the decrease of frequency in every addition of NaCl is steep, in Figure 5-20 the decrease is more gradual. This fact could be associated with the thickness of the film, meaning that the adsorption could be a slower process when the film is thicker.

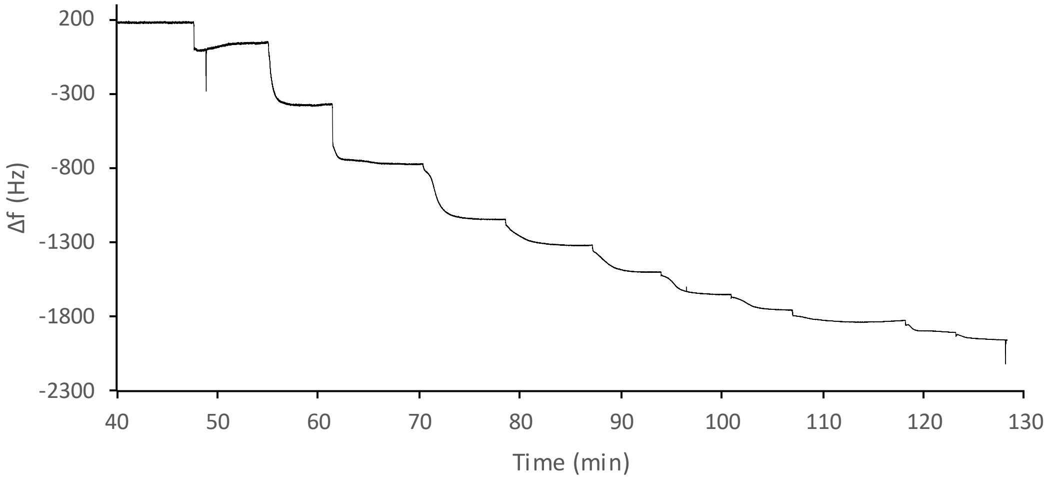

Figure 5-20. Change in frequency in presence of NaCl for the 50 layers MOF thin film. Every drop in frequency correspond to an addition of about 0.9 mM NaCl in the solution.

Working in the same fashion and after implementing Sauerbrey's equation, the adsorbed mass per surface area against the concentration of NaCl for the 50 layers MOF thin film is plotted in Figure 5-21. This is a product of only one set of data because, for reasons not clear yet, more adsorption experiments did not yield any results. Although this does not produce the statistical significance of the previous experiments, it is clear that it follows the same trend, meaning that there is little adsorption in low concentrations, high adsorption at the range of 2-4 mM, while the rate of adsorption gradually decreases in concentrations higher than 4 mM, finally reaching a plateau of 37 μg/cm^2 in high concentrations, which is higher than that of the 35 layers film, where the maximum adsorption seems to be around 32 μg/cm^2. The latter was expected, since the film is thicker it has higher adsorption capacity.

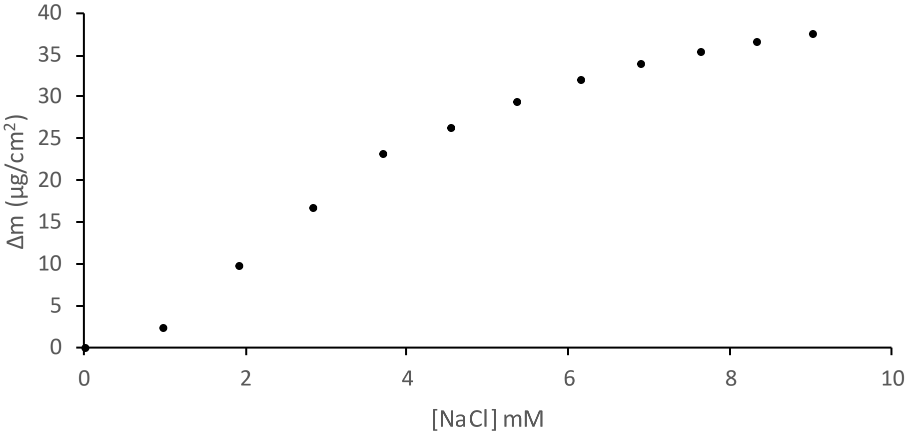

Figure 5-21. Adsorbed mass per surface area plotted as a function of NaCl concentration for the 50 layers MOF thin film coated QCM.

5.3.4 Experiments with Na_2SO_4

Another important interference in groundwater is the SO_4^{2-} anion, this is because as well as its relatively high concentration in groudwater, with a maximum of 384 mg/L and an average of 28.2 mg/L on the Sellafield site in 2016 [4], its tetrahedral structure mimics that of ReO_4^-, which forms the main recognition pattern used by the Ag-4,4'-bipyridine MOF to selectively adsorb ions . Figure 5-22 shows the response of the 35 layers thin film coated QCM in the presence of Na_2SO_4 . The experiments we conducted as previously, meaning that the QC was mounted in the holder, dipped in 50 mL of deionized water and then solution of Na_2SO_4, in 0.9 mM titrations, was added. This took place in room temperature and pH 7.

5.3.4.1 35-layer film

As can be seen, the sensor responds in a similar way as it did in the presence of $NaReO_4$ and NaCl. Every step corresponds to a titration of 0.9 mM of Na_2SO_4 in the solution and as the concentration increases, the size of the step decreases. As explained earlier, this is indicative of the progressive saturation of the film. As previously highlighted, this process is reversible, and the experiment was repeated 3 times.

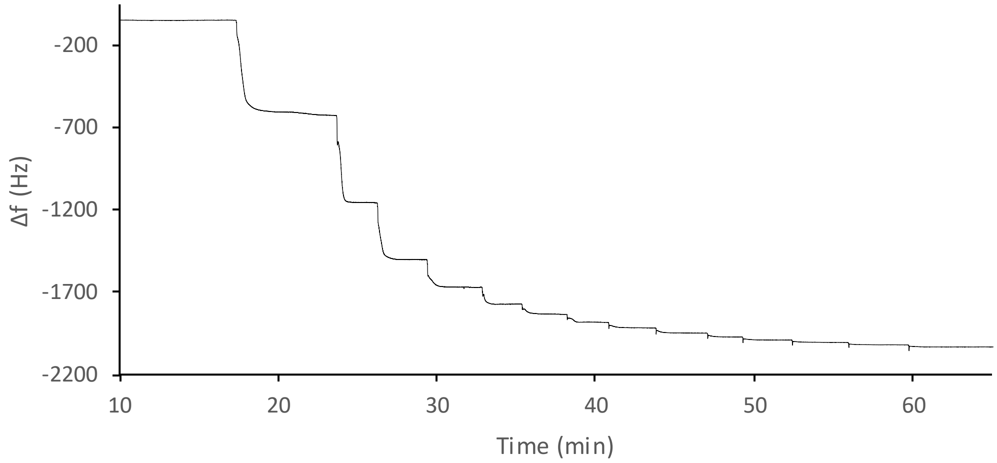

Figure 5-22. Change in frequency in presence of Na_2SO_4 *for the 35 layers MOF thin film. Every drop in frequency correspond to an addition of about 0.9 mM* Na_2SO_4 *in the solution.*

In Figure 5-23, the relation between change in frequency and the Na_2SO_4 concentration for 3 different experiments is shown. The data suggests good reproducibility and accuracy, as the results of the experiments are quite similar.

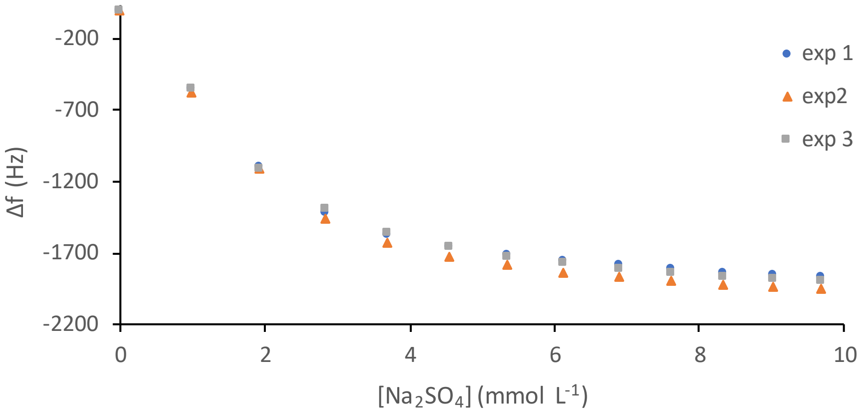

Figure 5-23 Change in resonant frequency plotted against the change in total concentration of Na$_2$SO$_4$ for the 35 layers MOF thin film coated QCM for 3 different adsorption experiments with the same crystal.

After combining the 3 experiments and implementing Sauerbrey's equation, we finally get the adsorbed mass pre surface area against the concentration of Na$_2$SO$_4$, as shown in Figure 5-24. The data seems to follow the same trend with that of NaReO$_4$ and NaCl, reaching a remarkably close plateau value of 33 µg/cm^2.

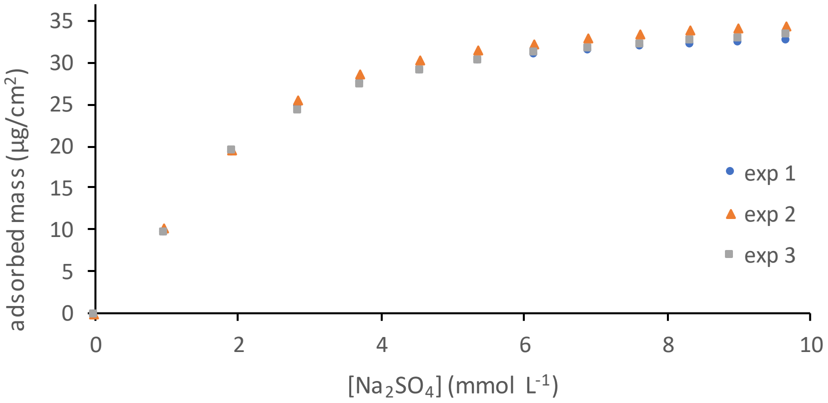

Figure 5-24. Adsorbed mass per surface area plotted as a function of Na$_2$SO$_4$ concentration for the 35 layers MOF thin film coated QCM, for 3 different adsorption experiments with the same thin film.

5.3.4.2 50-layer film

Let us, now, proceed with the results with the 50 layers MOF thin film in the presence of Na_2SO_4, which are presented in Figure 5-25. We were able to repeat the experiment 3 times, all of them were conducted in the same way, as explained earlier for the 35 layers film, and in room temperature and pH 7.

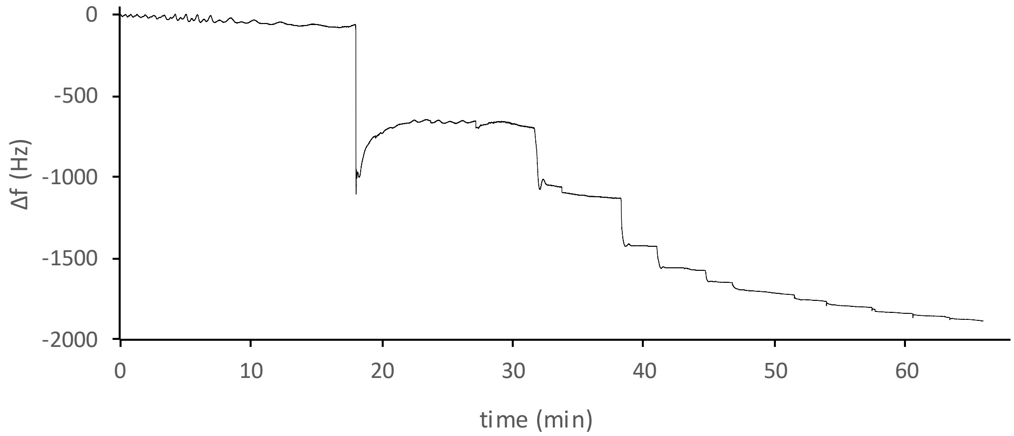

Figure 5-25. Change in frequency in presence of Na_2SO_4 for the 50 layers MOF thin film. Every drop in frequency correspond to an addition of about 0.9 mM Na_2SO_4 in the solution.

Figure 5-26 shows the change in frequency against the concentration of Na_2SO_4 for 3 repeats of this experiment. It may be seen that while the general trend is identical to previous plots, the frequency measurements are much less reproducible than for the 35-layer experiment. This was also observed for the $NaReO_4$ experiments, where the results from the 35 layers film were more reproducible than the those of the 50 layers film.

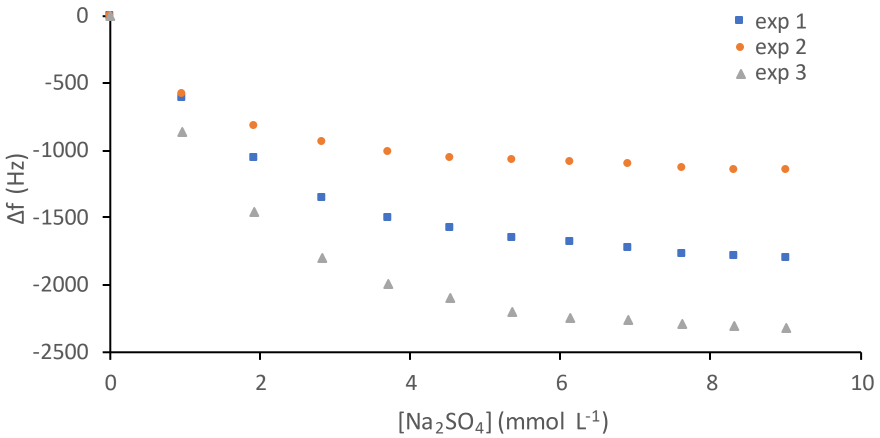

Figure 5-26 Change in resonant frequency plotted against the change in total concentration of Na_2SO_4 for the 50 layers MOF thin film coated QCM for 3 different adsorption experiments with the same film.

After converting the change in frequency to change in mass, we get the adsorption diagram in Figure 5-27, which shows the adsorbed mass per surface area of the 50 layers film against the concentration of Na_2SO_4. Although the difference between the experiments is significantly bigger than those of the 35 layers thin film, the data points follow the same trend, meaning that in concentrations higher than 2 mM, the rate of adsorption decreases until it reaches a maximum plateau of an average 31 μg/cm^2, in concentrations higher than 8 mM of Na_aSO_4.

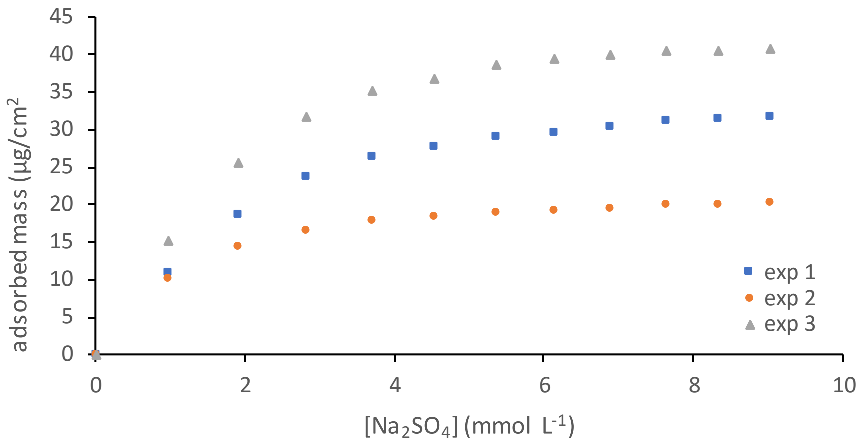

Figure 5-27. Adsorbed mass per surface area plotted as a function of Na_2SO_4 concentration for the 50 layers MOF thin film coated QCM, for 3 different adsorption experiments with the same thin film.

5.3.5 Experiments with Na_2CO_3

The last interference that was studied was the CO_3^{-2} ion. Given the fact that the sensor is not selective, since in the presence of NaCl and Na_2SO_4 it responded in a very similar way as it did with $NaReO_4$, it was decided to work towards understanding the mechanism of the adsorption, rather than keep testing the selectivity to anions found in groundwater. Although the carbonate anion is not abundant in groundwater (the bicarbonate HCO_3^- is one of the most abundant anions in groundwater instead), it was used because it holds some parameters that needed to be tested, such as its very similar geometry to NO_3^-, which is the counter anion of the Ag-4-4-bipyridine MOF, and its charge, which is the same as SO_4^{-2}. The sodium salt was used once again, in order to avoid any different cation interaction.

5.3.5.1 35-layer film

So, in Figure 5-28, the change in frequency for the 35 layers MOF thin film coated QCM in the presence of Na_2CO_3. As explained earlier, every step corresponds to an addition of 0.9 mM of Na_2CO_3 in the solution in which the QCM was dipped. Similarly to the previous experiments, the steps, meaning the decrease in frequency with every addition, is getting smaller, eventually approaching zero.

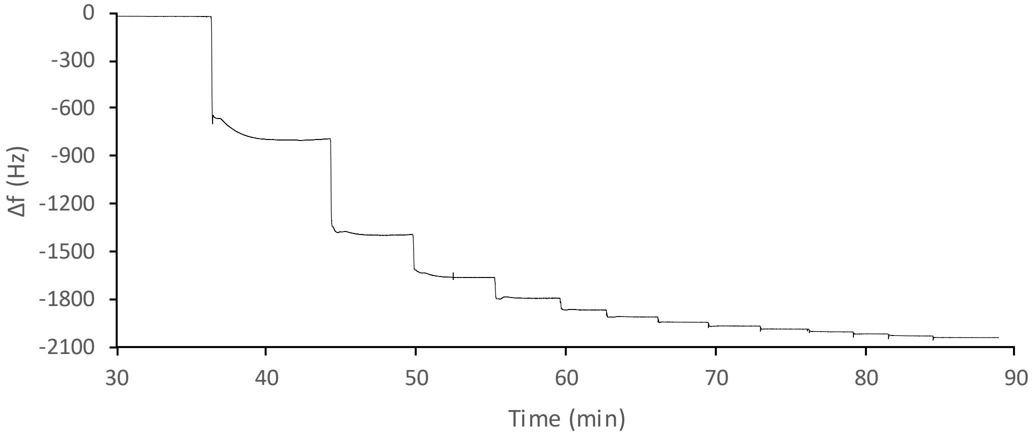

Figure 5-28. Change in frequency in presence of Na_2CO_3 for the 35 layers MOF thin film. Every drop in frequency correspond to an addition of about 0.9 mM Na_2CO_3 in the solution.

This experiment was repeated one more time and the results of both are presented in Figure 5-29, where the change of frequency is related with the concentration of Na_2CO_3, for the 35 layers film. As we can see, the two experiments have provided satisfyingly close results, which in fact, are also quite similar to those of the Na_2SO_4 experiments.

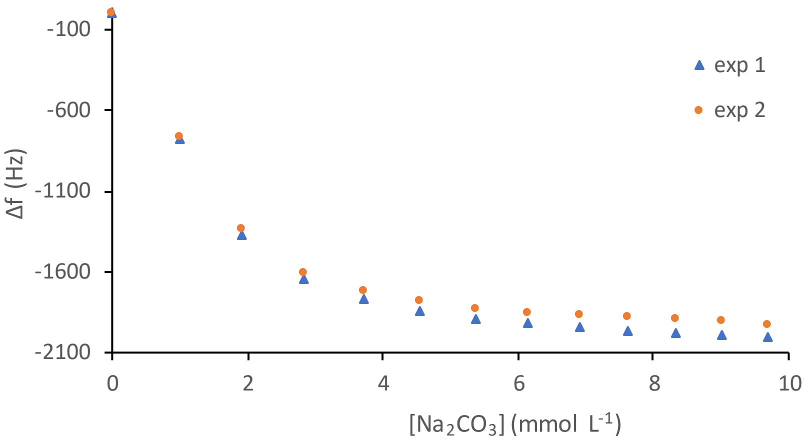

Figure 5-29. Change in resonant frequency plotted against the total concentration of Na_2CO_3 for the35 layers MOF thin film coated QCM for 2 different adsorption experiments.

Implementation of Sauerbrey's equation provides us with the final adsorption diagram, as presented in Figure 5-30. As it was explained earlier, high rate of adsorption is observed at low concentrations, while saturation of the film is reached quite soon, compared to the previous experiments with the other analytes, at concentrations above 6 mM, reaching a maximum adsorption of 35 μg/cm^2.

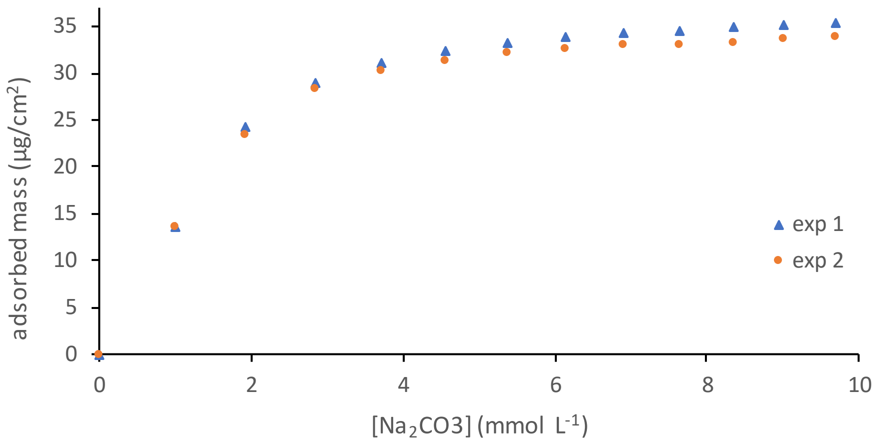

Figure 5-30. Adsorbed mass per surface area plotted as a function of Na_2CO_3 concentration for the 35 layers MOF thin film coated QCM. The error bars are derived from the analysis of 2 different adsorption experiments with the same thin film.

5.3.5.2 50-layer film

Finally, the last results to be presented are those of the 50 layers MOF thin film in the presence of Na_2CO_3, the raw QCM data of which is shown in Figure 5-31.

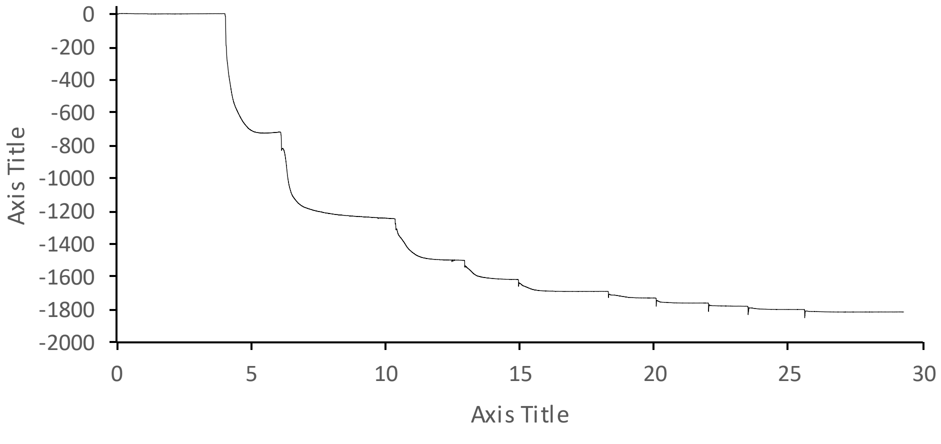

Figure 5-31. Change in frequency in presence of Na_2CO_3 for the 50 layers MOF thin film. Every drop in frequency correspond to an addition of about 0.9 mM Na_2CO_3 in the solution.

Like in the previous experiments, every drop in frequency in the above graph corresponds to an increase of 0.9 mM in the concentration of Na_2CO_3. So, working in a similar fashion, we get the adsorption diagram showing the connection between the adsorbed mass per surface area and the concentration of Na_2CO_3, in Figure 5-32. As it also happened with NaCl experiment with the 50 layers film, we were not able to reproduce this data. However, it seems that it follows the same trend, meaning that there is high adsorption in low concentrations, the rate of which decreases after 2 mM, finally reaching a plateau in concentrations higher than 6 mM.

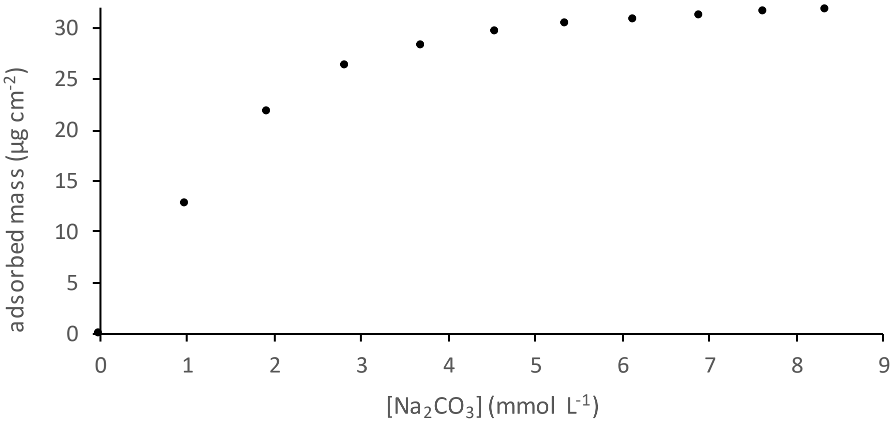

Figure 5-32. Adsorbed mass per surface area plotted as a function of Na_2CO_3 concentration for the 50 layers MOF thin film coated QCM.

5.4 Conclusion

The QCM surface was successfully coated with a thin film of the Ag-4,4-bipyridine metal-organic framework, which has been reported for extensive perrhenate take up. The film was built layer-by-layer on a self-assembled monolayer of 4-mercaptopridine on the gold electrode of the QCM and was characterized with XRD and SEM. The XRD analysis showed that the molecular structure of the thin film is similar to that of the bulk crystals. However, the SEM analysis suggests that the morphology of the film in the microscale is different than that of the bulk crystals, probably because of the tethering of the film on the gold surface of the QCM.

The response of 35 layers and 50 layers films in the presence of $NaReO_4$ as well as of interferents such as NaCl, Na_2SO_4 and Na_2CO_3 was tested. It was shown that the MOF responds in a different way in the form of a thin film than in the form of bulk crystals, since the adsorption was reversible in the case of the film. Also, it appears that the thin film is not very selective towards perrhenate, as both the 35 layers and 50 layers films respond similarly to all the analytes that they were tested with. However, there were some serious reproducibility issues with the 50 layers film, while the results of the 35 layers film proved to be more reproducible and with much smaller deviations. The next chapter considers the modeling of the data produced with all the analytes used, to adsorption isotherms, such as Langmuir, Freundlich and Sips to understand the mechanism behind the adsorption in the Ag-4-4-bipyridine MOF.

CHAPTER 6

6 Modeling of the adsorption of anions onto the Ag-4-4'-bipyridine thin film

After presenting the results of the adsorption experiments with the Ag-4-4'-bipyridine thin film, let us now consider the modelling this experimental data by well-understood adsorption isotherms, along with what this might reveal about the adsorption process.

Adsorption isotherms are mathematical expressions describing the retention phenomena of a fluid phase adsorbate onto a solid-state medium, under a set of well-defined conditions. The physicochemical parameters contained within the mathematical expressions of the models could provide an insight into the adsorption mechanism and other properties, such as the degree of affinity of the adsorbents [161]. The adsorption isotherms that will be used in this work are the Langmuir isotherm [162], the Freundlich isotherm [163] and the Sips isotherm [164]. While these models have been applied mostly in gas-solid interfaces, lately they have also been used in ionic environments for anion and cation adsorption [165], [166].

6.1 Adsorption isotherms

6.1.1 Langmuir isotherm

In the Langmuir model, the solid is assumed to have limited adsorption capacity, as the concentration of the adsorbent increases. The adsorption is assumed to occur in a monolayer in definite localized sites on the surface of the adsorbate that are identical and equivalent. Thus, graphically it is characterized by a plateau and an equilibrium saturation point, where once a site is occupied, there is no further adsorption. The mathematical expression of the Langmuir isotherm is

$$m = m_{\infty}\frac{kC}{1+kC} \qquad 6.1$$

where *m* is the actual adsorbed mass, *m*∞ is the theoretical adsorbed mass in infinite concentration, *k* is the adsorption affinity and *C* is the concentration of the adsorbent in the solution. In order to calculate the parameters, its linear form can be used as

$$\frac{m}{C} = m_{\infty}k - km \qquad 6.2$$

where a plot showing m/C vs. m provides a straight line of slope equal to -*k* and intercept *m*∞*k* [167].

6.1.2 Freundlich isotherm

The Freundlich isotherm is an empirical model that is not restricted to the formation of a monolayer can be applied to multilayer adsorption. In this perspective, the amount adsorbed is the summation of adsorption on all sites and it does not lead to a plateau, which limits its physical meaning to low concentrations. The mathematical expression of the Freundlich isotherm is

$$m = kC^n \qquad 6.3$$

where, as previously, *m* is the actual mass adsorbed, *k* is the adsorption affinity, *C* is the concentration of the adsorbent and *n* is a dimensionless constant. The linear form, by which the parameters can be calculated is

$$log\, m = n\, log\, C + log\, k \qquad 6.4$$

A plot of log*m* vs. log*C* provides a straight line of slope *n* that intercepts y-axis at log*k* [167].

6.1.3 Sips isotherm

Finally, the Sips isotherm consists of a combination of the Langmuir and Freundlich isotherms, which predicts the adsorption in heterogeneous systems while avoiding the limitation of the low adsorbate concentration in the Freundlich model. At low adsorbate concentrations the Sips isotherm reduces to the Freundlich isotherm predicting multilayer adsorption, while at high concentrations it approaches the Langmuir isotherm, predicting monolayer adsorption in a similar manner. The mathematical form of the Sips isotherm is

$$m = m_{\infty} \frac{kC^n}{1 + kC^n} \tag{6.5}$$

where m is the adsorbed mass, m_{∞} is the theoretical maximum adsorbed mass in infinite concentration, k is the adsorption affinity, C is the adsorbate concentration in the solution and n is a dimensionless constant. In order to obtain these parameters from the experimental results, the Sips equation can be expressed in a linear form as

$$ln \frac{m}{m_{\infty} - m} = n\, ln\, C \quad + ln\, k \tag{6.6}$$

m_{∞} is iteratively found to obtain a linear relation between $\ln C$ (as x-axis) and $\ln \frac{m}{m_{\infty} - m}$ (as y-axis), while n is determined by the slope and k by the interception point [168].

The above procedures for the Langmuir, Freundlich and Sips isotherms will be followed for all the experimental data presented in Chapter 5, in the pursuit of the model that best describes the adsorption mechanism of ReO_4^- onto the Ag-4-4'-bipyridine thin film.

6.2 Modeling of the $NaReO_4$ adsorption data

6.2.1 Langmuir fit

Experimental data of the adsorption of $NaReO_4$ with the 35 layers film were presented in section 5.3.2. Figure 6-1 shows that data recast as the linear form of the Langmuir isotherm (equation 6.2).

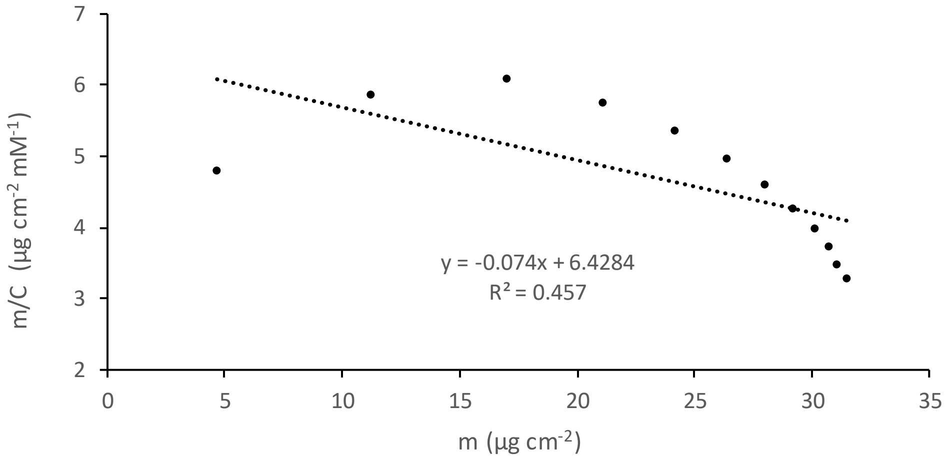

Figure 6-1. Linear form of the Langmuir isotherm for the adsorption of $NaReO_4$ into the 35 layer Ag-4-4-bipyridine MOF thin film, derived from the experimental data.

Through the best fitted line, the Langmuir parameters are calculated as $k = 0.074\ mM^{-1}$ and $m_\infty = 86.8\ \mu g/cm^2$. It is clear from figure 6.1, with its regression coefficient of 0.457, that the Langmuir isotherm does not accurately describe the adsorption process between ReO4- and Ag-4,4'-bipyridine. However, for completeness of analysis, the experimental data and the Langmuir fit, calculated through Equation 6.1, are shown in Figure 6-2. There seems to be a fairly big deviation of the model from the experimental data especially in concentrations higher than 8 mM, which can be explained by the big difference between the experimental (32 µg/cm^2) and theoretical (86.8 µg/cm^2) maximum adsorbed mass per surface area. This comparison leads us to the conclusion that the Langmuir model does not describe the $NaReO_4$ adsorption data.

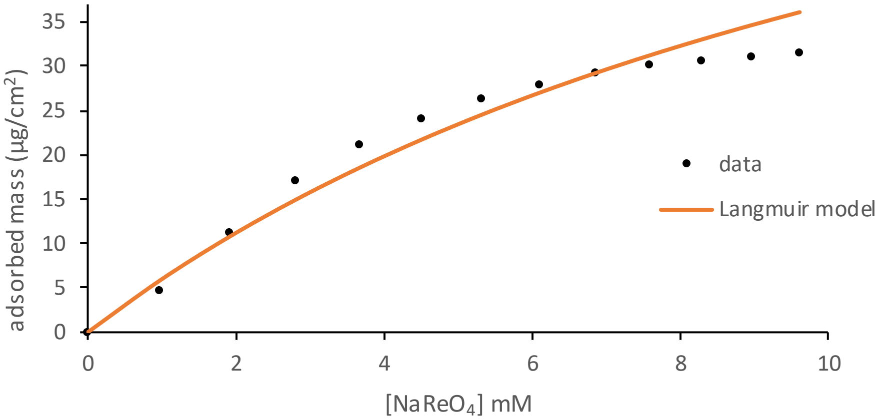

Figure 6-2. Comparison between the experimental data of the $NaReO_4$ adsorption into the 35 layers Ag-4-4-bipyridine film shown with the black dots and the Langmuir model shown with the orange straight line.

6.2.2 Freundlich fit

Continuing, the same data is presented according to the linear form of the Freundlich isotherm (Equation 6.4), as shown in Figure 6-3. The fit is reasonably good (R^2=0.931) with the parameters being calculated as $n = 0.789$ and $k = 6.33$ *µg/mM.*), however it may be seen that there is a marked curvature in the experimental data that is not replicated in the model.

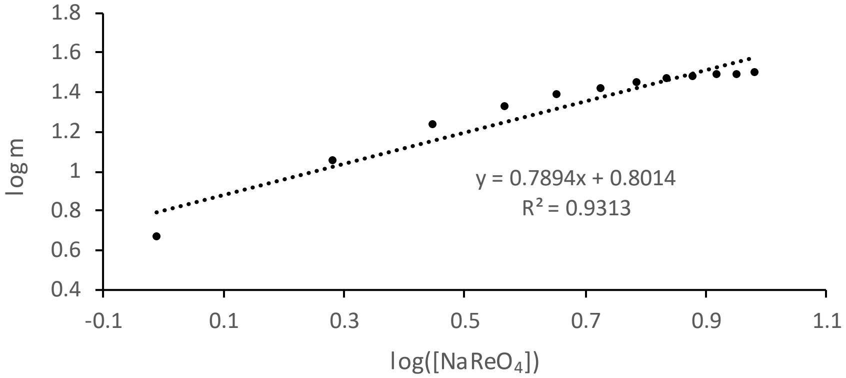

Figure 6-3. Linear form of the Freundlich isotherm for the adsorption of NaReO4 into the 35 layer Ag-4-4-bipyridine MOF thin film, derived from the experimental data.

Implementing those parameters into Equation 6.3 provide the Freundlich fit, presented alongside the experimental data in Figure 6-4. As with the Langmuir model, the Freundlich model seems to deviate significantly from the experimental data in the high concentration range, after 8 mM. While the experimental data are approaching a plateau at around 32 µg/cm^2 at concentrations higher than 8 mM, the Freundlich model seems to continue increasing indefinitely.

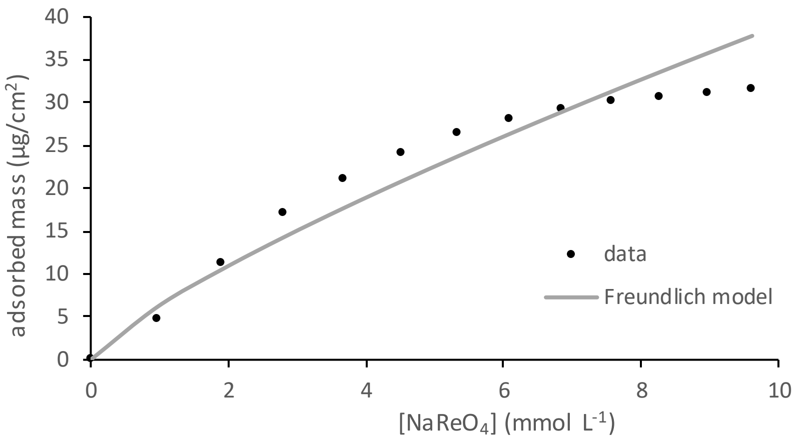

Figure 6-4. Comparison between the experimental data of the $NaReO_4$ *adsorption into the 35 layers Ag-4-4-bipyridine film shown with the black dots and the Freundlich model shown with the grey straight line.*

6.2.3 Sips fit

Finally, the combination of the Langmuir and Freundlich isotherms, namely the Sips isotherm is fitted to the experimental data. The first step is again the calculation of the Sips parameters through the linear form of the Sips model from Equation 6.6, which is shown in Figure 6-5. This results in a very good linear fit ($R^2 = 0.997$). The maximum adsorbed mass in infinite concentration was calculated iteratively as $m_\infty = 34.8\ \mu g/cm^2$, in order to obtain the linear fit which provided the other two parameters as $k = 0.136\ mM^{-1}$ and $n = 1.78$.

The isotherms analysis presented here were carried out for a single data set in order to identify the model that best describes the adsorption of ReO_4^- onto Ag-4,4'-bipyridine and has shown that the best fit is obtained with the Sips isotherm.

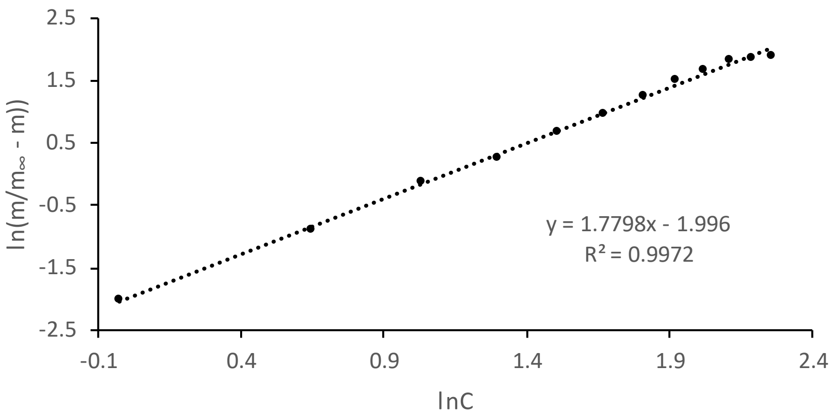

Figure 6-5. Linear form of the Sips isotherm for the adsorption of NaReO4 into the 35 layer Ag-4-4-bipyridine MOF thin film, derived from the experimental data. The parameter $m_{\infty}=34.8\ \mu g/cm^2$ *is calculated iteratively in order to produce a linear fit.*

Figure 6.6 shows every repeat recorded of the experiment of figure 5.13. As can be seen, the data is reproducible across experiments. The values of the Sips parameters obtained through the linear form of the isotherm of each of the 6 experimental data sets were $n = 1.73\ (\pm\ 0.066)$, $k = 0.153\ (\pm\ 0.014)\ mM^{-1}$ and $m_{\infty} = 35.9\ (\pm\ 0.88)\ \mu g\ cm^{-2}$. When those parameters are implemented into Equation 6.5, the Sips fit presented in figure 6.6 is obtained. The model clearly shows good agreement with the experimental data.

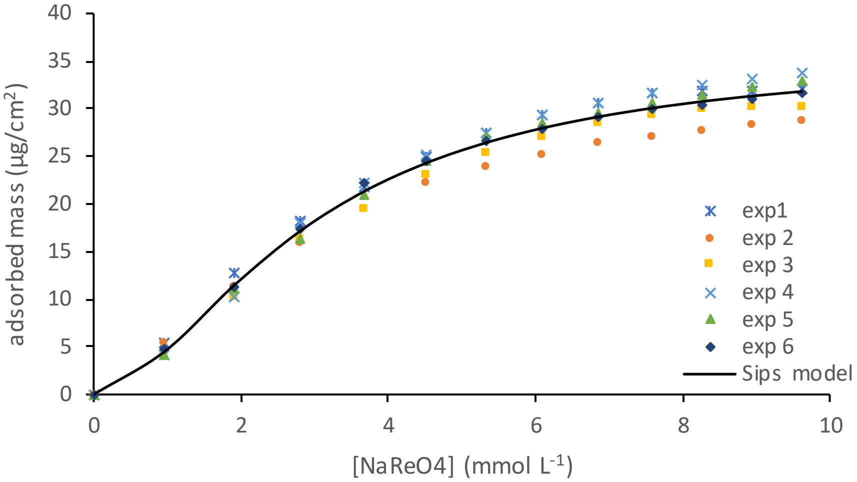

Figure 6-6. Comparison between the experimental data of the $NaReO_4$ adsorption into the 35 layers Ag-4-4-bipyridine film shown with the different type of points and the Sips model shown with the black straight line.

Data obtained with the 50-layer films of Ag-4,4'-bipyridine were fit using exclusively the Sips isotherm model. Following the same methodology, the linear form of one set of data is shown in Figure 6-7 and was used to extract the Sips fitting parameters. This was repeated for all the experiments and the average values of the Sips parameters were obtained as $n = 2.02$ ($\pm$ 0.18), $k = 0.122$ (± 0.053) and $m_\infty = 39.2$ ($\pm$ 3.17). Figure 6.8 shows all data recorded on the 50-layer film with ReO_4^-, alongside all the individual Sips models and the Sips model derived from these average parameters. It may be seen that the reproducibility of the data is less convincing on the 50-layer film than it was with the 35-layer film. As a result, the model appears less representative of the data recorded.

In fact, each of the data sets has been modelled using the linear expression of the Sips isotherm and yielded excellent regression coefficients (R^2 in the range 0.9977 to 0.9998) suggesting that the model accurately describes the experimental datasets. However, the general trends are different as can be seen from figure 6.8 where experiment 1 and 2 are in good agreement with one another but differ substantially from experiments 3 and 4 who are themselves in good agreement with one another. To aid our analysis, the fitting parameters for each experiment is reproduced in Table 6-1.

exp no	*1*	*2*	*3*	*4*
n	1.78	1.53	2.44	2.32
k (mM⁻¹)	0.277	0.163	0.020	0.027
m_∞ (μg cm^{-2})	31.7	34.7	47.6	42.7
R^2	0.9998	0.9996	0.9992	0.9977

Table 6-1. The Sips parameters obtained for consecutive $NaReO_4$ adsorption experiments into the 50-layer MOF film though linear analysis of the data.

The m_∞ values are about 25% lower for experiments 1 and 2 than those for experiments 3 and 4, suggesting a substantial increase in the total capacity for adsorption in the latter. This is observed concurrently to a decrease in the Sips affinity constant (k) by roughly an order of magnitude between experiments 1/2 and 3/4 suggesting a drastic reduction in the affinity of the film for the adsorbate. This behaviour was not observed in conjunction with the 35-layer film. It is possible that a partial breakdown in the film could result in a larger surface area available for adsorption (increased m_∞) and a reduction in the integrity of that film which may lead to a reduction in k value.

However, the general trend of the experimental data and the model are in fair agreement suggesting that whatever leads to the differences between individual experiments is not linked to the fundamental mechanism of adsorption. The differences in Sips parameters between the two film thicknesses will be discussed after the analysis of all the data recorded has been conducted.

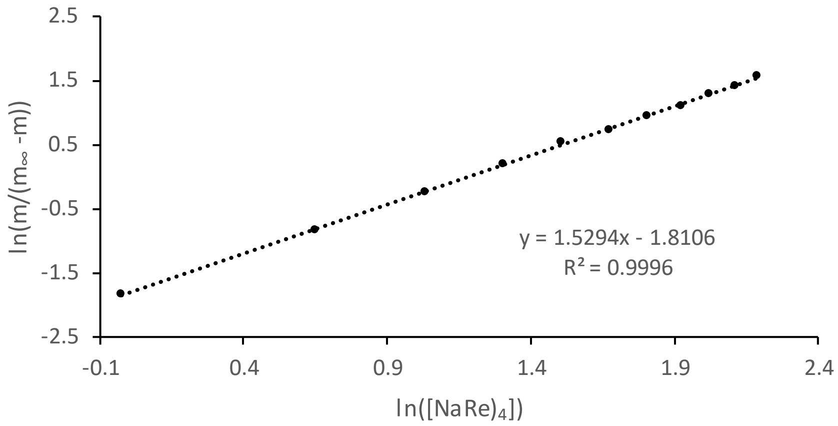

Figure 6-7. Linear form of the Sips isotherm for the adsorption of $NaReO_4$ into the 50 layer Ag-4-4-bipyridine MOF thin film, derived from the experimental data.

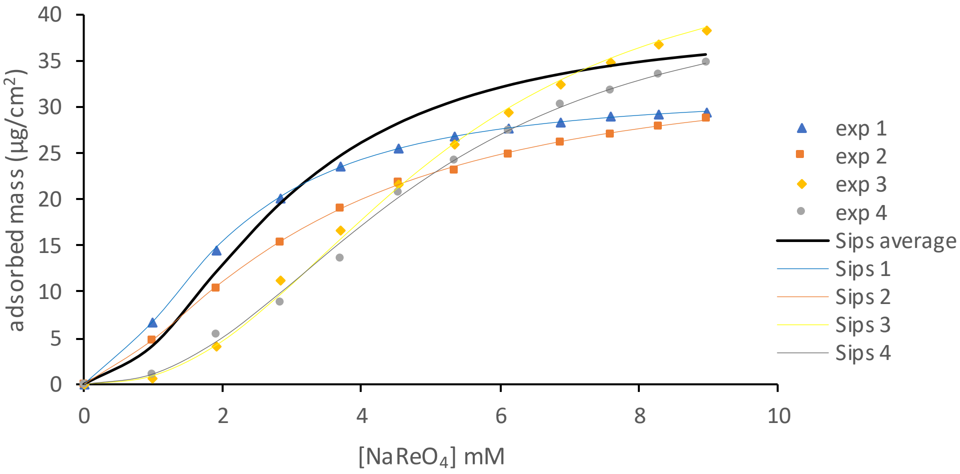

Figure 6-8. Comparison between the experimental data of the $NaReO_4$ adsorption into the 50 layers Ag-4-4-bipyridine film shown with the different type of points and the Sips model shown with the black straight line.

6.3 Modeling of the NaCl adsorption data

6.3.1 Langmuir fit

Following the same methodology as for the perrhenate ion, NaCl adsorption data was fitted for all three selected isotherms (Langmuir, Freundlich and Sips). Starting with the Langmuir isotherm, the linear fit, which will provide the two Langmuir parameters is shown in Figure 6-9.

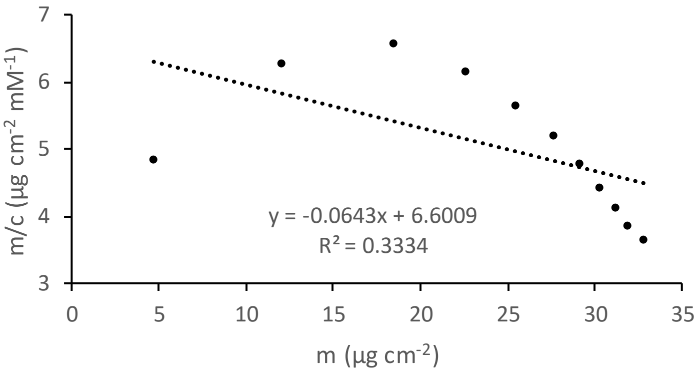

Figure 6-9 Linear form of the Langmuir isotherm for the adsorption of NaCl into the 35 layers Ag-4-4-bipyridine MOF thin film, derived from the experimental data.

It is once again clear that the Langmuir isotherm does not describe the experimental data of the NaCl adsorption. For reasons of completeness, the non-linear fit, calculated with the parameters provided by the best fitted line in Figure 6-9, which are $m_\infty = 102.6\ \mu g/cm^2$ and $k = 0.064\ mM^{-1}$ is shown in Figure 6-10. As already mentioned, it is even more clear now that the Langmuir isotherm does not describe this set of data.

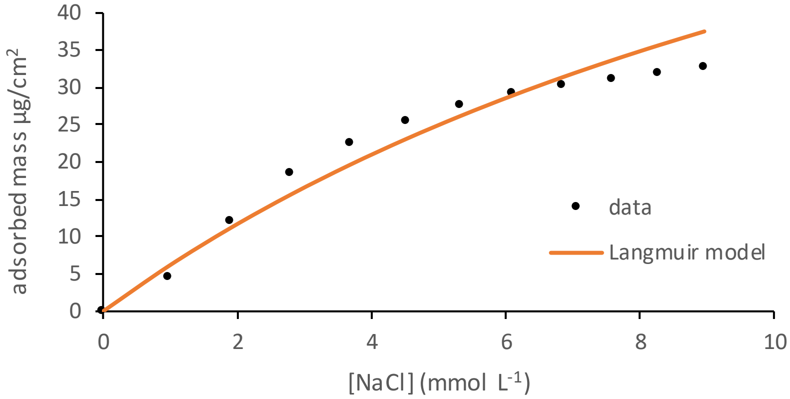

Figure 6-10. Comparison between the experimental data of the NaCl adsorption into the 35 layers Ag-4-4-bipyridine film shown with the black dots and the Langmuir model shown with the orange straight line.

6.3.2 Freundlich fit

The linear form of the Freundlich model is plotted in Figure 6-11, with a satisfactory regression factor of $R^2 = 0.926$. The slope of the best fitted line provides *n = 0.82*, while the interception point provides $k = 6.45\ \mu g\ mM^{-1}cm^{-2}$.

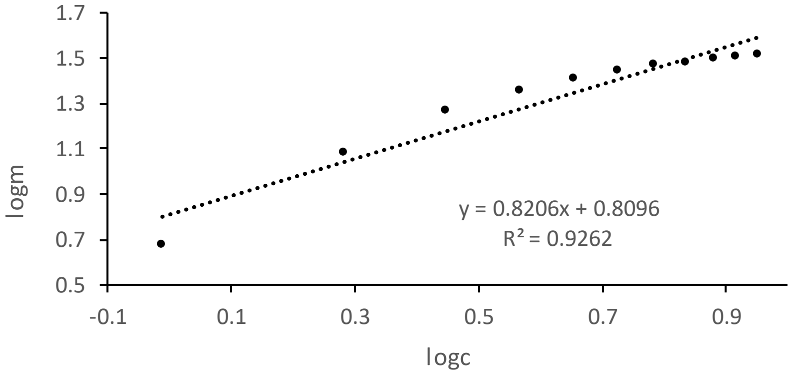

Figure 6-11. Linear form of the Freundlich isotherm for the adsorption of NaCl into the 35 layers Ag-4-4-bipyridine MOF thin film, derived from the experimental data.

However, once those values are implemented into the non-linear Freundlich model, the fit in the experimental data is not good enough, as shown in Figure 6-12. Just as in the case of $NaReO_4$, the Freundlich isotherm seems to deviate significantly in the high concentration range, and we can safely conclude that it does not describe the adsorption of NaCl in the thin film.

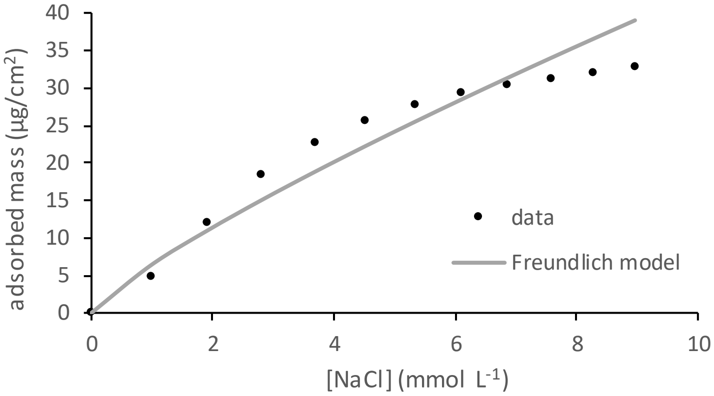

Figure 6-12. Comparison between the experimental data of the NaCl adsorption into the 35 layers Ag-4-4-bipyridine film shown with the black dots and the Freundlich model shown with the grey line.

Modelling the same data according to the linear form of the Sips isotherm, yields Figure 6-13. The high linearity of this plot shows that the model describes the adsorption of NaCl accurately and was used to analyse the remaining datasets. The average Sips parameters are obtained as $n = 1.84$ *(±0.17)*, $k = 0.154\ mM^{-1}$ *(±0.022)* and $m_\infty = 36.5\ \mu g/cm^2$ *(±0.52)*.

6.3.3 Sips fit

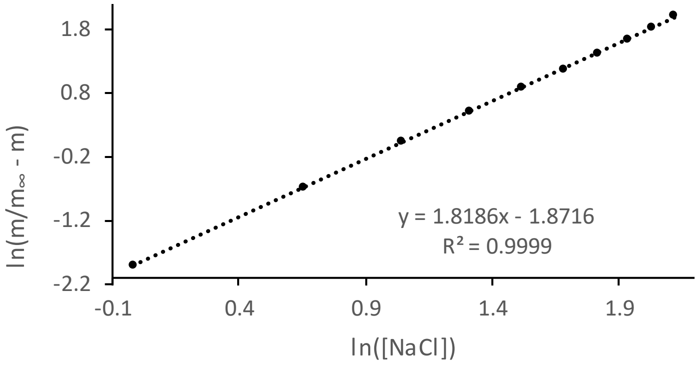

Figure 6-13. Linear form of the Sips isotherm for the adsorption of NaCl into the 35 layers Ag-4-4-bipyridine MOF thin film, derived from the experimental data. The parameter m_∞ = 36.2 µg/cm^2 is calculated iteratively in order to obtain a linear fit.

Figure 6.14 shows the data of all three repeats of this experiment alongside the trace computed from the average parameters and highlights the reproducibility of the recorded data and the goodness of the fit obtained from the modeling.

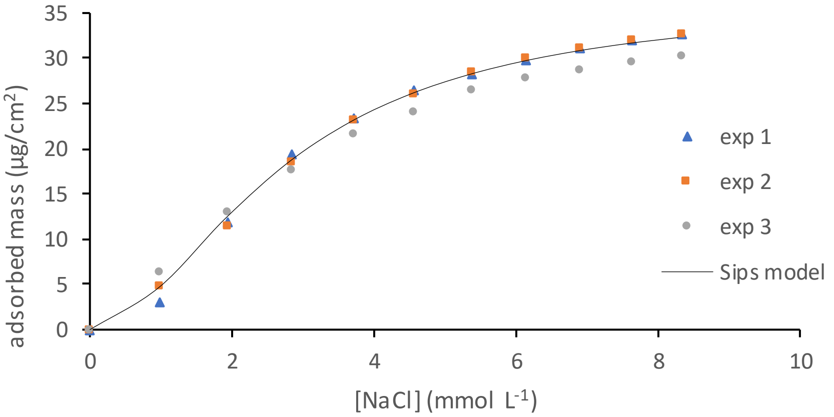

Figure 6-14. Comparison between the experimental data of the NaCl adsorption into the 35 layers Ag-4-4-bipyridine film shown with the different types of points and the Sips model shown with the black straight line.

Since the Sips isotherm best describes the experimental data for the adsorption of NaCl into the 35 layers Ag-4-4-bipyridine thin film, it will be used to model the data of the adsorption in the 50 layers film. The linear form of the Sips model for the adsorption of NaCl in the 50 layers film is shown in Figure 6-15.

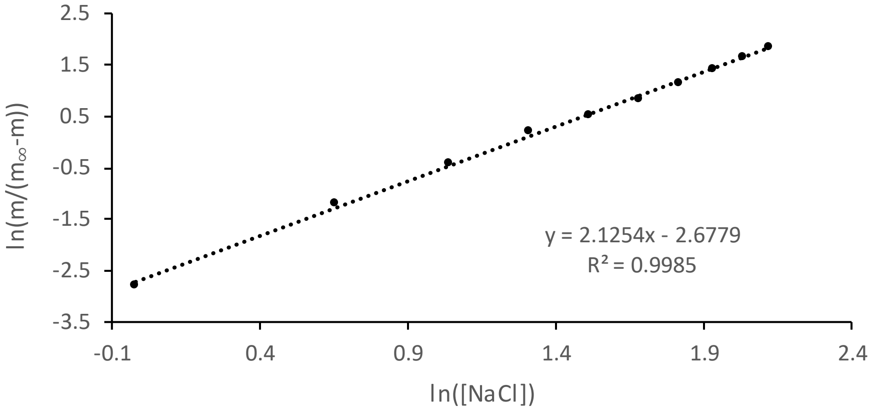

Figure 6-15. Linear form of the Sips isotherm for the adsorption of NaCl into the 50 layers Ag-4-4-bipyridine MOF thin film, derived from the experimental data. The parameter $m_\infty = 42.1\ \mu g/cm^2$ *is calculated iteratively in order to obtain a linear fit.*

The maximum adsorbed mass parameter $m_\infty = 42.1\ \mu g/cm^2$ was calculated iteratively in order to obtain a linear fit. The other two parameters of the Sips model were produced through the best fitted line as $n = 2.12$ and $k = 0.068\ mM^{-1}$. When those are implemented into Equation 6.5 the Sips isotherm is produced, shown in comparison to the experimental data in Figure 6-16.

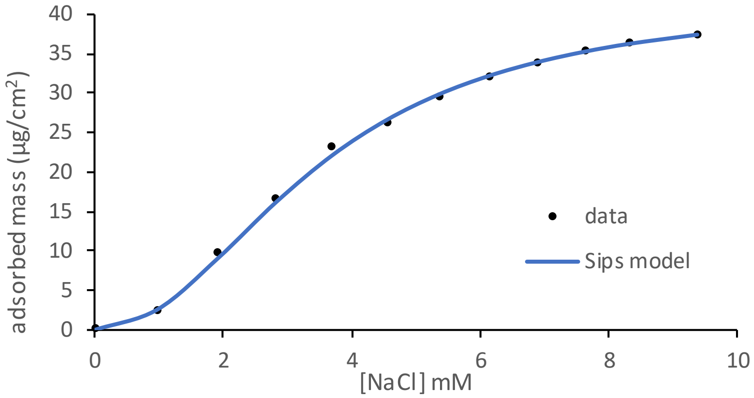

Figure 6-16. Comparison between the experimental data of the NaCl adsorption into the 50 layers Ag-4-4-bipyridine film shown with the black dots and the Sips model shown with the blue straight line.

The Sips isotherm was, again, the only model that successfully fitted into the experimental data of the adsorption of NaCl into the Ag-4-4-bipyridine thin film. The fact that different thicknesses of the film provided different physicochemical parameters could give an insight into the kinetics of the adsorption.

6.4 Modeling of the Na_2SO_4 adsorption data

6.4.1 Langmuir fit

Working in the same way as above, the experimental data of the adsorption of Na_2SO_4 into the 35 layers thin film are fitted into the Langmuir model first. Equation 6.2 provides the linear fit of Figure 6-17, through which the Langmuir parameters were obtained.

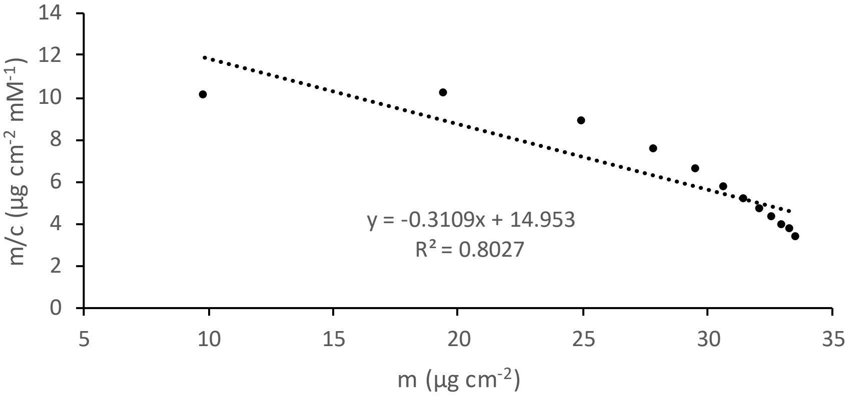

Figure 6-17. Linear form of the Langmuir isotherm for the adsorption of Na_2SO_4 into the 35 layers Ag-4-4-bipyridine MOF thin film, derived from the experimental data.

The fit seems to be more linear than the $NaReO_4$ and NaCl cases, but again is not good enough ($R^2 = 0.80$). The best fitted line provides $k = 0.311\ mM^{-1}$ and $m_\infty = 48.1\ \mu g/cm^2$. When those parameters are implemented into Equation 6.1, the non-linear Langmuir fit is obtained, shown in comparison to the experimental data in Figure 6-18. The fit is much better than the previous Langmuir fits, but again there seems to be some deviation in the high concentrations, suggested by the theoretical maximum adsorption calculated as 48.1 µg/cm^2, while the experimental seems to be around 33-34 µg/cm^2.

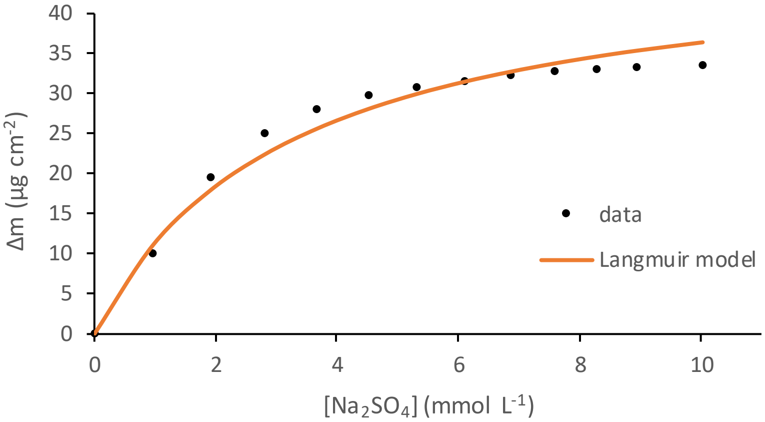

Figure 6-18. Comparison between the experimental data of the Na_2SO_4 adsorption into the 35 layers Ag-4-4-bipyridine film shown with the black dots and the Langmuir model shown with the orange straight line.

Although the Langmuir isotherm is a better fit for the Na_2SO_4 adsorption data than that of either ReO_4^- or Cl^-, the experimentally obtained data seems to plateau sooner and at a lower level that that predicted by the model, suggesting that the Langmuir isotherm is in fact not reflective of the adsorption mechanism at play for Na_2SO_4 .

6.4.2 Freundlich fit

The linear form of the Freundlich isotherm is therefore investigated next and shown in Figure 6-19.

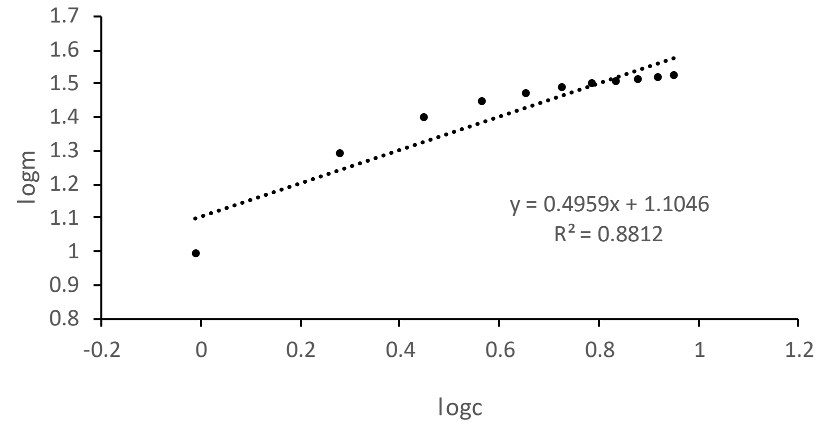

Figure 6-19 Linear form of the Freundlich isotherm for the adsorption of Na_2SO_4 into the 35 layers Ag-4-4-bipyridine MOF thin film, derived from the experimental data.

figure 6.19 provides a satisfactorily linear fit, through which the Freundlich parameters *n = 0.496* and *k = 12.7 μg* $mM^{-1}cm^{-2}$ are obtained. When those parameters are put into Equation 6.3, the Freundlich model is calculated, as shown in Figure 6-20. Like in the previous cases, it seems to deviate majorly in the high concentrations.

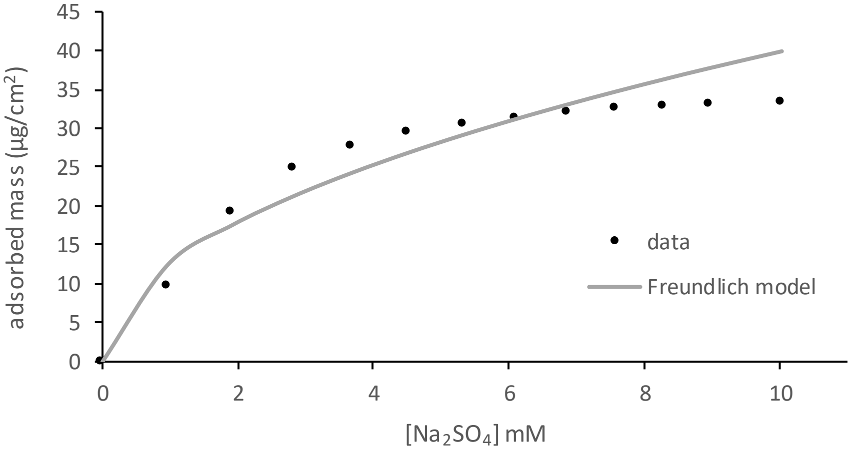

Figure 6-20. Comparison between the experimental data of the Na_2SO_4 adsorption into the 35 layers Ag-4-4-bipyridine film shown with the black dots and the Freundlich model shown with the grey straight line.

6.4.3 Sips fit

The same data is then fitted using the Sips isotherm the Na_2SO_4 adsorption into the 35 layers Ag-4-4-bipyridine thin film. Its linear form, which is shown in Figure 6-21, was calculated via Equation 6.6, for one set of experimental data.

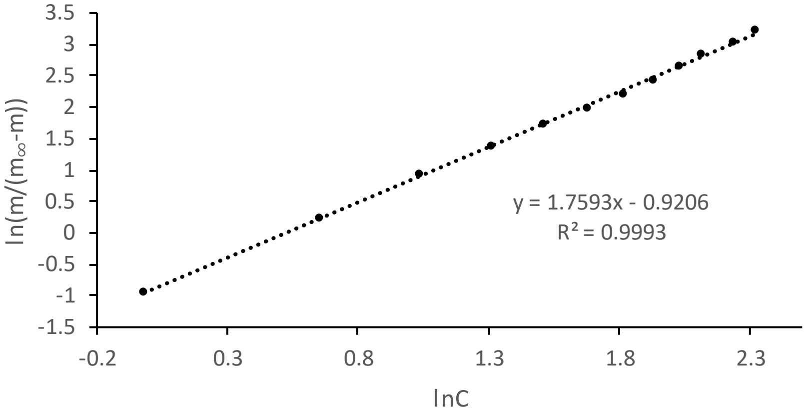

Figure 6-21. Linear form of the Sips isotherm for the adsorption of Na_2SO_4 *into the 35 layers Ag-4-4-bipyridine MOF thin film, derived from the experimental data. The parameter* $m_\infty = 34.9\ \mu g/cm^2$ *is calculated iteratively in order to obtain a linear fit*

The high linearity suggests that the model effectively describes the adsorption of Na_2SO_4, and is therefore used to analyse the remainder of the experimental datasets, leading to the determination of average Sips parameters as $n = 1.84\ (\pm 0.17)$, $k = 0.154\ mM^{-1}\ (\pm 0.022)$ and $m_\infty = 36.5\ \mu g/cm^2\ (\pm 0.52)$. hence providing the non-linear fit of the Sips model, shown in comparison to all the experimental data in Figure 6-22. This shows very good reproducibility across experiments and a very good fit of the model to the experimental data.

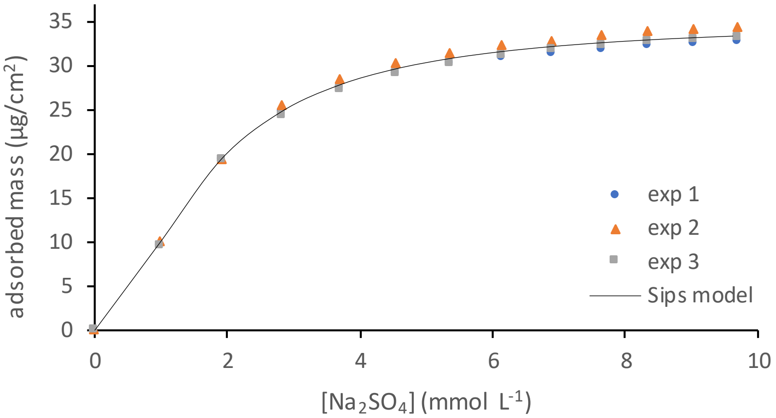

Figure 6-22. Comparison between the experimental data of the Na_2SO_4 adsorption into the 35 layers Ag-4-4-bipyridine film shown with the different types of points and the Sips model shown with the black straight line.

The goodness of fit for the Sips isotherm with the 35-layer film shows that this isotherm best describes the adsorption of Na_2SO_4 into the 35 layers thin film, and we will focus on this for the modelling of the 50-layer film. Following the same methodology, the linear form of one set of data is shown in Figure 6-23 and was used to extract the Sips fitting parameters. This was repeated for all the experiments and the average values of the Sips parameters were obtained as $n = 1.40\ (\pm 0.067)$ and $k = 0.641\ (\pm\ 0.089)\ mM^{-1}$ and $m_\infty = 33.3\ (\pm\ 4.50)\ \mu g/cm^2$ .Figure 6-24 shows all data recorded on the 50-layer film with SO_4^{2-} alongside all the individual Sips models and the Sips model derived from these average parameters. Likewise the ReO_4^- adsorption on the 50-layer film, the reproducibility of the data is less convincing on the 50-layer film than it was with the 35-layer film, as there is a huge variation in the m_∞ parameter. However, each of the data sets has been modelled using the linear expression of the Sips isotherm and yielded excellent regression coefficients suggesting that the model accurately describes the experimental datasets. To aid our analysis, the fitting parameters for each experiment is reproduced in Table 6-2.

exp no	*1*	*2*	*3*
n	1.47	1.21	1.52
k (mM^{-1})	0.476	0.891	0.556
m_∞ (µg cm^{-2})	34.2	21.7	43.6
R^2	0.9994	0.9982	0.9992

Table 6-2. The Sips parameters obtained for consecutive Na_2SO_4 adsorption experiments into the 50-layer MOF film though linear analysis of the data.

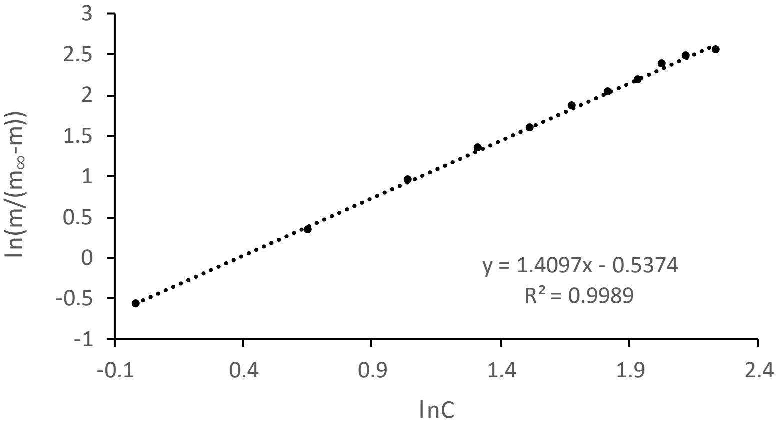

Figure 6-23. Linear form of the Sips isotherm for the adsorption of Na_2SO_4 into the 50 layers Ag-4-4-bipyridine MOF thin film, derived from the experimental data. The parameter m_∞ = 33.3 µg/cm^2 is calculated iteratively in order to obtain a linear fit

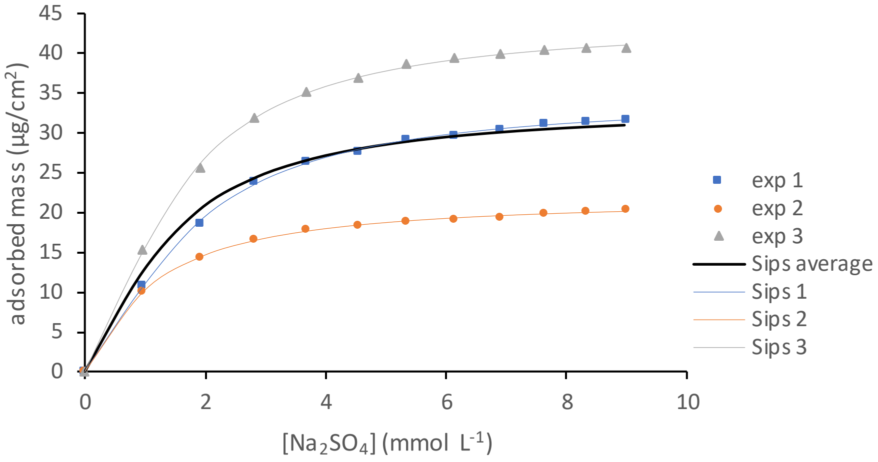

Figure 6-24. Comparison between the experimental data of the Na_2SO_4 adsorption into the 50 layers Ag-4-4-bipyridine film shown with the different types of points and the Sips model shown with the black straight line.

Although there is significant divergence between the experimental data, it is clear through the individual fits that the Sips model describes the adsorption of Na_2SO_4 into the 50 layers Ag-4-4-bipyridine film well. However, it would be inappropriate to use the mean values of the Sips parameters to draw any meaningful conclusions, given the size of their standard deviations.

6.5 Modeling of the Na_2CO_3 adsorption data

6.5.1 Langmuir fit

Finally, we get to model the adsorption of Na_2CO_3 into the Ag-4-4-bipyridine thin film, starting again with the data from the 35 layers film. All the isotherms used previously will be tested in the same way. So, starting with the Langmuir isotherm, its linear form, which will provide the Langmuir parameters, is shown in Figure 6-25.

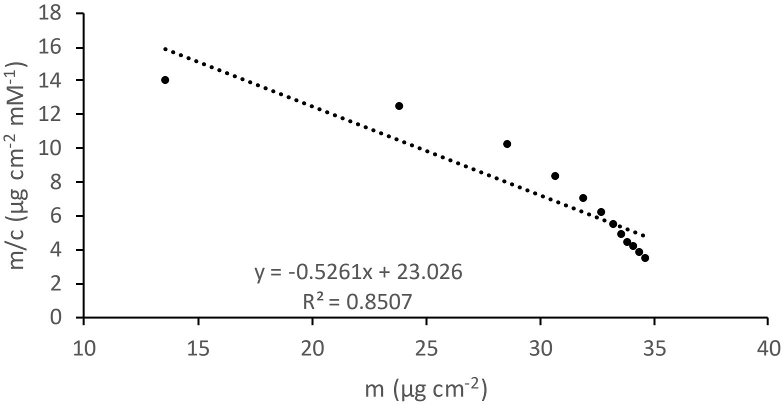

Figure 6-25. Linear form of the Langmuir isotherm for the adsorption of Na_2CO_3 into the 35 layers Ag-4-4-bipyridine MOF thin film, derived from the experimental data.

In contrast to the previous cases, the fit is satisfactorily linear ($R^2 = 0.85$), while the best fitted line provides $m_\infty = 43.8\ \mu g/cm^2$ and $k = 0.526\ mM^{-1}$. When those values are implemented into Equation 6.1, the Langmuir adsorption isotherm is produced, as shown in Figure 6-26. The fit into the experimental data is indeed much better than in the cases of $NaReO_4$ and NaCl, but still it seems to deviate in the high concentrations.

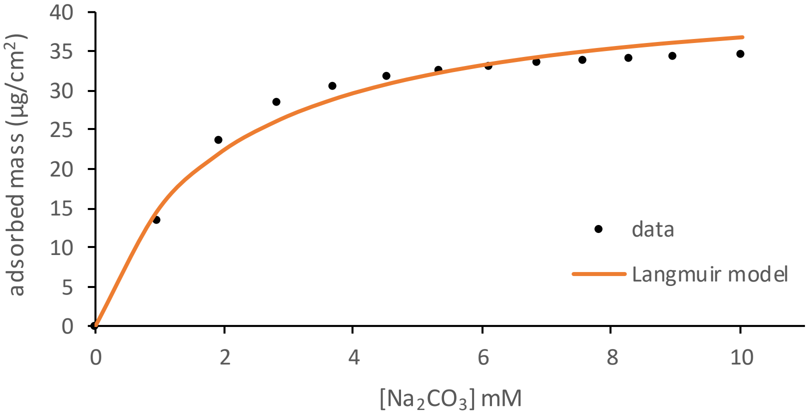

Figure 6-26. Comparison between the experimental data of the Na_2CO_3 adsorption into the 35 layers Ag-4-4-bipyridine film shown with the black dots and the Langmuir model shown with the orange straight line.

6.5.2 Freundlich fit

The modeling process with the Freundlich isotherm was performed, the linear form of which is presented in Figure 6-27. This provides a satisfactorily linear fit, through which the Freundlich parameters $n = 0.368$ and $k = 16.9\ \mu g\ mM^{-1}cm^{-2}$ are obtained.

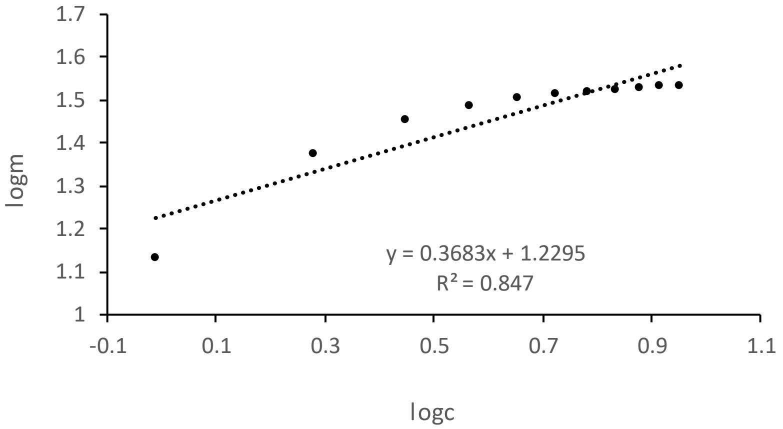

Figure 6-27. Linear form of the Freundlich isotherm for the adsorption of Na_2CO_3 into the 35 layers Ag-4-4-bipyridine MOF thin film, derived from the experimental data.

However, once those values are implemented into the non-linear Freundlich model, the fit in the experimental data is not good enough, as shown in Figure 6-28. Freundlich isotherm seems to deviate significantly in the high concentration range, and we can safely conclude that it does not describe the adsorption of Na_2CO_3 in the thin film.

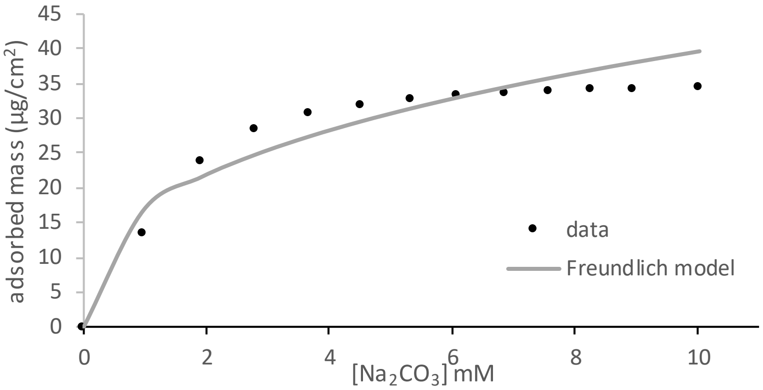

Figure 6-28. Comparison between the experimental data of the Na_2CO_3 adsorption into the 35 layers Ag-4-4-bipyridine film shown with the black dots and the Freundlich model shown with the grey straight line.

6.5.3 Sips fit

So, we finish the modeling with the Sips isotherm, the linear form of which is presented in Figure 6-29. The perfectly linear fit was obtained using a value a value of $m_\infty = 35.2\ \mu g/cm^2$. Working in the same way for the rest of the data provides us with the all the Sips parameters as $n = 1.75\ (\pm\ 0.008)$, $k = 0.665\ mM^{-1}\ (\pm\ 0.012)$ and $m_\infty = 35.3\ \mu g/cm^2\ (\pm\ 0.422)$.

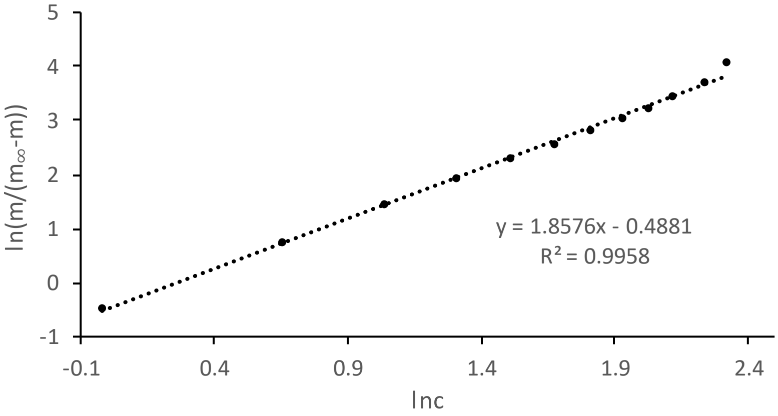

Figure 6-29. Linear form of the Sips isotherm for the adsorption of Na_2CO_3 into the 35 layers Ag-4-4-bipyridine MOF thin film, derived from the experimental data. The parameter $m_\infty = 35.2\ \mu g/cm^2$ is calculated iteratively in order to obtain a linear fit.

The Sips model, obtain through the above values, is presented in Figure 6-30. Once again, it seems that the Sips isotherm is the one that describes with exceptional accuracy the experimental data even in the case of the adsorption of Na_2CO_3 in the Ag-4-4-bipridine thin film.

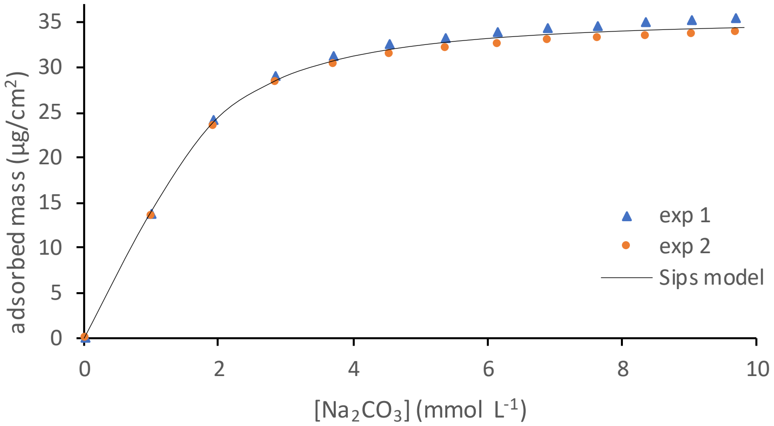

Figure 6-30. Comparison between the experimental data of the Na_2CO_3 *adsorption into the 35 layers Ag-4-4-bipyridine film shown with the different types of points and the Sips model shown with the black straight line.*

Having proved this, it would be safe to assume that the Sips model is the one to describe the data from the 50 layers film, so it will be the only one to be tested to this direction. Working in the same way, the linear form, which will provide the Sips parameters is shown in Figure 6-31. The maximum adsorbed mass in infinite concentration was calculated iteratively as $m_\infty = 33.1\ \mu g/cm^2$,in order to obtain a linear fit, while from the slope of the fit we get $n = 1.70$ and from the interception we get $k = 0.639\ mM^{-1}$.

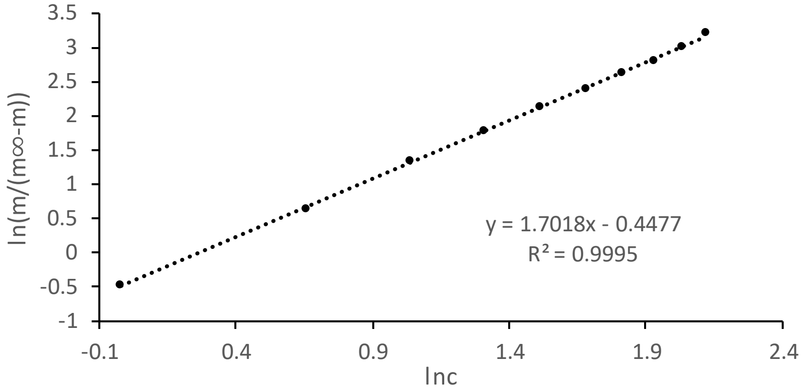

Figure 6-31. Linear form of the Sips isotherm for the adsorption of Na_2CO_3 into the 50 layers Ag-4-4-bipyridine MOF thin film, derived from the experimental data. The parameter $m_\infty = 33.1$ μg/cm^2 is calculated iteratively in order to obtain a linear fit.

When those parameters are implemented into the Sips model, a fit in exceptionally good coordination with the experimental data is obtained, as shown in Figure 6-32. It would be safe to conclude that the Sips isotherm is the one describing the adsorption of Na_2CO_3 in the Ag-4-4-bipyridine thin film.

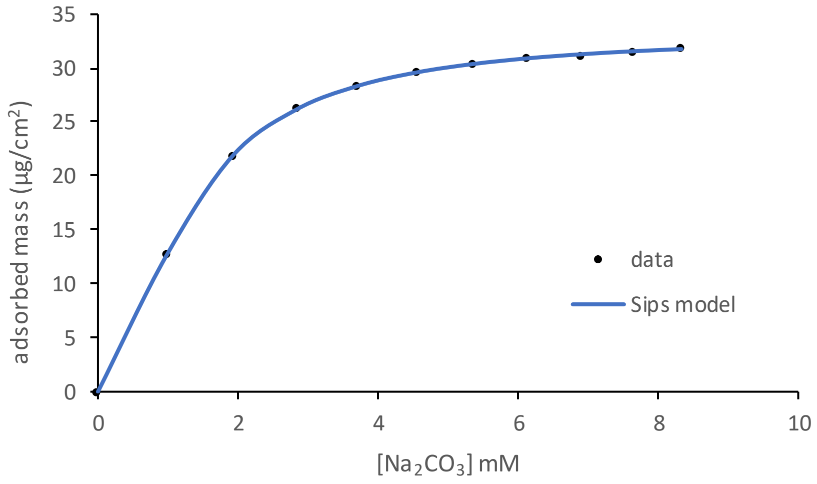

Figure 6-32 Comparison between the experimental data of the Na_2CO_3 adsorption into the 50 layers Ag-4-4-bipyridine film shown with the black dots and the Sips model shown with the blue straight line.

6.6 Discussion

The systematic modeling of the experimental data with well-understood adsorption isotherms led to the conclusion that the Sips isotherm unambiguously best describes the adsorption of every analyte considered in the previous chapter. The implication of this result is that adsorption takes place across multiple layers, rather than in a single monolayer, (best described by the Langmuir isotherm) but that an upper limit exists on the amount of material may be adsorbed in the film, typified by the plateau reached by every set of data, precluding the use of the Freundlich isotherm. Table 6-3 summarises the fitting parameters obtained for each analyte considered both the 35- and 50-layer films.

In order to make more sense of what those values mean for the adsorption mechanism, it is instructive to plot all the isotherms on a single graph. Starting with the 35 layers film, the four Sips isotherms for the adsorption of $NaReO_4$, NaCl, Na_2SO_4 and Na_2CO_3 are shown in Figure 6-33. Since it was shown that the Sips isotherm accurately describes the experimental data, it is acceptable to compare just the models.

Reviewing the data of Table 6.1, it may be observed, that the m_∞ factor, which reflects the total maximum mass of adsorbate immobilized onto the film and affects the height of the plateau in the graph, is very similar for all the analytes. This is may also be observed graphically in Figure 6-33, where all the isotherms reach similar plateaus. This contradicts the initial hypothesis of the anion exchange as the mechanism of adsorption, as suggested in the literature and reproduced in our experiments involving bulk crystals of the Ag-4-4-bipyridine MOF described in Chapter 5.

35 layers Ag-4-4-bipyridine film			
	n	k (mM^{-1})	m_∞ ($\mu g\ cm^{-2}$)
$NaReO_4$	1.73 (± 0.066)	0.153 (± 0.014)	35.8 (± 0.88)
NaCl	1.84 (± 0.17)	0.154 (± 0.021)	36.2 (± 0.52)
Na_2SO_4	1.71 (± 0.017)	0.409 (± 0.0057)	35.0 (± 0.43)
Na_2CO_3	1.73 (± 0.088)	0.665 (± 0.012)	35.3 (± 0.42)
50 layers Ag-4-4-bipyridine film			
	n	k (mM^{-1})	m_∞ ($\mu g\ cm^{-2}$)
$NaReO_4$	2.02 (± 0.18)	0.122 (± 0.053)	39.2 (± 3.17)
NaCl*	2.12	0.0687	42.1
Na_2SO_4	1.40 (± 0.067)	0.641 (± 0.089)	33.3 (± 4.51)
Na_2CO_3*	1.70	0.639	33.1

*Table 6-3. All the Sips parameters as calculated in the previous sections, for all the adsorbents, first for the adsorption into the 35 layers Ag-4-4-bipyridine film and then for the adsorption into the 50 layers film. The * sign indicates that there was only one set of data, so there are no standard deviations.*

The replacement of the nitrate counterions from the MOF structure with the range of analytes studied should not result in a consistent m_∞ value since each target analyte has a different molecular mass. Indeed, this is most obvious in the case of the chloride ion which has a molecular mass lower than that of the nitrate ion which it is purported to replace, 35.5 g mol^{-1} and 62.0 g mol^{-1}, respectively, and which should result in an overall mass loss rather than the mass gain observed.

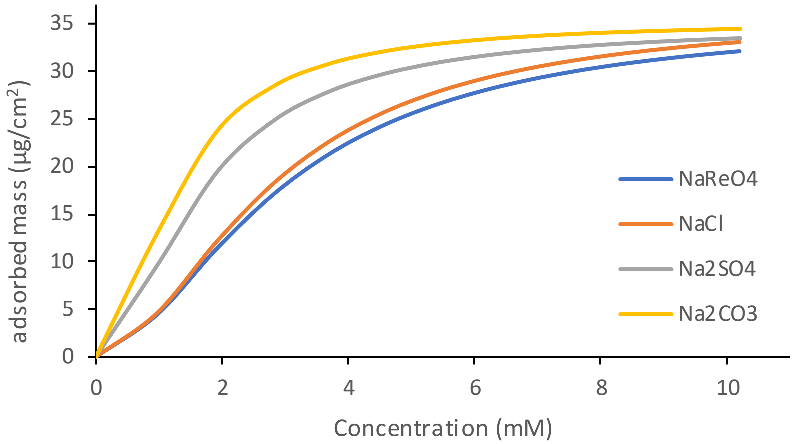

Figure 6-33. The Sips isotherms of the adsorption of $NaReO_4$, NaCl, Na_2SO_4 and Na_2CO_3 into the 35 layers Ag-4-4-bipyridine film.

Another contradiction to the ion exchange hypothesis is the fact that the adsorption of ReO_4^- appears to be reversible. As previously stated, Zhu *et al.* reported that when ReO_4^- is exchanged for NO_3^- into the Ag-4,4'-bipyridine network as the counter anion, the structure of the MOF alters irreversibly [158] with the spheroidal perrhenate-free particles transforming into needle-like structures in the presence of the anion. This was also confirmed by our own experiments with the bulk MOF crystals, presented in Chapter 5. The reversible nature of the adsorption process previously reported suggests that in the case of our thin film, anion exchange (which would require washing with highly concentrated NO_3^- solution) had not taken place. This may be due to the impossibility of the film to rearrange and trap the anion of interest as a result of its tethering to the gold electrode of the QCM, confining the movement of the atoms within the network. This becomes more evident when the SEM images of the MOF thin film before and after the exposure to ReO_4^- are compared, as shown in Figure 6-34 A & B, respectively. No change in the surface of the film is observed after the exposure to ReO_4^-, contrary to the reports by Zhu, *et al* [158] and our own experiments on the bulk crystals presented in figures 5.1 and 5.3 respectively. Since the thermodynamics of the system cannot be lowered by the exchange of nitrate for perrhenate as observed in the bulk, the anion exchange mechanism must be ruled out.

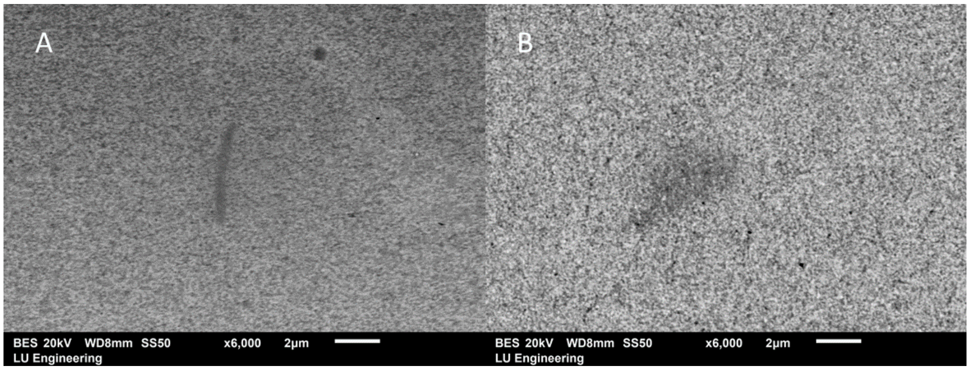

Figure 6-34. SEM images of the MOF thin film A) pre-exposure and B) post-exposure to ReO_4^-.

Returning to the data summarized in Table 6-3, it may be seen that the value of the adsorption affinity parameter*, k*, is the only parameter that differs significantly between the four different adsorbents. Furthermore, its value for $NaReO_4$ and NaCl is very similar, while for Na_2SO_4 and Na_2CO_3 it is almost 2.5 and 4 times larger, respectively. The value of *k* impacts the steepness of the initial rise in the mass vs. concentration curve (figure 5), in other words, the higher the value of *k*, the easier it becomes for the adsorbent to get into the film. For example, while in 1 mmol L^{-1} of $NaReO_4$, almost 5 μg/cm^2 are adsorbed into the film, at the same concentration of Na_2SO_4 the adsorbed mass reaches 13 μg/cm^2. This also reinforces our assumption that anion exchange cannot be the mechanism leading to these measured mass changes, as it would be impossible for the much lighter and doubly charged SO_4^{2-} anion to lead to heavier adsorption than the much heavier ReO_4^-.

Having ruled out the anion exchange mechanism for these MOF-modified QCM substrates, we must now attempt to not only determine the adsorption mechanism that obtains under our experimental conditions, but also identify the nature of the adsorbate. The lack of anion exchange means that no anions can enter the film for charge conservation reasons. Given the similarities in the m_∞ across all experiments summarized in Table 6-3, it is probable that all experiments are affected by the same species, and since all experiments were carried out using sodium salts of the relevant anions, the next logical step is to recast the data for the sodium cation concentration. This is further supported by the values of k reported in Table 6-3 which are similar between monocation salts and similar between dication salts. In the analysis above, the concentrations taken into account were that of the anions, which in the cases of $NaReO_4$ and NaCl are the same with those of Na^+, but in the cases of Na_2SO_4 and Na_2CO_3 the concentration of Na^+ is double of the anions. So, in order to confirm this hypothesis, the adsorption graphs of those two salts will be replotted and the Sips isotherms will be recalculated as a function of sodium concentration.

So, taking Figure 5.22 from the previous chapter and replotting in terms of Na^+ concentration, which is double, provides Figure 6-35, for the adsorption of Na_2SO_4 into the 35 layers film.

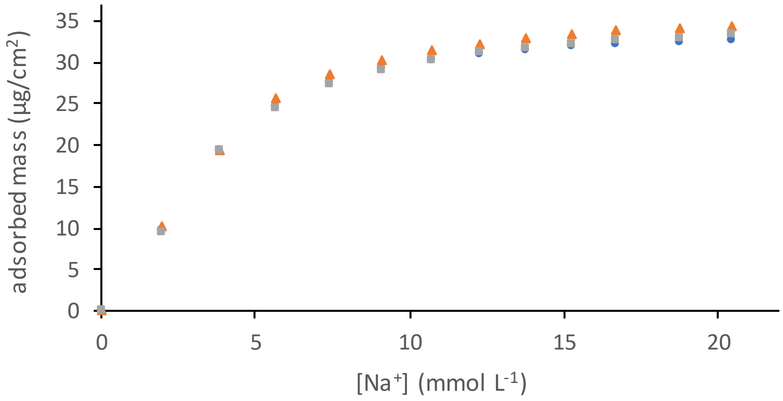

Figure 6-35. Adsorbed mass per surface area plotted as a function of Na^+ concentration from Na_2SO_4 for the 35 layers MOF thin film coated QCM of 3 different adsorption experiments with the same thin film.

Working as previously, the linear form of the Sips isotherm is shown in Figure 6-36, calculated using the value $m_\infty = 34.9\ \mu g/cm^2$.

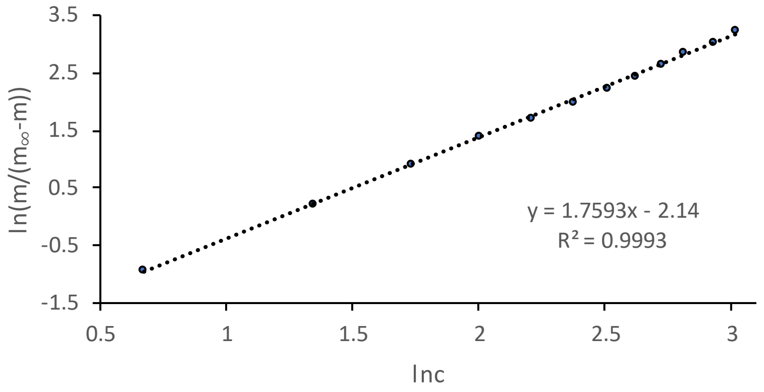

Figure 6-36. Linear form of the Sips isotherm for the adsorption of Na_2SO_4 *into the 35 layers Ag-4-4-bipyridine MOF thin film, derived from the experimental data and considering the concentration of* Na^+*. The parameter* $m_\infty = 34.9\ \mu g/cm^2$ *is calculated iteratively in order to obtain a linear fit.*

After analyzing all the data, the Sips parameters are obtained as $n = 1.73\ (\pm\ 0.018)$ and $k = 0.122\ (\pm\ 0.00065)\ mM^{-1}$ and $m_\infty = 35.0\ (\pm\ 0.43)\ \mu g/cm^2$. When those values are implemented into Equation 6.5, the Sips isotherm is obtained, as shown in comparison to the experimental data in Figure 6-37.

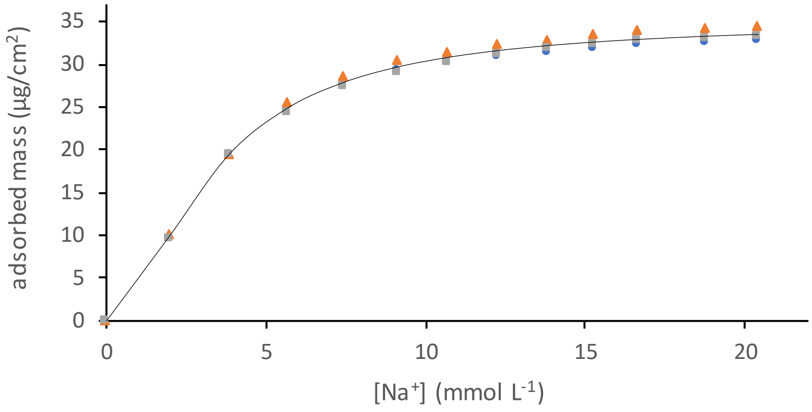

Figure 6-37. Comparison between the experimental data of the Na_2SO_4 adsorption into the 35 layers Ag-4-4-bipyridine film shown with the different types of points and the Sips model shown with the black straight line, considering the concentration of Na^+.

Working in the same way for the Na_2CO_3 data, Figure 5.28 is replotted against the concentration of Na^+, providing Figure 6-38.

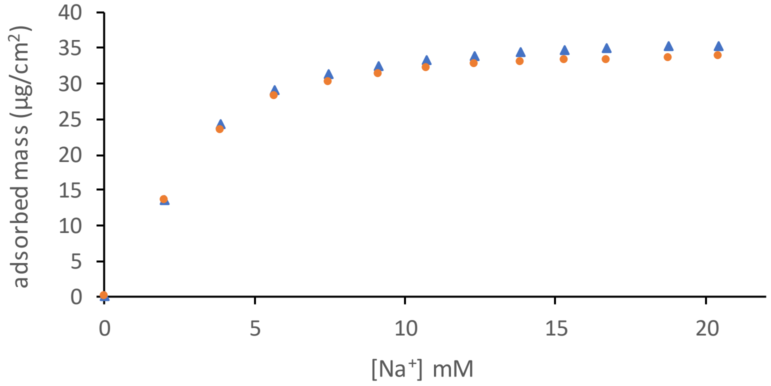

Figure 6-38. Adsorbed mass per surface area plotted as a function of Na^+ concentration from Na_2CO_3 for the 35 layers MOF thin film coated QCM of 2 different adsorption experiments with the same thin film.

The linear form of the Sips isotherm for one set of data is shown in Figure 6-39, calculated using the value $m_\infty = 35.2\ \mu g/cm^2$.

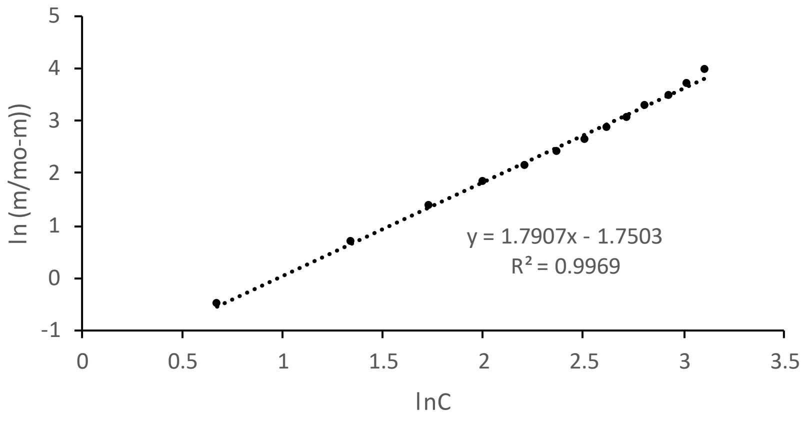

Figure 6-39. Linear form of the Sips isotherm for the adsorption of Na_2CO_3 into the 35 layers Ag-4-4-bipyridine MOF thin film, derived from the experimental data and considering the concentration of Na^+. The parameter $m_\infty = 36.2\ \mu g/cm^2$ is calculated iteratively in order to obtain a linear fit.

After the analysis of all the set of data, the Sips parameters are now calculated as $n = 1.80$ (± 0.082) and $k = 0.188\ (\pm 0.015)\ mM^{-1}$ and $m_\infty = 35.3\ (\pm 0.44)$ µg/cm^2 the Sips isotherm is obtained in Figure 6-40.

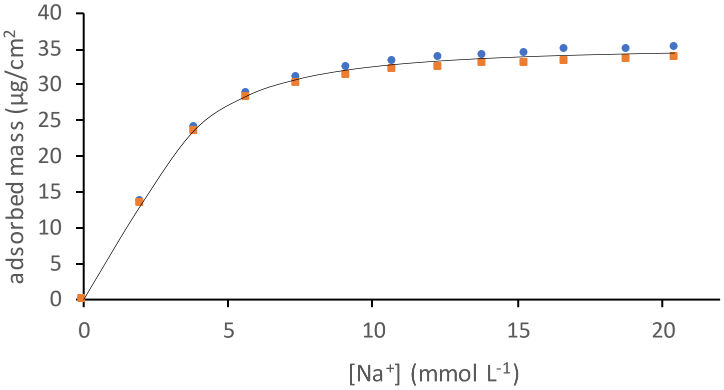

Figure 6-40. Comparison between the experimental data of the Na_2CO_3 adsorption into the 35 layers Ag-4-4-bipyridine film shown with the different types of points and the Sips model shown with the black straight line, considering the concentration of Na^+.

Although the data from the 50 layers film have not been discussed yet, there is nothing implying anything different is happening there, so the Sips parameters will be recalculated for those sets of data, as well. Since the transformation worked well for the data of the 35 layers film, let us provide directly the new Sips parameters. For the Na_2SO_4 data of the 50 layers film, the Sips parameters in terms of Na^+ concentration are $m_\infty = 33.3\ (\pm\ 4.5)\ \mu g/cm^2$, $k = 0.246\ (\pm\ 0.048)\ mM^{-1}$ *and* $n = 1.41\ (\pm\ 0.07)$ while for Na_2CO_3 the parameters are $m_\infty = 33.1\ \mu g/cm^2$, $k = 0.196\ mM^{-1}$ *and* $n = 1.70$. To sum up, the all the parameters calculated through the concentration of Na^+ are gathered in Table 6-4.

35 layers Ag-4-4-bipyridine film			
	n	k (mM^{-1})	m_∞ ($\mu g\ cm^{-2}$)
$NaReO_4$	1.73 (± 0.066)	0.153 (± 0.014)	35.8 (± 0.88)
NaCl	1.84 (± 0.17)	0.154 (± 0.021)	36.2 (± 0.52)
Na_2SO_4	1.73 (± 0.018)	0.122 (± 0.00065)	35.0 (± 0.45)
Na_2CO_3	1.80 (± 0.082)	0.181 (± 0.015)	35.3 (± 0.44)
50 layers Ag-4-4-bipyridine film			
	n	k (mM^{-1})	m_∞ ($\mu g\ cm^{-2}$)
$NaReO_4$	2.02 (± 0.18)	0.122 (± 0.053)	39.2 (± 3.17)
NaCl*	2.12	0.0687	42.1
Na_2SO_4	1.40 (± 0.07)	0.246 (± 0.048)	33.3 (± 4.50)
Na_2CO_3*	1.70	0.196	33.1

*Table 6-4 All the Sips parameters calculated for the concentration of Na^+, for all the adsorbents, first for the adsorption into the 35 layers Ag-4-4-bipyridine film and then for the adsorption into the 50 layers film. The * sign indicates that there was only one set of data, so there are no standard deviations.*

By comparing the values of the parameters for Na_2SO_4 and Na_2CO_3 between Table 6.1 and Table 6.2, it is easily observed that the only difference is the value of *k*. When the concentration of Na^+ cations is taken into account, the value of *k* for those salts is in good agreement to that of NaCl and $NaReO_4$, varying just in the second significant figure. Figure 6-41 shows the normalized isotherms for all species studied.

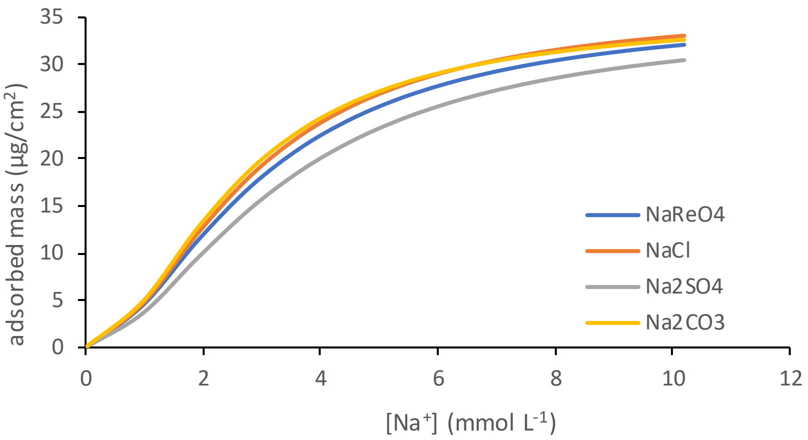

Figure 6-41. The Sips isotherms of the adsorption of $NaReO_4$*,* $NaCl$*,* Na_2SO_4 *and* Na_2CO_3 *into the 35 layers Ag-4-4-bipyridine film, calculated for the* Na^+ *concentration.*

In this case, the adsorption rate, represented by *k,* is comparable for all the isotherms, a fact that probably validates the approach of the sodium concentration in the different salt solutions. What is more, the fact that all the isotherms look so similar, after they were normalized to the concentration of sodium cations, strongly suggests that what is getting adsorbed into the film is indeed the Na^+. Thus, Figure 6-42 shows all the data recorded for all salts as a function of Na^+ concentration alongside the Sips isotherm calculated from the average of all individual models; $n = 1.77$ *(± 0.093),* $k = 0.150$ *(± 0.016)* mM^{-1} and $m_\infty = 35.8$ *(± 0.73)* $\mu g\ cm^{-2}$.

The most likely mechanism for this uptake of sodium cations into the MOF matrix is through electrostatic interaction between its positive charge and the π-electron clouds of the bipyridine rings which present a significant electronegative area of the frameworks. The weaker nature of this type of interactions also helps to explain the reversibility of the process.

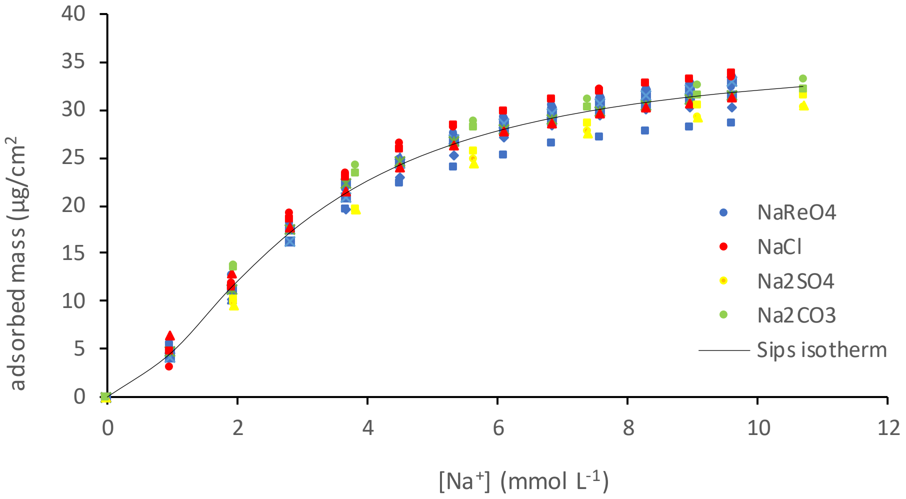

Figure 6-42. The adsorption data of the experiments with $NaReO_4$ *(blue marks), NaCl (red marks),* Na_2SO_4 *(yellow marks) and* Na_2CO_3 *(green marks) of the 35-layer film plotted with a Sips isotherm modeling the overall adsorption of* Na^+ *into the Ag-4,4'-bipyridine thin film.*

As for the 50-layer film, it is likely that Na^+ adsorption is also taking place. Figure 6-43 shows the adsorption data recorded on the 50-layer MOF-modified QCM crystal and recast vs. concentration of Na^+ ions. The data in figure 6-43 is more spread out than it was for the 35-layer film shown in figure 6-42. This spread preventing us from calculating an overall isotherm. Furthermore, experiments with the 100 and 150 layer films did not result in the measurement of any mass changes. This is likely due to excessive damping of the crystal as a result of the increased thickness of the film and further work is needed to verify this hypothesis.

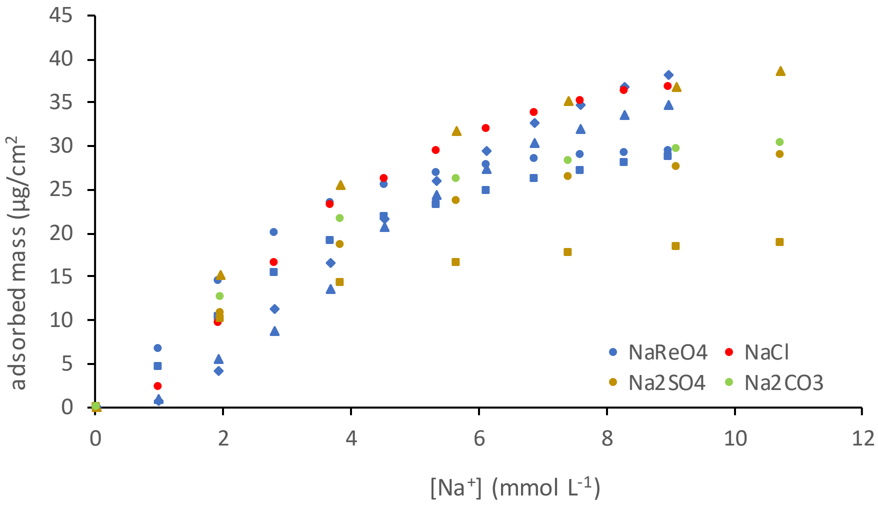

Figure 6-43. The adsorption data of the experiments with $NaReO_4$ (blue marks), NaCl (red marks), Na_2SO_4 (yellow marks) and Na_2CO_3 (green marks) of the 50-layer film, considering the concentration of Na^+.

6.7 Conclusion

The adsorption data acquired and discussed in Chapter 5 by experiments with $NaReO_4$, NaCl, Na_2SO_4 and Na_2CO_3 using the 35- and 50-layer films, were modelled with the well-studied Langmuir, Freundlich and Sips adsorption isotherms. It was found that the Sips isotherm, which consists of a combination of the Langmuir and Freundlich isotherms, produced the most accurate fit to the experimental data, suggesting multilayer-fashioned adsorption. However, the original hypothesis of the anion exchange, where ReO_4^- replaced NO_3^- as the counter anion in the MOF matrix was proved inappropriate leading to the conclusion that behaviour of the thin film contradicts that of the bulk crystals. Alteration of the MOF structure in the thin film is constrained since it is chemically tethered to the gold surface of the QCM, thus prohibiting the anion exchange process. Systematic analysis of the physicochemical parameters contained within the mathematical expression of the Sips model provided us with an insight about the nature and mechanism of the adsorption. It was shown that the values of the parameters were significantly similar for all the salts used in the adsorption experiments, indicating a common adsorbent. Thus, it was found that sodium cations were adsorbed into the film, probably through weak electrostatic interactions with the π-electrons of the bipyridine rings. Nevertheless, in order to confirm cation adsorption properties of the thin film, further work is needed, including experiments with other cations such as K^+, Li^+, Ca^{2+}. Furthermore, the adsorption data for the 50-layer film was not as consistent and reproducible as that of the 35-layer film. This is probably due to excessive damping of the crystal as a result of the increased thickness of the film and further work is also needed to verify this hypothesis.

CHAPTER 7

7 Conclusion and further work

Nuclear reprocessing sites such as Sellafield Ltd have a statutory requirement to monitor the radionuclide concentration in the groundwater on their site. Technetium-99 is a contaminant of significant importance, since it forms the extremely environmentally mobile pertechnetate ion (TcO_4^-). Its lack of natural occurrence means that early detection of Tc is crucial because it can help identify leaks of radioactive contaminants into the environment. However, the current methods of determination of Tc in environmental samples, using both radiometric and mass spectroscopic techniques, are time consuming and require expensive equipment. In addition, because of its low concentration in environmental samples, Tc must be first isolated form other matrix components that could interfere in the measurement, such as other β-emitters or isobaric nuclei like Ru. The purpose of this work was to develop a novel, real-time sensor for Tc based on a Quartz Crystal Microbalance, which can detect small changes of mass added to its surface. Thus, the work towards the development of a QCM sensor modified with Tc-selective materials including the TREN ligand, TEVA resin and Ag-4,4'-bipyridine MOF was presented.

Chapter 3 focused on the synthesis of a novel TREN derivative ligand. A multi-step chemical synthesis was used to the preparation of a novel tri-Boc protected ligand which was characterized by NMR, IR and mass spectrometry. The synthesis was challenging, and a small amount of material could be prepared. The subsequent Boc deprotection was attempted using well-established reaction conditions but ^{1}H NMR spectroscopic data did not conclusively show that the deprotection was successful without degradation of the rest of the molecular structure. Nevertheless, the product of the deprotection was deployed on a Quartz Crystal Microbalance as a SAM, unfortunately this did not lead to the measurement of a mass change and no detection of ReO_4^- was observed. This could be due to issues with the quality of the final product, very small frequency deviations resulting from only a small number of anions being accepted within the TREN derivative structure caused by the presence of only a single monolayer onto the crystal, or a decreased affinity for the target anion as a result of the modifications made to the base

TREN ligand. However, since TREN has been reported for the uptake of TcO_4^-, it is possible that a multilayer coating on the QCM of the original TREN ligands reported in the literature would offer a tool in the real time detection of TcO_4^-.

Given the challenges in producing appreciable amounts of the TREN ligand derivative, the time-consuming nature of this synthetic route and the uncertainty about the viability of this detection method using a QCM, it was decided to refocus the project to make use of other materials such as Teva resin and its active group, as presented in Chapter 4. In the first instance, an attempt was made to incorporate TEVA resin particles into a Aam/MBAAm hydrogel deposited directly onto the QCM. The swelling of the hydrogel as a result of the water absorption and concomitant increase in mass loading prevented its use as a useful QCM modification mechanism. For this reason, a novel derivative of the active component of TEVA resin, Aliquat-336, that can be tethered on the QCM through a SAM was prepared by multi-step chemical synthesis. The novel compound was fully characterized by ^1H NMR, ^{13}C NMR, IR and MS. The ligand was tethered to the QCM surface in a SAM but led to no detection of ReO_4^-. Estimation of maximum theoretical frequency changes resulting from the interaction of the crystal with the perrhenate ion revealed that the expected mass gained could be below the detection limit of the QCM equipment. This is a result of the small mass of the ion and the relatively large footprint of the Aliquat-336 derivative making up the SAM. However, since TEVA resin has been reported for the uptake of ReO_4^- and TcO_4^-, a more efficient coating on a QCM would have the potential to create an effective sensor. This could be achieved by use of much smaller TEVA resin particles in the range of nanometers (perhaps obtained via milling of the currently available 20-50 μm particles) immobilized as a multilayer coating within a matrix that is water permeable but does not swell to such a large extent as the hydrogel used in this work.

Considering the potential issues in using SAM-modified QCMs for the detection of ReO_4^- identified in Chapters 3 and 4, it was decided to explore multi-layered functionalized QCMs. Our efforts were then focused on the Ag-4,4-bipyridine metal-organic framework, as presented in Chapter 5, which has been reported for extensive perrhenate take up. Bulk crystals of the MOF were spin coated on the QCM surface and the sensor was exposed to ReO_4^-. Although the adsorption of ReO_4^- was confirmed, the coating became detached from the QCM when immersed into solution. Thus, it was decided to tether chemically the MOF onto the QCM surface in the form of a thin film. Films of 35-, 50-, 100- and 150-layers, were built layer-by-layer on a self-assembled monolayer of 4-mercaptopridine on the gold electrode of the QCM and was characterized with XRD and SEM. The XRD analysis showed that the molecular structure of the thin film is similar to that of the bulk crystals. However, the SEM analysis suggests that the morphology of the film in the microscale was substantially different than that of the bulk crystals, possibly because of the tethering of the film on the gold surface of the QCM.

The response of the 35- and 50-layer films in the presence of $NaReO_4$ as well as that of interferents such as NaCl, Na_2SO_4 and Na_2CO_3 was tested. It was shown that the response of the thin film MOF is different to that of the bulk crystals, since the adsorption was reversible in the case of the film. The thin film also showed little selective towards perrhenate, as both the 35 layers and 50 layers films respond similarly to all the analytes that they were tested with. However, there were some serious reproducibility issues with the 50 layers film, while the results of the 35 layers film proved to be more reproducible and with much smaller deviations.

The adsorption data acquired and discussed in Chapter 5 by experiments with $NaReO_4$, NaCl, Na_2SO_4 and Na_2CO_3 using the 35- and 50-layer films, were then modelled with the well-studied Langmuir, Freundlich and Sips adsorption isotherms, as described in Chapter 6, in order to understand the mechanism behind the adsorption in the Ag-4-4-bipyridine MOF. It was found that the Sips isotherm, which consists of a combination of the Langmuir and Freundlich isotherms, produced the most accurate fit to the experimental data, suggesting multilayer-fashioned adsorption. However, the original hypothesis of the anion exchange, where ReO_4^- replaced NO_3^- as the counter anion in the MOF matrix was proved inappropriate leading to the conclusion that the behaviour of the thin film contradicts that of the bulk crystals. Alteration of the MOF structure in the thin film is constrained since it is chemically tethered to the gold surface of the QCM, thus prohibiting the anion exchange process. Systematic analysis of the physicochemical parameters contained within the mathematical expression of the Sips model provided us with an insight on the nature and mechanism of the adsorption. It was shown that the values of the parameters were significantly similar for all the salts used in the adsorption experiments, indicating a common adsorbent. Thus, it was found that sodium cations were adsorbed into the film, probably through weak electrostatic interactions with the π-electrons of the bipyridine rings. Nevertheless, in order to confirm cation adsorption properties of the thin film, further work is needed, including experiments with other cations such as K^+, Li^+, Ca^{2+}. Furthermore, the adsorption data for the 50-layer film was not as consistent and reproducible as that of the 35-layer film. This is probably due to excessive damping of the crystal as a result of the increased thickness of the film and further work is also needed to verify this hypothesis. It would also be possible that as the film thickness grows away from the gold surface, the film may start to behave more similarly to the bulk crystals, but this may not be compatible with QCMs, since they can support films of limited thicknesses. However, concerning the detection of TcO_4^-, it seems that the efforts should be concentrated to the bulk crystals and to types of coating which would let them move and rearrange their structure freely.

Although the effective detection of ReO_4^- and consequently TcO_4^- were not successful, novel organic molecules and thin films were successfully synthesized and characterized in this work. It was proven that light molecules such as ReO_4^- cannot be detected by a single monolayer, while multilayered coatings have potential in anion and cation detection. It was also shown that the physicochemical and adsorptive properties of MOF bulk crystals are significantly different than that of their thin films, which potentially opens a new field of research.

CHAPTER 8

8 References

[1] S. B. Jenkinson, D. McCubbin, P. H. W. Kennedy, A. Dewar, R. Bonfield, and K. S. Leonard, “An estimate of the inventory of technetium-99 in the sub-tidal sediments of the Irish Sea,” *J Environ Radioact*, vol. 133, pp. 40–47, 2014, doi: 10.1016/j.jenvrad.2013.05.004.

[2] M. Simonsen *et al.*, “The impact of tidal and mesoscale eddy advection on the long term dispersion of99Tc from Sellafield,” *J Environ Radioact*, vol. 177, pp. 100–112, 2017, doi: 10.1016/j.jenvrad.2017.06.002.

[3] “*Groundwater Protection Guidelines for Nuclear Power Plants: Public Edition.* EPRI, Palo Alto, CA: 2008. 1016099,” 2008.

[4] “Groundwater monitoring at Sellafield: Annual Data review 2016, LQTD000758” 2016.

[5] H. G. Gorchev and G. Ozolins, “Guidelines for Drinking-water Quality,” *World Health Organisation, Third Edition*, 2004, doi: 10.1016/S1462-0758(00)00006-6.

[6] J. Hunter, “SCLS Phase 1-Conceptual model of contamination below ground at Sellafield,” 2004.

[7] “Environmental sampling and monitoring of groundwater, SLF2.13.10.01, Sellafield Ltd” 2015.

[8] K. Rengan, “Cerenkov counting technique for beta particles: advantages and limitations,” *J Chem Educ*, vol. 60, no. 8, p. 682, 1983, doi: 10.1021/ed060p682.

[9] “ANALYTICAL METHOD FOR THE DETERMINATION OF TOTAL ALPHA , BETA AND GAMMA SPECTROMETRY,” 2013.

[10] J. Mattauch, “Zur Systematik der Isotopen.,” *Z. Phys.*, pp. 361–371, 1934.

[11] C. Perrier and E. Segrè, “Some chemical properties of element 43. II,” *J Chem Phys*, vol. 5, pp. 712–716, 1937, doi: 10.1063/1.1750403.

[12] A. H. Meena and Y. Arai, “Environmental geochemistry of technetium,” *Environ Chem Lett*, vol. 15, no. 2, pp. 241–263, 2017, doi: 10.1007/s10311-017-0605-7.

[13] E. D. Davis and L. Hamdan, “The Oklo natural nuclear reactor,” *Sov. Phys. Usp*, vol. 20, p. 937, 1977.

[14] K. H. Lieser, “Technetium in the Nuclear Fuel Cycle, in Medicine and in the Environment,” *Radiochim Acta*, vol. 63, no. SI, pp. 5–8, 1993, doi: 10.1007/s13398-014-0173-7.2.

[15] N. N. Popova, I. G. Tananaev, S. I. Rovnyi, and B. F. Myasoedov, “Technetium: Behavior during reprocessing of spent nuclear fuel and in environmental objects,” *Russian Chemical Reviews*, vol. 72, no. 2, pp. 101–121, 2003, doi: 10.1070/RC2003v072n02ABEH000785.

[16] J. P. Icenhower, N. P. Qafoku, J. M. Zachara, and W. J. Martin, “The biogeochemistry of technetium: A review of the behavior of an artificial element in the natural environment,” *Am J Sci*, vol. 310, no. 8, pp. 721–752, 2010, doi: 10.2475/08.2010.02.

[17] J. A. Rard, “Current status of the thermodynamic data for Technetium and its compounds and aqueous species,” *Journal of Nuclear and Radiochemical Sciences*, vol. 6, no. 3, pp. 197–204, 2005, doi: 10.14494/jnrs2000.6.3_197.

[18] J. M. Mckibben, “Chemistry of the Purex Process,” *Radiochim Acta*, vol. 36, pp. 3–15, 1984, doi: 10.1524/ract.1984.36.12.3.

[19] A. P. Paiva and P. Malik, “Recent advances on the chemistry of solvent extraction applied to the reprocessing of spent nuclear fuels and radioactive wastes,” *J Radioanal Nucl Chem*, vol. 261, no. 2, pp. 485–496, 2004.

[20] K. George, A. J. Masters, F. R. Livens, M. J. Sarsfield, R. J. Taylor, and C. A. Sharrad, “A review of technetium and zirconium extraction into tributyl phosphate in the PUREX process,” *Hydrometallurgy*, vol. 211. Elsevier B.V., May 01, 2022. doi: 10.1016/j.hydromet.2022.105892.

[21] M. Khan and W. Um, “Liquid Scintillation Counting Methodology for ^{99}Tc Analysis: A Remedy for Radiopharmaceutical Waste,” *Anal Chem*, vol. 87, no. 17, pp. 9054–9060, 2015, doi: 10.1021/acs.analchem.5b02279.

[22] N. Guérin, A. Gagné, and S. Kramer-Tremblay, “A rapid method for the routine monitoring of 99Tc by liquid scintillation counting,” *J Radioanal Nucl Chem*, vol. 314, no. 3, pp. 2009–2017, 2017, doi: 10.1007/s10967-017-5552-z.

[23] X. Hou and P. Roos, “Critical comparison of radiometric and mass spectrometric methods for the determination of radionuclides in environmental, biological and nuclear waste samples,” *Anal Chim Acta*, vol. 608, no. 2, pp. 105–139, 2008, doi: 10.1016/j.aca.2007.12.012.

[24] K. Rengan, “Cerenkov Counting Technique for Beta Particles: Advantages and Limitations,” 1983.

[25] K. Shi, X. Hou, P. Roos, and W. Wu, “Determination of technetium-99 in environmental samples: A review,” *Anal Chim Acta*, vol. 709, pp. 1–20, 2012, doi: 10.1016/j.aca.2011.10.020.

[26] F. Wigley, P. E. Warwick, I. W. Croudace, J. Caborn, and A. L. Sanchez, “Optimised method for the routine determination of Technetium-99 in environmental samples by liquid scintillation counting,” *Anal Chim Acta*, no. 380, pp. 73–82, 1999.

[27] G. Steinhauser and K. Buchtela, *Gas ionization detectors*, vol. 1. Elsevier Inc., 2020. doi: 10.1016/B978-0-12-814397-1.00002-9.

[28] N. Matsuoka, T. Umata, M. Okamura, N. Shiraishi, N. Momoshima, and Y. Takashima, “Determination of technetium-99 from the aspect of environmental

radioactivity," *Journal of Radioanalytical and Nuclear Chemistry Articles*, vol. 140, no. 1, pp. 57–73, 1990, doi: 10.1007/BF02037364.

[29] Q. Chen, H. Dahlgaard, and S. P. Nielsen, "Determination of 99Tc in sea water ata ultra low levels," *Anal. Chim. Acta*, vol. 285, pp. 177–180, 1994.

[30] V. Foti, S; Delucchi, E; Akamian, "Determination of picogram amounts of technetium in environmental samples by neutron activation analysis," *Anal Chim Acta*, 1971.

[31] J. L. Mas, M. García-León, and J. P. Bolívar, "99 Tc detection in water samples by ICP-MS," *Radiochim Acta*, vol. 92, no. 1–2004, pp. 39–46, 2004, doi: 10.1524/ract.92.1.39.25403.

[32] a. Bartošová, P. Rajec, and a. Klimeková, "Determination of technetium-99 in soils and radioactive wastes using ICP-MS," *Chemical Papers*, vol. 60, no. 2, pp. 125–131, 2006, doi: 10.2478/s11696-006-0023-y.

[33] K. Shi, J. Qiao, W. Wu, P. Roos, and X. Hou, "Rapid Determination of Technetium-99 in Large Volume Seawater Samples Using Sequential Injection Extraction Chromatographic Separation and ICP-MS Measurement," *Anal Chem*, vol. 84, pp. 6783–6789, 2012.

[34] L. Wacker, L. K. Fifield, and S. G. Tims, "Developments in AMS of99Tc," *Nuclear Instruments and Methods in Physics Research B*, vol. 223–224, pp. 185–189, 2004, doi: 10.1016/j.nimb.2004.04.038.

[35] R. G. ; H. P. P. Fifield, L K; Carling, R.S.; Cresswell, "Accelerator mass spectrometry of 99Tc," *Nuclear Instruments and Methods in Physics Research B*, no. 168, pp. 427–436, 2000.

[36] S. K. Aggarwal, "Thermal ionisation mass apectrometry (TIMS) in nuclear science and technology – a review," *Analytical Methods*, no. 8, pp. 942–957, 2016, doi: 10.1039/C5AY02816G.

[37] D. J. Rokop, N. C. Schroeder, and K. Wolfsberg, "Mass Spectrometry of Technetium at the Subpicogram Level," no. 13, pp. 1271–1274, 1990.

[38] B. N. Trautmann, "Ultratrace Analysis of Technetium," *Radiochim Acta*, no. 63, pp. 37–43, 1993.

[39] S. W. Downey and N. S. Nogar, "Resonance ionization mass spectrometry of technetium," *International journal of Mass Spectrometry and Ion Process*, no. 61, pp. 337–345, 1984.

[40] K. Shi, X. Hou, P. Roos, and W. Wu, "Determination of technetium-99 in environmental samples: A review," *Anal Chim Acta*, vol. 709, pp. 1–20, 2012, doi: 10.1016/j.aca.2011.10.020.

[41] J. C. Butterworth, F. R. Livens, and P. R. Makinson, "Development of a method for the determination of low levels of technetium-99," vol. 174, pp. 293–300, 1995.

[42] J. H. Chao, C. L. Tseng, and C. J. Lee, “Sequential extraction separation for determination of technetium-99 in radwastes by ICP-MS,” vol. 251, no. 1, pp. 105–112, 2002.

[43] B. R. Harvey, R. D. Ibbett, K. J. Williams, and M. B. Lovett, “The Determination of Technetium-99 in Environmental Materials,” *Aquatic Environmet Protection: Analytical Methods*, vol. 8, pp. 1–22, 1991.

[44] J. H. P. Watson and D. C. Ellwood, “The removal of the pertechnetate ion and actinides from radioactive waste streams at Hanford, Washington, USA and Sellafield, Cumbria, UK: The role of iron-sulfide-containing adsorbent materials,” *Nuclear Engineering and Design*, vol. 226, no. 3, pp. 375–385, 2003, doi: 10.1016/S0029-5493(03)00194-8.

[45] J. Holm, E.; Rioseco, “Determination of 99Tc in environmental samples,” *Nuclear Instruments and Methods in Physics Research B*, vol. 223, pp. 204–207, 1984.

[46] Ihsanullah, “Methods for the Separation of Technetium from Ruthenium for Inductively Coupled Plasma-Mass Spectrometry,” *Sep Sci Technol*, vol. 29, no. 6, pp. 781–797, 1994, doi: 10.1080/01496399408005608.

[47] R. Schurhammer and G. Wip, “Liquid - Liquid Extraction of Pertechnetic Acid (Tc VII) by Tri- n -butyl Phosphate : Where Is the Proton ? A Molecular Dynamics Investigation,” *J Phys Chem*, vol. 115, pp. 2338–2348, 2011.

[48] K. Watanabe S., Hashimoto, “Solvent extraction of technetium in urine with TBP,” *J Radioanal Nucl Chem*, vol. 201, no. 5, pp. 361–370, 1995.

[49] N. W. Golchert and J. Sedlet, “Radiochemical Determination of Technetium-99 in Environmental Water Samples,” *Anal Chem*, vol. 41, pp. 669–671, 1969.

[50] Q. Chen, H. Dahlgaard, H. J. M. Hansen, and A. Aarkrog, “Determination of 99Tc in environmental samples by anion exchange and liquid-liquid extraction at controlled valency,” *Anal Chim Acta*, vol. 228, pp. 163–167, 1990.

[51] S. Morita, C. K. Kim, Y. Takaku, R. Seki, and N. Ikeda, “Determination of Technetium-99 in Environmental Samples by Inductively Coupled Plasma Mass Spectrometry,” *Applied Radiation and Isotopes*, vol. 42, no. 6, pp. 531–534, 1991.

[52] K. Tagami and S. Uchida, “Comparison of the TEVA-Spec resin and liquid-liquid extraction methods for the separation of technetium in soil samples,” *J Radioanal Nucl Chem*, vol. 239, no. 3, pp. 643–648, 1999.

[53] P. Rajec *et al.*, “Preparation and characterization of adsorbent based on carbon for pertechnetate adsorption,” *J Radioanal Nucl Chem*, vol. 303, no. 1, pp. 277–286, 2015, doi: 10.1007/s10967-014-3303-y.

[54] Y. Wang, H. Gao, R. Yeredla, H. Xu, and M. Abrecht, “Control of pertechnetate sorption on activated carbon by surface functional groups,” *J Colloid Interface Sci*, vol. 305, no. 2, pp. 209–217, 2007, doi: 10.1016/j.jcis.2006.09.056.

[55] B. Gu, K. E. Dowlen, L. Liang, and J. L. Clausen, "Efficient separation and recovery of technetium-99 from contaminated groundwater," *Separations Technology*, vol. 6, no. 2, pp. 123–132, 1996, doi: 10.1016/0956-9618(96)00147-6.

[56] E. Holm, T. Gäfvert, P. Lindahl, and P. Roos, "In situ sorption of technetium using activated carbon," *Applied Radiation and Isotopes*, vol. 53, no. 1–2, pp. 153–157, 2000, doi: 10.1016/S0969-8043(00)00127-5.

[57] B. Remenec, S. Dulanská, V. Paučová, and L. Mátel, "Determination of 99Tc in evaporator concentrates using solid phase extraction techniques," *J Radioanal Nucl Chem*, vol. 290, no. 2, pp. 403–407, 2011, doi: 10.1007/s10967-011-1354-x.

[58] V. Paučová, B. Remenec, S. Dulanská, Ľ. Mátel, and M. Prekstová, "Determination of 99Tc in soil samples using molecular recognition technology product AnaLig® Tc-02 gel," *J Radioanal Nucl Chem*, vol. 293, no. 2, pp. 675–677, 2012, doi: 10.1007/s10967-012-1710-5.

[59] A. E. Eroglu, C. W. Mcleod, K. S. Leonard, and D. Mccubbin, "Determination of technetium in sea-water using ion exchange and inductively coupled plasma mass spectrometry with ultrasonic nebulisation," *J Anal At Spectrom*, vol. 13, no. September, pp. 875–878, 1998.

[60] E. P. Horwitz, M. L. Dietz, R. Chiarizia, H. Diamond, S. L. Maxwell, and M. R. Nelson, "Separation and Preconcentration of Actinides by Extraction Chromatography Using a Supported Liquid Anion-Exchanger - Application to the Characterization of High-Level Nuclear Waste Solutions," *Anal Chim Acta*, vol. 310, no. 1, pp. 63–78, 1995, doi: 10.1016/0003-2670(95)00144-O.

[61] Z. lu Zhang, G. qing Zhou, J. feng Lin, Y. Ma, and X. wei Yi, "Preconcentration and separation of99Tc in groundwater by using TEVA resin," *J Radioanal Nucl Chem*, vol. 314, no. 1, pp. 161–166, 2017, doi: 10.1007/s10967-017-5425-5.

[62] K. H. Chung, S. do Choi, G. S. Choi, and M. J. Kang, "Design and performance of an automated radionuclide separator: Its application on the determination of 99Tc in groundwater," *Applied Radiation and Isotopes*, vol. 81, pp. 57–61, 2013, doi: 10.1016/j.apradiso.2013.03.080.

[63] P. E. Warwick and I. W. Croudace, "Rapid on-site radionuclide screening of aqueous waste streams using dip-stick technologies and liquid scintillation counting," *J Radioanal Nucl Chem*, vol. 314, no. 2, pp. 761–766, 2017, doi: 10.1007/s10967-017-5413-9.

[64] S. Uchida and K. Tagami, "Separation and concentration of technetium using a Tc-selective extraction chromatographic resin," *J Radioanal Nucl Chem*, vol. 221, pp. 35–39, 1997.

[65] D. Banerjee, D. Kim, M. J. Schweiger, A. A. Kruger, and P. K. Thallapally, "Removal of TcO_4^- ions from solution: materials and future outlook," *Chem. Soc. Rev.*, vol. 45, no. 10, pp. 2724–2739, 2016, doi: 10.1039/C5CS00330J.

[66] Y. Wang and H. Gao, "Compositional and structural control on anion sorption capability of layered double hydroxides (LDHs)," *J Colloid Interface Sci*, vol. 301, pp. 19–26, 2006, doi: 10.1016/j.jcis.2006.04.061.

[67] S. Wang *et al.*, "Selectivity, kinetics, and efficiency of reversible anion exchange with TcO 4 - in a supertetrahedral cationic framework," *Adv Funct Mater*, vol. 22, no. 11, pp. 2241–2250, 2012, doi: 10.1002/adfm.201103081.

[68] S. Wang *et al.*, "NDTB-1: A supertetrahedral cationic framework that removes TcO 4- from solution," *Angewandte Chemie - International Edition*, vol. 49, no. 6, pp. 1057–1060, 2010, doi: 10.1002/anie.200906397.

[69] R. A. Leonard *et al.*, "DEVELOPING AND TESTING AN ALKALINE-SIDE SOLVENT EXTRACTION PROCESS FOR TECHNETIUM SEPARATION FROM TANK WASTE," *Sep Sci Technol*, vol. 34, pp. 1043–1068, 1999, doi: 10.1080/01496399908951080.

[70] P. D. Beer, P. K. Hopkins, and J. D. McKinney, "Cooperative halide, perrhenate anion-sodium cation binding and pertechnetate extraction and transport by a novel tripodal tris(amido benzo-15-crown-5) ligand," *Chemical Communications*, no. 13, pp. 1253–1254, 1999, doi: 10.1039/A903440D.

[71] R. Alberto, G. Bergamaschi, H. Braband, T. Fox, and V. Amendola, "99TcO4-: Selective recognition and trapping in aqueous solution," *Angewandte Chemie - International Edition*, vol. 51, no. 39, pp. 9772–9776, 2012, doi: 10.1002/anie.201205313.

[72] D. Zacher, R. Schmid, C. Wöll, and R. A. Fischer, "Surface chemistry of metal-organic frameworks at the liquid-solid interface," *Angewandte Chemie - International Edition*, vol. 50, no. 1, pp. 176–199, 2011, doi: 10.1002/anie.201002451.

[73] N. A. Khan, Z. Hasan, and S. H. Jhung, "Adsorptive removal of hazardous materials using metal-organic frameworks (MOFs): A review," *J Hazard Mater*, vol. 244–245, pp. 444–456, 2013, doi: 10.1016/j.jhazmat.2012.11.011.

[74] L. Heinke and C. Wöll, "Surface-Mounted Metal–Organic Frameworks: Crystalline and Porous Molecular Assemblies for Fundamental Insights and Advanced Applications," *Advanced Materials*, vol. 31, no. 26, 2019, doi: 10.1002/adma.201806324.

[75] K. Sumida *et al.*, "Carbon Dioxide Capture in Metal À Organic Frameworks," *Chem Rev*, vol. 112, pp. 724–781, 2012.

[76] P. D. C. Dietzel, V. Besikiotis, and R. Blom, "Application of metal – organic frameworks with coordinatively unsaturated metal sites in storage and separation of methane and carbon dioxide †," *J Mater Chem*, vol. 19, pp. 7362–7370, 2009, doi: 10.1039/b911242a.

[77] F. Ke, L. Qiu, Y. Yuan, F. Peng, X. Jiang, and A. Xie, "Thiol-functionalization of metal-organic framework by a facile coordination-based postsynthetic strategy and

enhanced removal of Hg 2 + from water," *J Hazard Mater*, vol. 196, pp. 36–43, 2011, doi: 10.1016/j.jhazmat.2011.08.069.

[78] B. Zhu *et al.*, "Iron and 1 , 3 , 5-Benzenetricarboxylic Metal − Organic Coordination Polymers Prepared by Solvothermal Method and Their Application in E ffi cient As (V) Removal from Aqueous Solutions," *J Phys Chem*, vol. 116, 2012.

[79] I. R. Colinas, R. C. Silva, and S. R. J. Oliver, "Reversible, Selective Trapping of Perchlorate from Water in Record Capacity by a Cationic Metal-Organic Framework," *Environ Sci Technol*, vol. 50, no. 4, pp. 1949–1954, 2016, doi: 10.1021/acs.est.5b03455.

[80] L. Zhu *et al.*, "Exceptional perrhenate/pertechnetate uptake and subsequent immobilization by a low-dimensional cationic coordination polymer: Overcoming the hofmeister bias selectivity," *Environ Sci Technol Lett*, vol. 4, no. 7, pp. 316–322, 2017, doi: 10.1021/acs.estlett.7b00165.

[81] A. Manbachi and R. S. C. Cobbold, "Development and application of piezoelectric materials for ultrasound generation and detection," *Ultrasound*, vol. 19, pp. 187–196, 2011, doi: 10.1258/ult.2011.011027.

[82] A. Alassi, M. Benammar, and D. Brett, "Quartz crystal microbalance electronic interfacing systems: A review," *Sensors (Switzerland)*, vol. 17, no. 12, pp. 1–41, 2017, doi: 10.3390/s17122799.

[83] G. Sauerbrey, "Verwendung von Schwingquarzen zur Wägung dünner Schichten und zur Mikrowägung," *Zeitschrift für Physik*, vol. 155, no. 2, pp. 206–222, 1959, doi: 10.1007/BF01337937.

[84] Y. Xue, X. Li, H. Li, and W. Zhang, "Quantifying thiol-gold interactions towards the efficient strength control," *Nat Commun*, vol. 5, pp. 1–9, 2014, doi: 10.1038/ncomms5348.

[85] C. I. Cheng, Y.-P. Chang, and Y.-H. Chu, "Biomolecular interactions and tools for their recognition : focus on the quartz crystal microbalance and its diverse surface chemistries and applications," *Chem. Soc. Rev.*, vol. 41, pp. 1947–1971, 2012, doi: 10.1039/c1cs15168a.

[86] Z. Fu and G. Xu, "Crystalline, Highly Oriented MOF Thin Film: the Fabrication and Application," *Chemical Record*, vol. 17, no. 5, pp. 518–534, 2017, doi: 10.1002/tcr.201600109.

[87] J. Liu and C. Wöll, "Surface-supported metal-organic framework thin films: Fabrication methods, applications, and challenges," *Chem Soc Rev*, vol. 46, no. 19, pp. 5730–5770, 2017, doi: 10.1039/c7cs00315c.

[88] Z. Wang and C. Wöll, "Fabrication of Metal – Organic Framework Thin Films Using Programmed Layer-by-Layer Assembly Techniques," vol. 1800413, pp. 1–22, 2019, doi: 10.1002/admt.201800413.

[89] O. Shekhah, J. Liu, R. A. Fischer, and C. Wöll, “MOF thin films: Existing and future applications,” *Chem Soc Rev*, vol. 40, no. 2, pp. 1081–1106, 2011, doi: 10.1039/c0cs00147c.

[90] V. Stavila, J. Volponi, A. M. Katzenmeyer, M. C. Dixon, and M. D. Allendorf, “Kinetics and mechanism of metal-organic framework thin film growth: Systematic investigation of HKUST-1 deposition on QCM electrodes,” *Chem Sci*, vol. 3, no. 5, pp. 1531–1540, 2012, doi: 10.1039/c2sc20065a.

[91] E. Biemmi, C. Scherb, and T. Bein, “Oriented Growth of the Metal Organic Framework Cu 3 (BTC) 2 (H 2 O) 3 , xH 2 O Tunable with Functionalized Self-Assembled Monolayers,” *J Am Chem Soc*, vol. 3, pp. 8054–8055, 2007.

[92] D. Y. Lee, E. Kim, Y. Shin, D. V Shinde, and W. Lee, “Layer-bylayer deposition and photovoltaic property of Ru-based metal – organic frameworks,” *RSC Adv*, vol. 4, pp. 12037–12042, 2014, doi: 10.1039/c4ra00397g.

[93] K. Otsubo, T. Haraguchi, O. Sakata, A. Fujiwara, and H. Kitagawa, “Step-by-step fabrication of a highly oriented crystalline three-dimensional pillared-layer-type metal-organic framework thin film confirmed by synchrotron X-ray diffraction,” *J Am Chem Soc*, vol. 134, no. 23, pp. 9605–9608, 2012, doi: 10.1021/ja304361v.

[94] S. Sakaida *et al.*, “Crystalline coordination framework endowed with dynamic gate-opening behaviour by being downsized to a thin film,” *Nat Chem*, no. March, pp. 1–7, 2016, doi: 10.1038/nchem.2469.

[95] B. Liu, M. Tu, and R. A. Fischer, “Metal – Organic Framework Thin Films : Crystallite Orientation Dependent Adsorption,” vol. 52, pp. 3402–3405, 2013, doi: 10.1002/anie.201207908.

[96] K. Sadman, C. G. Wiener, R. A. Weiss, C. C. White, K. R. Shull, and B. D. Vogt, “Quantitative Rheometry of Thin Soft Materials Using the Quartz Crystal Microbalance with Dissipation,” *Anal Chem*, vol. 90, no. 6, pp. 4079–4088, 2018, doi: 10.1021/acs.analchem.7b05423.

[97] H. Jean, T. Saha, T. Tey, W. Siang, and C. Wei, “Quartz crystal microbalance-based biosensors as rapid diagnostic devices for infectious diseases,” *Biosens Bioelectron*, vol. 168, p. 112513, 2020, doi: 10.1016/j.bios.2020.112513.

[98] M. Menger, H. B. Yildiz, A. Yarman, J. Erd, and F. Scheller, “MIPs and Aptamers for Recognition of Proteins in Biomimetic Sensing,” *Biosensors (Basel)*, vol. 6, no. 3, p. 35, 2016, doi: 10.3390/bios6030035.

[99] K. Novoselov *et al.*, “Electric Field Effect in Atomically Thin Carbon Films,” *Science (1979)*, vol. 306, no. October, pp. 666–670, 2004.

[100] C. Mattevi and M. Chhowalla, “A review of chemical vapour deposition of graphene on copper,” *J Mater Chem*, vol. 21, no. 10, pp. 3324–3334, 2011, doi: 10.1039/c0jm02126a.

[101] V. Van Quang, V. Ngoc, L. Anh, V. Ngoc, T. Quang, and N. Van Quy, "Graphene-coated quartz crystal microbalance for detection of volatile organic compounds at room temperature," *Thin Solid Films*, vol. 568, pp. 6–12, 2014, doi: 10.1016/j.tsf.2014.07.036.

[102] F. Fauzi, A. Rianjanu, I. Santoso, and K. Triyana, "Gas and humidity sensing with quartz crystal microbalance (QCM) coated with graphene-based materials – A mini review," *Sens Actuators A Phys*, vol. 330, p. 112837, 2021, doi: 10.1016/j.sna.2021.112837.

[103] R. Perez, C. E. Ayala, J. Park, J. Choi, and I. Warner, "Coating-Based Quartz Crystal Microbalance Detection Methods of Environmentally Relevant Volatile Organic Compounds," *Chemosensors*, no. 7, p. 153, 2021.

[104] I. A. Koshets, Z. I. Kazantseva, Y. M. Shirshov, S. A. Cherenok, and V. I. Kalchenko, "Calixarene films as sensitive coatings for QCM-based gas sensors," *Sensors and Actuators B*, vol. 106, pp. 177–181, 2005, doi: 10.1016/j.snb.2004.05.054.

[105] S. Öztürk, A. Kösemen, Z. Alpaslan, N. Kılınc, Z. Z. Öztürk, and M. Penza, "Electrochemically growth of Pd doped ZnO nanorods on QCM for room temperature VOC sensors," *Sensors and Actuators B*, vol. 222, pp. 280–289, 2016, doi: 10.1016/j.snb.2015.08.083.

[106] S. I. Boyadjiev *et al.*, "Characterization of PLD grown WO3 thin films for gas sensing," *Appl Surf Sci*, vol. 417, pp. 218–223, 2017, doi: 10.1016/j.apsusc.2017.03.212.

[107] S. K. Vashist and P. Vashist, "Recent advances in quartz crystal microbalance-based sensors," *J Sens*, 2011, doi: 10.1155/2011/571405.

[108] M. Hussain, K. Kotova, and P. A. Lieberzeit, "Molecularly imprinted polymer nanoparticles for formaldehyde sensing with QCM," *Sensors (Switzerland)*, vol. 16, no. 7, Jul. 2016, doi: 10.3390/s16071011.

[109] F. Temel, E. Ozcelik, A. G. Ture, and M. Tabakci, "Sensing abilities of functionalized calix[4]arene coated QCM sensors towards volatile organic compounds in aqueous media," *Appl Surf Sci*, vol. 412, pp. 238–251, Aug. 2017, doi: 10.1016/j.apsusc.2017.03.258.

[110] C. Y. Huang, M. Song, Z. Y. Gu, H. F. Wang, and X. P. Yan, "Probing the adsorption characteristic of metal-organic framework MIL-101 for volatile organic compounds by quartz crystal microbalance," *Environ Sci Technol*, vol. 45, no. 10, pp. 4490–4496, 2011, doi: 10.1021/es200256q.

[111] V. van Quang, V. N. Hung, L. A. Tuan, V. N. Phan, T. Q. Huy, and N. van Quy, "Graphene-coated quartz crystal microbalance for detection of volatile organic compounds at room temperature," *Thin Solid Films*, vol. 568, no. 1, pp. 6–12, 2014, doi: 10.1016/j.tsf.2014.07.036.

[112] P. Qi, Z. Wang, R. Wang, Y. Xu, and T. Zhang, “Studies on QCM-type NO2 gas sensor based on graphene composites at room temperature,” *Chem Res Chin Univ*, vol. 32, no. 6, pp. 924–928, Dec. 2016, doi: 10.1007/s40242-016-6129-z.

[113] N. van Quy, V. A. Minh, N. van Luan, V. N. Hung, and N. van Hieu, “Gas sensing properties at room temperature of a quartz crystal microbalance coated with ZnO nanorods,” *Sens Actuators B Chem*, vol. 153, no. 1, pp. 188–193, Mar. 2011, doi: 10.1016/j.snb.2010.10.030.

[114] S. Muraoka, Y. Kiyohara, H. Oue, and S. Higashimoto, “A CO2 sensor using a quartz crystal microbalance coated with a sensitive membrane,” *Electronics and Communications in Japan*, vol. 97, no. 2, pp. 60–66, 2014, doi: 10.1002/ecj.11601.

[115] J. Devkota, K. J. Kim, P. R. Ohodnicki, J. T. Culp, D. W. Greve, and J. W. Lekse, “Zeolitic imidazolate framework-coated acoustic sensors for room temperature detection of carbon dioxide and methane,” *Nanoscale*, vol. 10, no. 17, pp. 8075–8087, May 2018, doi: 10.1039/c7nr09536h.

[116] Z. Cao, J. Guo, X. Fan, J. Xu, Z. Fan, and B. Du, “Detection of heavy metal ions in aqueous solution by P(MBTVBC-co-VIM)- coated QCM sensor,” *Sens Actuators B Chem*, vol. 157, no. 1, pp. 34–41, Sep. 2011, doi: 10.1016/j.snb.2011.03.023.

[117] L. Sartore, M. Barbaglio, L. Borgese, and E. Bontempi, “Polymer-grafted QCM chemical sensor and application to heavy metal ions real time detection,” *Sens Actuators B Chem*, vol. 155, no. 2, pp. 538–544, Jul. 2011, doi: 10.1016/j.snb.2011.01.003.

[118] H. Lou *et al.*, “The real-time detection of trace-level Hg 2+ in water by QCM loaded with thiol-functionalized SBA-15,” *Sens Actuators B Chem*, vol. 166–167, pp. 246–252, May 2012, doi: 10.1016/j.snb.2012.02.053.

[119] H. Eun and Y. Umezawa, “Sulfate ion sensing based on a quartz-crystal microbalance immobilized with barium sulfate crystals grown on a self-assembled monolayer of phosphorylated 11-mercapto-1-undecanol.”

[120] D. D. Erbahar, I. Gürol, F. Zelder, and M. Harbeck, “Anion sensing with cobalt corrinoid grafted quartz crystal microbalances,” *Sens Actuators B Chem*, vol. 207, no. Part A, pp. 297–302, 2015, doi: 10.1016/j.snb.2014.10.073.

[121] T. Y. Lin, C. H. Hu, and T. C. Chou, “Determination of albumin concentration by MIP-QCM sensor,” in *Biosensors and Bioelectronics*, Jul. 2004, vol. 20, no. 1, pp. 75–81. doi: 10.1016/j.bios.2004.01.028.

[122] F. Kartal, D. Çimen, N. Bereli, and A. Denizli, “Molecularly imprinted polymer based quartz crystal microbalance sensor for the clinical detection of insulin,” *Materials Science and Engineering C*, vol. 97, no. December 2018, pp. 730–737, 2019, doi: 10.1016/j.msec.2018.12.086.

[123] J. Luo, Q. Zhang, Y. Huang, G. Liu, and R. Zhao, “Quartz crystal microbalance biosensor for recombinant human interferon-β detection based on antisense

peptide approach," *Anal Chim Acta*, vol. 590, no. 1, pp. 91–97, May 2007, doi: 10.1016/j.aca.2007.03.022.

[124] E. Kim and J. Boulègue, "Chemistry of rhenium as an analogue of technetium: Experimental studies of the dissolution of rhenium oxides in aqueous solutions," *Radiochim Acta*, vol. 91, no. 4, pp. 211–216, 2003, doi: 10.1524/ract.91.4.211.19968.

[125] J. G. Darab and P. A. Smith, "Chemistry of technetium and rhenium species during low-level radioactive waste vitrification," *Chemistry of Materials*, vol. 8, no. 5, pp. 1004–1021, 1996, doi: 10.1021/cm950418+.

[126] E. a Katayev, G. v Kolesnikov, and J. L. Sessler, "Molecular recognition of pertechnetate and perrhenate," *Chem Soc Rev*, vol. 38, no. 6, p. 1572, 2009, doi: 10.1039/b806468g.

[127] S. Sarri, P. Misaelides, D. Zamboulis, X. Gaona, M. Altmaier, and H. Geckeis, "Rhenium(VII) and technetium(VII) separation from aqueous solutions using a polyethylenimine–epichlorohydrin resin," *J Radioanal Nucl Chem*, vol. 307, no. 1, pp. 681–689, 2016, doi: 10.1007/s10967-015-4213-3.

[128] H. Stephan *et al.*, "Binding and Extraction of Pertechnetate and Perrhenate by Azacages," in *Fundamentals and Applications of Anion Separations*, Boston, MA: Springer US, 2004, pp. 151–168. doi: 10.1007/978-1-4419-8973-4_10.

[129] J. Y. C. Lim and P. D. Beer, "Superior perrhenate anion recognition in water by a halogen bonding acyclic receptor," *Chemical Communications*, vol. 51, no. 17, pp. 3686–3688, 2015, doi: 10.1039/C4CC10130H.

[130] J. A. Gawenis, K. T. Holman, J. L. Atwood, and S. S. Jurisson, "Extraction of pertechnetate and perrhenate from water with deep-cavity [CpFe(arene)]+-derivatized cyclotriveratrylenes," *Inorg Chem*, vol. 41, no. 23, pp. 6028–6031, 2002, doi: 10.1021/ic0202312.

[131] S. P. Cornes, M. R. Sambrook, and P. D. Beer, "Selective perrhenate recognition in pure water by halogen bonding and hydrogen bonding alpha-cyclodextrin based receptors," *Chem. Commun.*, vol. 53, no. 27, pp. 3866–3869, 2017, doi: 10.1039/C7CC01605K.

[132] A. Papageorgiou and F. Andrieux, "Adsorptive Behaviour of a Novel Ag-4,4-bipyridine Metal Organic Framework Thin Film Tethered to a Quartz Crystal Microbalance," *J Electrochem Soc*, vol. 168, no. 11, p. 117502, Nov. 2021, doi: 10.1149/1945-7111/ac315f.

[133] W. W. Sleator, "The Faraday Laws of Electrolysis," *Am J Phys*, vol. 9, no. 3, pp. 166–168, Jun. 1941, doi: 10.1119/1.1991660.

[134] W. H. Bragg, W. L. Bragg Apr, B. W. H Bragg, and C. Professor of Physics, "The Reflection o f X-rays by Crystals." [Online]. Available: https://royalsocietypublishing.org/

[135] J. I. Goldstein *et al.*, *Scanning Electron Microscopy and X-ray Microanalysis*. Boston, MA: Springer US, 2003. doi: 10.1007/978-1-4615-0215-9.

[136] J. Roberts, *Nuclear Magnetic Resonance, Applictions to organic Chemistry*. McGraw-Hill Book Company, Inc, 1959.

[137] R. Alberto, G. Bergamaschi, H. Braband, T. Fox, and V. Amendola, "99TcO 4-: Selective recognition and trapping in aqueous solution," *Angewandte Chemie - International Edition*, vol. 51, no. 39, pp. 9772–9776, 2012, doi: 10.1002/anie.201205313.

[138] N. Ghanem, J. Martinez, and D. Stien, "Quaternary Ammonium-Supported Scavenger Reagents for Acids and Electrophiles," *European J Org Chem*, no. 1, pp. 84–89, 2004, doi: 10.1002/ejoc.200300403.

[139] F. Goursaud *et al.*, "Glycine betaine as a renewable raw material to 'greener' new cationic surfactants," *Green Chemistry*, vol. 10, no. 3, pp. 318–328, 2008, doi: 10.1039/b713429k.

[140] T. Le Gall *et al.*, "Effects of a novel archaeal tetraether-based colipid on the in vivo gene transfer activity of two cationic amphiphiles," *Mol Pharm*, vol. 11, no. 9, pp. 2973–2988, 2014, doi: 10.1021/mp4006276.

[141] A. Leggio *et al.*, "One-pot synthesis of amides from carboxylic acids activated using thionyl chloride," *RSC Adv*, vol. 6, no. 41, pp. 34468–34475, 2016, doi: 10.1039/c5ra24527c.

[142] N. Srinivasan, A. Yurek-george, and A. Ganesan, "Rapid deprotection of N -Boc amines by TFA combined with freebase generation using basic ion-exchange resins," *Mol Divers*, vol. 9, pp. 291–293, 2005, doi: 10.1007/s11030-005-4386-8.

[143] M. Sun, L. Yang, P. Jose, L. Wang, and J. Zweit, "Functionalization of quantum dots with multidentate zwitterionic ligands: Impact on cellular interactions and cytotoxicity," *J Mater Chem B*, vol. 1, no. 44, pp. 6137–6146, 2013, doi: 10.1039/c3tb20894j.

[144] Z. Li, T. Niu, Z. Zhang, G. Feng, and S. Bi, "Studies on the effect of solvents on self-assembly of thioctic acid and Mercaptohexanol on gold," *Thin Solid Films*, vol. 519, no. 13, pp. 4225–4233, 2011, doi: 10.1016/j.tsf.2011.02.065.

[145] S. Buchatip, C. Ananthanawat, P. Sithigorngul, P. Sangvanich, S. Rengpipat, and V. P. Hoven, "Detection of the shrimp pathogenic bacteria, Vibrio harveyi, by a quartz crystal microbalance-specific antibody based sensor," *Sens Actuators B Chem*, vol. 145, no. 1, pp. 259–264, 2010, doi: 10.1016/j.snb.2009.12.003.

[146] E. Temba, S. Reis, and J. Geraldo, "Separation and determination of the difficult-to-measure radionuclide 99 Tc in radioactive wastes from nuclear power plants by using extraction chromatography and radiometric techniques," *J Radioanal Nucl Chem*, vol. 307, pp. 1453–1458, 2016, doi: 10.1007/s10967-015-4359-z.

[147] E. Turan, S. Demirci, and T. Caykara, “Preparation of Polyacrylamide Hydrogels at Various Charge Densities by Postmodification,” no. July, 2008, doi: 10.1002/app.

[148] F. Sabbagh and I. I. Muhamad, “Physical and Chemical Characterisation of Acrylamide-Based Hydrogels, Aam, Aam/NaCMC and Aam/NaCMC/MgO,” *J Inorg Organomet Polym Mater*, vol. 27, no. 5, pp. 1439–1449, Sep. 2017, doi: 10.1007/s10904-017-0599-4.

[149] E. M. Ahmed, “Hydrogel: Preparation, characterization, and applications: A review.,” *J Adv Res*, vol. 6, no. 2, pp. 105–21, 2015, doi: 10.1016/j.jare.2013.07.006.

[150] X. Qiao *et al.*, “Progresses on the theory and application of quartz crystal microbalance,” *Appl Phys Rev*, vol. 3, no. 031106, 2016, doi: 10.1063/1.4963312.

[151] M. Khodakarami and L. Alagha, “Separation and recovery of rare earth elements using novel ammonium-based task-specific ionic liquids with bidentate and tridentate O-donor functional groups,” *Sep Purif Technol*, vol. 232, no. August 2019, p. 115952, 2020, doi: 10.1016/j.seppur.2019.115952.

[152] Y. Nakagawa, S. Sehata, S. Fujii, H. Yamamoto, A. Tsuda, and K. Koumoto, “Mechanistic study on the facilitation of enzymatic hydrolysis by α-glucosidase in the presence of betaine-type metabolite analogs,” *Tetrahedron*, vol. 70, no. 35, pp. 5895–5903, 2014, doi: 10.1016/j.tet.2014.06.028.

[153] M. D. Hanwell, D. E. Curtis, D. C. Lonie, T. Vandermeersch, E. Zurek, and G. R. Hutchison, “Avogadro: an advanced semantic chemical editor, visualization, and analysis platform,” *J Cheminform*, vol. 4, pp. 4–17, 2012, [Online]. Available: http://www.jcheminf.com/content/4/1/17

[154] F. Robinson and M. J. Zaworotko, “Triple Interpenetration in [Ag(4,4’-bipyridine)][N03], a Cationic Polymer with a Three-dimensional Motif Generated by Self-assembly of ’T-shaped’ Building Blocks,” vol. 163, no. 6, pp. 2413–2414, 1995.

[155] O. M. Yaghi and H. Li, “T-shaped molecular building units in the porous structure of Ag(4,4′-bpy)·NO3,” *J Am Chem Soc*, vol. 118, no. 1, pp. 295–296, 1996, doi: 10.1021/ja953438l.

[156] S. L. Cai, S. R. Zheng, J. B. Tan, M. Pan, J. Fan, and W. G. Zhang, “An unprecedented supramolecular network with channels filled by 1D coordination polymer chains: Cocrystallization of Ag(i)-4,4′-bipyridine and Ag(i)-benzimidazole complexes,” *CrystEngComm*, vol. 13, no. 21, pp. 6345–6348, 2011, doi: 10.1039/c1ce05535f.

[157] L. Zhu *et al.*, “Exceptional perrhenate/pertechnetate uptake and subsequent immobilization by a low-dimensional cationic coordination polymer: Overcoming the hofmeister bias selectivity,” *Environ Sci Technol Lett*, vol. 4, no. 7, pp. 316–322, 2017, doi: 10.1021/acs.estlett.7b00165.

[158] L. Zhu *et al.*, “Exceptional perrhenate/pertechnetate uptake and subsequent immobilization by a low-dimensional cationic coordination polymer: Overcoming

the hofmeister bias selectivity," *Environ Sci Technol Lett*, vol. 4, no. 7, pp. 316–322, 2017, doi: 10.1021/acs.estlett.7b00165.

[159] S. Wannapaiboon *et al.*, "Hierarchical structuring of metal-organic framework thin-films on quartz crystal microbalance (QCM) substrates for selective adsorption applications," *J Mater Chem A Mater*, vol. 3, no. 46, pp. 23385–23394, 2015, doi: 10.1039/c5ta05620a.

[160] I. R. Colinas, R. C. Silva, and S. R. J. Oliver, "Reversible, Selective Trapping of Perchlorate from Water in Record Capacity by a Cationic Metal-Organic Framework," *Environ Sci Technol*, vol. 50, no. 4, pp. 1949–1954, 2016, doi: 10.1021/acs.est.5b03455.

[161] K. Y. Foo and B. H. Hameed, "Insights into the modeling of adsorption isotherm systems," *Chemical Engineering Journal*, vol. 156, no. 1, pp. 2–10, 2010, doi: 10.1016/j.cej.2009.09.013.

[162] I. Langmuir, "The constitution and fundamental properties of solids and liquids," *J Am Chem Soc*, vol. 38, no. 11, pp. 2221–2295, 1916.

[163] H. Freundlich, "OF THE ADSORPTION OF GASES . SECTION 11 . KINETICS AND ENERGETICS OF GAS ADSORPTION .," *Tansactions of the Faraday Society*, 1932.

[164] R. Sips, "On the Structure of a Catalyst Surface," *Journal of Chemical Physics*, vol. 16, no. 5, 1948.

[165] M. T. Rahman, T. Kameda, S. Kumagai, and T. Yoshioka, "Adsorption isotherms and kinetics of arsenic removal from aqueous solution by Mg–Al layered double hydroxide intercalated with nitrate ions," *Reaction Kinetics, Mechanisms and Catalysis*, vol. 120, no. 2, pp. 703–714, Apr. 2017, doi: 10.1007/s11144-016-1116-4.

[166] Y. Huang, X. Lee, F. C. Macazo, M. Grattieri, R. Cai, and S. D. Minteer, "Fast and efficient removal of chromium (VI) anionic species by a reusable chitosan-modified multi-walled carbon nanotube composite," *Chemical Engineering Journal*, vol. 339, pp. 259–267, May 2018, doi: 10.1016/j.cej.2018.01.133.

[167] G. Limousin, J. P. Gaudet, L. Charlet, S. Szenknect, V. Barthès, and M. Krimissa, "Sorption isotherms: A review on physical bases, modeling and measurement," *Applied Geochemistry*, vol. 22, no. 2, pp. 249–275, 2007, doi: 10.1016/j.apgeochem.2006.09.010.

[168] N. Tzabar and H. J. M. ter Brake, "Adsorption isotherms and Sips models of nitrogen, methane, ethane, and propane on commercial activated carbons and polyvinylidene chloride," *Adsorption*, vol. 22, no. 7, pp. 901–914, 2016, doi: 10.1007/s10450-016-9794-9.